Formulation of a high-fidelity multibody dynamical model for an electric solar wind sail

Guillermo Pacheco-Ramos[a,*], Daniel Garcia-Vallejo[b] and Rafael Vazquez[a]

[a]Department of Aerospace Engineering, Universidad de Sevilla, Seville, Spain
[b]Department of Mechanical Engineering and Manufacturing, Universidad de Sevilla, Seville, Spain

ARTICLE INFO

Keywords:
Electric solar wind sail dynamics
High fidelity E-sail model
Multibody system dynamics
ANCF for cable elements
Tether dynamics
DAE

ABSTRACT

E-sail technology enables a continuous propulsion system based on the repulsive force exerted by solar wind protons on a set of positively charged tethers. Diverse methods have been explored within the last two decades to investigate the dynamics of E-sail. This work introduces a dynamic multibody model combining Absolute Nodal Coordinate Formulation (ANCF) and Natural Coordinates (NC) to describe flexible and rigid bodies, respectively. A complete formulation for cable elements considering nonlinear bending and internal damping is provided. Coulomb propulsive forces are included and the expressions for the integration of the resulting Differential Algebraic Equation (DAE) system are given. Based on the simulation results obtained from the proposed model, the convenience of considering bending stiffness to accurately capture the dynamics is proven. The in-plane and out-of-plane oscillations of the tethers are reported and explained. By means of the Power Spectral Density (PSD) representation, the relevant role on the E-sail dynamics of the spin, bending and axial modes, associated to the well-known problem of a rotating cable with a tip mass, is described. The force and perturbation moments transmitted to the central body are compared to the generated thrust, and its complexity and instability under non-null sailing angle operation is established.

1. Introduction

The E-sail is a propellantless propulsion technology proposed by Janhunen [1], which extracts thrust from the solar wind protons. The most extended configuration of the E-sail follows a hub-spoke architecture in which the main spacecraft is located in the center and the positively charged tethers are distributed radially [2]. The whole system spins around the principal axis and tethers' stability is increased thank to the centrifugal force exerted on the remote units located at their outer end. The repulsion phenomenon and force generation, which are the base of the E-sail propulsion, have been analyzed in detail [3–7] with different models. The influence of the solar wind density and speed, or the difference of electric potential at the wire, among others, is quantified and the modulation of the wire voltage is identified as a key control magnitude of the E-sail [8].

The performance of the E-sail concept as a main propulsion system has been assessed [3, 9], showing promising results in terms of competitiveness, [10, 11], for a wide range of missions: planetary rendez vous [12], heliocentric transfer missions [13, 14], non-Keplerian orbits [15] or asteroids exploration [16] between others. To navigate the planned trajectories, on the one hand, the module of the propulsive force may be adjusted thanks to voltage modulation. On the other hand, the orientation of the thrust force can be established by modifying the orientation of the E-sail axis respect to the solar rays; the angle formed between them is commonly referred to as sailing angle. When this angle is not null, the thrust has a component on the spin plane [9] which, together with the orbital Coriolis forces, generates effects that may conduce to tether collision [16]. In order to mitigate this risk, different solutions are proposed [17] such as the inclusion of auxiliary tethers, active remote units or photonic blades.

Early research on E-sail dynamics proposed the use of an spherical pendulum model [8], in which tethers are modelled as rotating rigid thin wires under the effect of orbital and Coulomb forces, and where the use of a secondary tether is considered. Under this approach, it is proven that a stable evolution as well as spin rate and orientation control of the sail can be ensured by means of the modulation of tether voltage. The previous spherical pendulum model is improved by including the centrifugal forces associated to the spin of the E-sail, acting on main tether and remote

*Correspondence to: G. Pacheco-Ramos.
gpacheco@us.es (G. Pacheco-Ramos); dgvallejo@us.es (D. Garcia-Vallejo); rvazquez1@us.es (R. Vazquez)
ORCID(s): 0000-0001-9655-7820 (G. Pacheco-Ramos); 0000-0002-2319-2688 (D. Garcia-Vallejo); 0000-0001-6904-2055 (R. Vazquez)

mass [18]. As a first result, a criterion for the selection of the spin frequency is established, ensuring that the ratio of centrifugal and Coulomb effects is greater than 5. Secondly, it is proven that the voltage modulation on secondary tethers may be sufficient to compensate the secular variation of spin rate associated to orbit Coriolis forces, reinforcing the propellantless character of the E-sail. The spherical pendulum model applied to a single rotating tether [19], is considered for the derivation of control efficiency and indicates that a on-off modulation of the main tether voltage makes possible the operation on amplified transverse thrust conditions. Under this modulation it is verified that thrust angle approximately equals the sailing angle, in contrast to continuous modulation in which the thrust angles is half of the sailing angle. In addition, a reduction of power consumption is established.

E-sail modelling is further ameliorated by the contributions of studies providing analytical approximations for realistic sail shapes under the effect of Coulomb and centrifugal forces [20]. Under this approach, Coulomb forces and torques are computed and the voltage modulation required to counteract the torque and maintain E-sail attitude is given. On a similar line, the equilibrium deformed shape is computed under the hypothesis of axial-symmetry, [21], and considered to define voltage modulation to remove torque and perform attitude control under null or small sailing angle conditions [22, 23].

Numerical approaches based on lumped mass models have also been investigated [24, 25]. The control of the secular variation of spin rate by aux tether voltage modulation is proven for two types of secondary tethers configurations: galvanically connected "T-tether" and insulated "I-tethers" [24]. The complexity of the E-sail dynamics is confirmed by the oscillating behaviour of the relative position of the ends of a single tether firstly revealed in [25], and associated to the combined action of inertial, Coulomb and tether internal forces. Their lumped mass model (in which a viscous-elastic tether is proposed) reveals the influence of the spin rate in the system dynamics, subsequently known as coning motion. The comparison of the lumped mass model against the dumbbell idealization for a single tether, in which transverse deformation is neglected, validates the use of the latter in the case that centrifugal forces are dominant and the transversal effects can be disregarded. The use of finite elements based on the Nodal Position Finite Element Method (NPFEM), [26], is applied to deorbit electrodynamics tethered systems [27] and to E-sail concept [28]. In [28], a multi-physic model is defined for an E-sail in which tethers are represented by flexible truss elements and central vehicle as a point mass. Orbit and attitude coupling is investigated, concluding that it is a long-term effect and negligible for the short term. Results for unbalanced configuration and parametric analysis are also provided for a deeper understanding of the dynamics of an E-sail containing auxiliary tethers. Additional parameters and the influence of relative solar wind velocity are explored considering the same modelling approach [29] and the control of secular spin rate oscillation is validated under the NPFEM strategy. An important milestone in the comprehension of E-sail dynamics is achieved with the deduction of the coning motion frequency and equilibrium angle presented in [30].

Concerning the multibody character of the proposed E-sail models, most of the works on this topic neglect the dynamics of the central body, given the typical length of the tethers, and model it as a lumped mass. An exception can be found in [31], where a multibody model based on dumbbell simplifications is proposed and studied, but only null sailing angle configuration are explored. Additionally, a multibody idealization, considering a rigid body for the main spacecraft and flexible tethers formulated by NPFEM, is investigated in [32], which demonstrates the appearance of perturbation torques on the main spacecraft due to the motion of the center of mass and the evolution of the thrust force. Additional fluctuations of tether tension leading to disturbances on the spacecraft angular rate and attitude are identified and finally, the necessity of using remote units to control the spin rate is showed in this notable contribution [32].

In addition to the NPFEM [28–30, 32] and the lumped mass approximation [24, 25] previously exposed, other methods have also been investigated to analyse the dynamics of the E-sail. The Reference Nodal Coordinate Formulation (RNCF) and the nonlinear Floating Frame of Reference Method (FFRM), are compared for studying the dynamics and defining control strategies of a flexible E-sail in [33]. Moreover, the Absolute Nodal Coordinate Formulation (ANCF) has also been considered [34, 35]. The ANCF is a widely used formulation, which presents the advantage, with respect to the NPFEM, of making possible the formulation of non-singular cable elements to account for bending stiffness, as pointed out in [26]. The necessity of incorporating the cable bending stiffness into tethers models has been proven [36–38], and justifies efforts oriented to achieve this objective for NPFEM [39, 40]. However, even when the formulation is improved, to avoid ill-conditioning a moderate element slenderness has to be ensured, forcing an unaffordable reduced integration time step [26]. Proposed in [41, 42], and given the use of absolute nodal coordinates and the selection of the shape functions, ANCF allows a zero strain condition under rigid body motion, and is able to consider large displacement and nonlinear behaviours. The selection of nodal displacements and slopes as nodal coordinates, enables the formulation of bi-dimensional and three-dimensional beam elements with a

constant mass matrix [43, 44]. In contrast, the expressions of elastic forces become highly nonlinear. The available beam elements formulated under ANCF can be separated into those considering shear and cross section deformation [43, 44] and those with gradient deficient elements where transverse shear deformation cannot be captured [45, 46]. These last group is of special interest for tether applications. Given that slope vectors on the transverse directions are omitted from the nodal coordinates vector, cross sectional deformation, torsion or Poisson effects cannot be directly derived [46]. However, modified formulations have been proposed [47, 48] to tackle these issues and improve the capabilities of the original ACNF cable formulation. In addition to the elemental capabilities, the adequacy of a formulation to integrate joint constraints is a relevant aspect for applications on multibody systems. There are an extensive number of contributions for ANCF in this regard, [49, 50] which propose and evaluate a wide range of formulations for joint constraints, contacts or sliding joints, among others. For the current application, only spherical joints are formulated according to [51, 52], and the corresponding set of linear constraints equations is incorporated to the associated Differential Algebraic Equation (DAE) system. The combined use of ANCF for the formulation of flexible elements, and Natural Coordinates (NC) for rigid elements notably simplifies the formulation of combined rigid-flexible joint constraint equations [53, 54].

The applicability and efficiency of ANCF to model nonlinear dynamics have been investigated and demonstrated, not only for space applications, but also in other fields [55, 56]. ANCF's capability to address large displacement problems has been highlighted in numerous flexible multibody dynamics reviews [49, 50, 57, 58] and demonstrated by its extensive use in the field of Tethered Satellite System (TSS). Research on TSS has led to remarkable contributions and applications of the ANCF method. Namely, the development of variable length ANCF cable elements and its application to the deployment and control of TSS [59–61], the vibration and stability analysis of Long Tethered Satellite Systems under a multibody perspective [62], or the investigation of space tethered-net dynamics [63, 64]. ANCF Cable elements are used to study the E-sail dynamics in [34], where the the importance of transverse effects for small spin rates is highlighted. However, despite of the high potential of ANCF and the numerous contributions on the TSS field, an specific development of a multibody E-sail model considering a detailed formulation of the tether has not yet been proposed.

Regarding numerical algorithms and techniques, significant integration schemes for the solution of the DAE system, are based on implicit Runge-Kutta scheme [65, 66], generalized-α algorithm [67, 68] and structure-preserving methods [69, 70]. On one hand, symplectic methods are the most adequate option for long-term simulations in which the preservation of energy and momentum need to be ensured. On the other hand, the generalized-α scheme presents a second order convergence rate and adjustable numerical damping at high-frequency [68] and its implementation is simple and direct which justifies its choice for the present work.

In the current work, a high-fidelity dynamical model for an electric solar wind sail is presented. A rigid-flexible multibody approach is proposed considering the main spacecraft, the tethers and the remote masses. The central spacecraft is modeled as a rigid cylinder formulated using NC, the tethers are represented by cable elements established in ANCF and remote units are considered as lumped masses. The dynamic problem is stated using the Lagrangian formulation and Lagrange multipliers are used to establish the pinned joint condition between the cables and the center body at the anchor points. In contrast to previous works considering multibody and flexible tethers in NPFEM [32], the proposed cable elements include bending stiffness which is proven to be critical to capture the cable dynamics in a more accurate way. The formulation of an E-sail considering ANCF proposed in [34], is improved by the multibody approach and the inclusion of structural damping capability and nonlinear bending for the tethers. Regarding external forces, a Coulomb propulsive force model according to [71] is considered, whereas gravitational forces are neglected given its long-term nature revealed in [28]. The full set of expressions for the evaluation of Jacobians and additional elements necessary for integration of the DAE system by means of the generalized-α algorithm are provided [68]. Results on generalized coordinates are translated into a more comprehensible set of dynamic and attitude variables. It should be noted that, given the multibody character of the model, two attitudes are calculated. Firstly, the attitude of the central vehicle, given by the Euler angles ψ, θ and ϕ. And secondly, the attitude of the E-sail, defined as the orientation of the mean plane containing the remote masses, and given by the angles Ψ, Θ and Φ. Simulations are carried out for an E-sail baseline configuration to investigate the evolution of dynamic variables defining the motion of the tethers and central vehicle.

The original contributions of this work are as follows. It presents the first multibody model of an E-sail solely based on absolute coordinates, in which ANCF is used for the tethers and NC for the central body. The formulation for bending forces includes the nonlinear curvature effect, therefore allowing the comparison with models considering linear bending or truss elements for the mathematical representation of tethers. In addition, the inclusion of internal

damping enables the evaluation of the effect of internal dissipation in the dynamics of the system. Furthermore, this work contributes to the understanding of the E-sail dynamics by the identification of the main governing frequencies: spin, already identified in previous works, but also bending and axial modes. Besides, the current work presents a novel study of the tether in-plane oscillation for an E-sail, being of special interest to assess the risk of collision of the cables for configuration without secondary tethers, which is a risk mentioned in the literature [16], but not deeply investigated until today. An E-sail configuration without secondary tethers involves a greater specific propulsion and a notably simpler deployment process, and the identification and explanation of tether lagging presented in the current work represents an advance in the comprehension of the E-sail system. The accurate modelling and precise understanding of the E-sail dynamics from a multibody perspective is also a valuable asset for the progress of advanced stability and deployment analyses [72, 73]. Moreover, and for the first time, the evolution of the orientation of the tethers at the anchor points is explicitly described and the participating vibration modes examined. As a consequence, the forces transmitted to the central vehicle are detailed, allowing to improve the comprehension of the existing perturbation torques applied to the central vehicle and explaining the corresponding angular rates oscillations. Finally, and as a consequence of the multibody character of the proposed model, the evolution of the attitude is studied and compared for both the central vehicle and the remote units mean plane.

The present article is organized as follows. Following the introduction, Sect. 2 describes the formulation of the multibody rigid-flexible E-sail model, defines the coordinate systems used and the formulation in absolute coordinates of the rigid body, the flexible cable elements and the displacement constraints. Next Sect. 3 contains the description of the auxiliary variables and magnitudes defined for a better interpretation of the system dynamics. The analysis results are provided in Sect. 4. Firstly, the results for the convergence analysis are presented. The effect of keeping or neglecting the bending stiffness of the tethers is illustrated by comparing the results achieved by considering cable or truss elements. Secondly, the results for the dynamics of a single tether are presented and described. Finally, the E-sail dynamics results are provided. Finally, some conclusions and future lines of work are stated in Sect. 5.

2. Formulation of the E-sail model and dynamic problem

In this section, the definition of the E-sail dynamic model is presented. The components considered for the multibody system are described, the associated constraints introduced, and the contributions considered are identified, allowing the establishment of the DAE system. Moreover, the assembly process of the system generalized coordinates vector, mass matrix, generalized forces and constraints is outlined and the implemented DAE integration method is introduced. Additionally, dedicated sections are incorporated to describe the coordinate frames, as well as the formulation of the cable elements used to model the flexible tethers and the rigid body considered for the central vehicle.

The dynamics of the E-sail multibody system is formulated following the Lagrangian approach [42] and its idealization is established, as described in Fig. 1(a), considering a rigid body for the central vehicle, flexible bodies for the tethers and point masses for the remote units. The rigid body is assumed to be a cylinder of height h_r, radius R_r and homogeneous density ρ_r. The flexible tethers are modelled as cables with constant transverse section, given by area A_t and inertia I_t, length L_0, homogeneous density ρ_t and Young Modulus E_t. The radial tethers considered in the configuration assessed in this paper, are known as main tethers, and the number of main tethers contained by the sail is represented by p. The contribution of the rigid and flexible elements to the constant global mass matrix $\boldsymbol{\mathcal{M}}$, and the generalized forces $\boldsymbol{\mathcal{Q}}_a(\dot{\mathbf{q}}, \mathbf{q}, t)$, are computed in terms of the time t, the generalized coordinate vector $\mathbf{q}$ and its velocity vector, $\dot{\mathbf{q}}$. Their formulation are described in Sect. 2.2 for flexible parts, and in Sect. 2.3 for the rigid body. The point masses m_u, associated to the remote units are simply added to the mass matrix at the corresponding nodal coordinates location. Additionally, there exist a set of constraint equations applicable to the system and comprised at matrix $\boldsymbol{\mathcal{C}}(\dot{\mathbf{q}}, \mathbf{q}, t)$, which are imposed by the introduction of the Lagrange multipliers vector, $\boldsymbol{\lambda}$. Two main types of constraints are differentiated: the joints' constrains associated to the continuity of the displacements between the tethers and the rigid body at the anchor points, named $\mathbf{C}_a$ and described at Sect. 2.4, and the internal constrains associated to the formulation of the rigid body formulated as per Sect. 2.3.1 and designated as $\mathbf{C}_r$. Consequently, the system constraint matrix is determined by the concatenation $\boldsymbol{\mathcal{C}} = [\mathbf{C}_a^T \ \mathbf{C}_r^T]^T$. Defining $\dot{(\,)}$ as the time derivative and $(\,)_{,\mathbf{q}}$ and $(\,)_{,t}$ as the partial derivative respect $\mathbf{q}$ and t, respectively, the second time derivative of the constrains matrix $\boldsymbol{\mathcal{C}}$ leads to the expression shown next, which generally defines $\boldsymbol{\mathcal{Q}}_\lambda(\dot{\mathbf{q}}, \mathbf{q}, t)$ as

$$\boldsymbol{\mathcal{C}}_{,\mathbf{q}}\ddot{\mathbf{q}} = -\boldsymbol{\mathcal{C}}_{,tt} - \left(\boldsymbol{\mathcal{C}}_{,\mathbf{q}}\dot{\mathbf{q}}\right)_{,\mathbf{q}}\dot{\mathbf{q}} - 2\boldsymbol{\mathcal{C}}_{,\mathbf{q}t}\dot{\mathbf{q}} = \boldsymbol{\mathcal{Q}}_\lambda. \tag{1}$$

However, given that the constraints previously mentioned are scleronomic, the actual dependence of constrains matrix

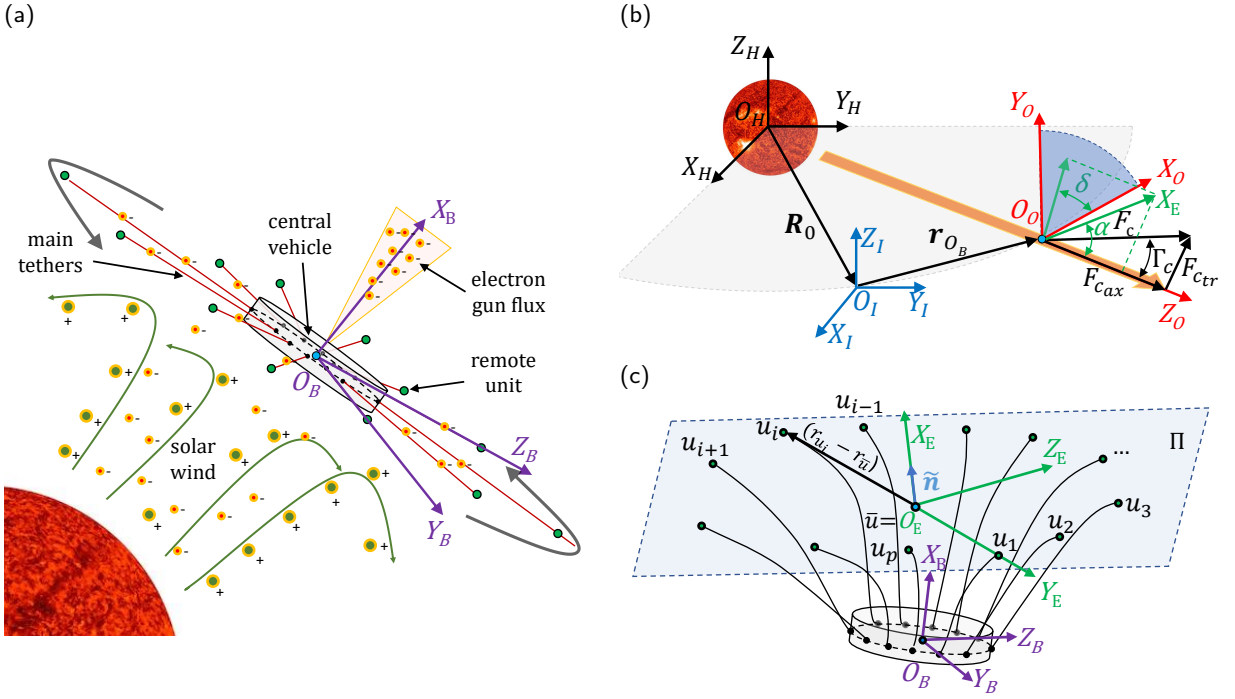

Figure 1: (a) Description of the main components of an E-sail and its interaction with the solar wind, when a positive bias voltage at tethers is maintained by the operation of an electron gun. Establishment of E-sail body coordinate system B; (b) Description of the main reference frames considered for the formulation: heliocentric ecliptic inertial H, inertial I and orbital O. Description of the sailing α, and precession δ, angles, established between the vector X_E and the solar rays. Description of the propulsive force resultant, given by its module, F_c, and its orientation respect to the solar rays, Γ_c. Definition of the decomposition of the propulsive force into the longitudinal $F_{c_{ax}}$ and transversal $F_{c_{tr}}$ contributions; and (c) Description of the auxiliary E-sail coordinate system E, established by the mean plane of the remote units Π, and the location of the first remote unit u_1.

can be written as $\boldsymbol{\mathscr{C}}(\mathbf{q})$. Consequently, both $\boldsymbol{\mathscr{C}}_{,tt}$ and $\boldsymbol{\mathscr{C}}_{,\mathbf{q}t}$ terms are null and Eq. (1) reduces to

$$\boldsymbol{\mathcal{Q}}_\lambda = -\left(\boldsymbol{\mathscr{C}}_{,\mathbf{q}}\dot{\mathbf{q}}\right)_{,\mathbf{q}}\dot{\mathbf{q}}. \tag{2}$$

Taking into consideration the previous definitions, the dynamic equations of the system can be written as the following index-3 DAE system in matrix form

$$\begin{bmatrix} \boldsymbol{\mathcal{M}} & \boldsymbol{\mathscr{C}}_{,\mathbf{q}}^T \\ \boldsymbol{\mathscr{C}}_{,\mathbf{q}} & \mathbf{0} \end{bmatrix} \begin{bmatrix} \ddot{\mathbf{q}} \\ \boldsymbol{\lambda} \end{bmatrix} = \begin{bmatrix} \boldsymbol{\mathcal{Q}}_a \\ \boldsymbol{\mathcal{Q}}_\lambda \end{bmatrix}. \tag{3}$$

Concerning the vector of generalized forces of the system $\boldsymbol{\mathcal{Q}}_a$, it comprises the following contributions: the Coulomb force $\boldsymbol{\mathcal{Q}}_c$, induced on the charged tethers by the solar wind, the elastic forces $\boldsymbol{\mathcal{Q}}_e$, obtained from the elastic energy stored on flexible bodies and finally the damping forces $\boldsymbol{\mathcal{Q}}_d$, derived from the internal energy dissipation occurring on flexible bodies. Going deeper into the structure of $\mathbf{q}$, it consists on the union of the generalized coordinates of the rigid element, $\mathbf{d}$, and the generalized coordinates associated to the flexible parts. Consequently, it can be written as

$$\mathbf{q} = \left[\mathbf{d}_1^T\ \mathbf{d}_2^T\ \mathbf{d}_3^T\ \mathbf{d}_4^T \mid \hat{\mathbf{e}}_{11}^T\ \hat{\mathbf{e}}_{12}^T \dots \hat{\mathbf{e}}_{1j}^T\ \hat{\mathbf{e}}_{1n}^T \mid \dots \mid \hat{\mathbf{e}}_{i1}^T\ \hat{\mathbf{e}}_{i2}^T \dots \hat{\mathbf{e}}_{ij}^T \dots \hat{\mathbf{e}}_{in}^T \mid \dots \mid \hat{\mathbf{e}}_{p1}^T\ \hat{\mathbf{e}}_{p2}^T \dots \hat{\mathbf{e}}_{pj}^T \dots \hat{\mathbf{e}}_{pn}^T\right]^T, \tag{4}$$

where $\mathbf{d}_k$ represent the generalized coordinates of the node k considered for the formulation of the rigid body. As explained in Sect. 2.3, four basic points are considered, $k = 1, \dots, 4$, and the nodal coordinates include just the

nodal position expressed in an absolute frame. Consequently the dimensions of $\mathbf{d}_k$ are 3×1, and the total number of generalized coordinates associated to the rigid definition, $\mathbf{d}$, is equal to twelve. In relation to the definition of flexible elements, described in more detail in Sect. 2.2, $\hat{\mathbf{e}}_{ij}$ represent the nodal coordinates of the j^{th} node of tether i. In the present case, given the gradient deficient definition chosen for the cable elements, the generalized coordinates include the nodal position and the longitudinal slope, being the dimensions of each set of nodal coordinates equal to 6×1. For an E-sail formed by p tethers, in which each tether is divided by n nodes into q finite elements, being $q = n - 1$, the dimensions of the generalized coordinates associated to the flexible cables are $(6n\,p) \times 1$. It is concluded that the number of generalized coordinates of the system, contained in vector $\mathbf{q}$ and referred from now on as m, is $m = (6n\,p + 12)$. Given the formulation of the rigid body, Sect. 2.3 introduces six internal constraints, and keeping in mind that each of the spherical joint at tethers root, formulated in Sect. 2.4, is equivalent to three constraints equations, the total number of constraints of the system is $c = 6 + 3p$. Consequently, the number of degrees of freedom of the system is $s = m - c = 6 + 3(2n - 1)p$.

Assembly of the system generalized matrices/vectors from the elemental results

This paragraph introduces the assembly process of the system generalized vectors and matrices from the contribution of the rigid body and flexible elements making use of the Boolean matrices presented subsequently. The base of this process is the extraction from vector $\mathbf{q}$ of the coordinates $\hat{\mathbf{e}}_{ij}$ associated to an specific node j of a given tether i, which can be easily carried out using the following matrix product

$$\hat{\mathbf{e}}_{ij} = \hat{\mathbf{B}}^e_{ij}\mathbf{q}, \tag{5}$$

where $\hat{\mathbf{B}}^e_{ij}$ is the Boolean matrix of dimensions $6 \times m$ for flexible components

$$\hat{\mathbf{B}}^e_{ij} = \left[\mathbf{0}_{6\times 12} \,|\, \mathbf{0}_{6\times 6n(i-1)} \,|\, \mathbf{0}_{6\times 6(j-1)} \,|\, \mathbf{I}_{6\times 6} \,|\, \mathbf{0}_{6\times 6(n-j)} \,|\, \mathbf{0}_{6\times 6n(p-i)}\right], \tag{6}$$

in which the dimensions of each of the blocks can be explained as it follows: the first null sub matrix corresponds to the coordinates of the 4 basic points used for the definition of the rigid body. The second, with dimensions $6\times 6n(i-1)$, is associated to the $(i-1)$ previous tethers. The element $\mathbf{0}_{6\times 6(j-1)}$ corresponds to the coordinates associated to the initial $(j-1)$ nodes of tether i. The identity matrix of size 6 allows the extraction of the coordinates of interest $\hat{\mathbf{e}}_{ij}$, while the following element $\mathbf{0}_{6\times 6(n-j)}$, completes the coordinates of the remaining $(n-j)$ nodes of tether i. To conclude, $\mathbf{0}_{6\times 6n(p-i)}$ corresponds to the coordinates appertaining to the subsequent $(p-i)$ tethers. Analogously, the Boolean matrix $\mathbf{B}^r_k$, $3 \times m$, that allows the extraction of the nodal coordinates associated to basic point k of the rigid body, can be formulated as

$$\mathbf{B}^r_k = \left[\mathbf{0}_{3\times 3(k-1)} \,|\, \mathbf{I}_{3\times 3} \,|\, \mathbf{0}_{3\times 3(4-k)} \,|\, \mathbf{0}_{3\times 6n\cdot p}\right]. \tag{7}$$

The assembly of the generalized forces vector $\mathcal{Q}_k$, with dimensions $m \times 1$, can be achieved by making use of the previous Boolean matrices to integrate the contributions of the flexible elements and the rigid body conforming the E-sail. For the sake of brevity, the assembly process, applicable to any of the contributions to generalized forces previously mentioned, is described considering a non-specific generalized force $\mathcal{Q}$. The elemental coordinate vector associated to the j^{th} flexible finite element of tether i, $\mathbf{e}_{ij}$ is formed by the vertical concatenation of nodal coordinate vectors associated to the j^{th} and $(j+1)^{\text{th}}$ nodes of tether i, of size 12×1. Elemental coordinates could be simply extracted from $\mathbf{q}$, making used of the Boolean matrices associated to the nodal contributions

$$\mathbf{e}_{ij} = \begin{bmatrix} \hat{\mathbf{e}}_{ij} \\ \hat{\mathbf{e}}_{i(j+1)} \end{bmatrix} = \begin{bmatrix} \hat{\mathbf{B}}^e_{ij} \\ \hat{\mathbf{B}}^e_{i(j+1)} \end{bmatrix} \mathbf{q} = \mathbf{B}^e_{ij}\mathbf{q}, \tag{8}$$

and the transposes of the elemental Boolean matrix $\mathbf{B}^e_{ij}$ for flexible elements and for the rigid body $\mathbf{B}^r_k$, allow to write

$$\mathcal{Q} = \sum_{i=1}^{p}\sum_{j=1}^{n-1}\left(\mathbf{B}^e_{ij}\right)^T \mathbf{Q}^e_{ij} + (\mathbf{B}^r)^T\,\mathbf{Q}^r, \tag{9}$$

where the initial double summation in i and j, computes the contribution of flexible elements, being $\mathbf{Q}^e_{ij}$ the elemental generalized forced vector, of dimensions 12×1, of the j^{th} flexible element of tether i. In the second summand, related

to the rigid body, $\mathbf{Q}^r$ is the generalized forced associated to the rigid body with dimensions 12×1 and $\mathbf{B}^r$ is defined as the Boolean matrix that extracts from $\mathbf{q}$ the rigid body coordinates $\mathbf{d}$, given by

$$\mathbf{B}^r = \left[(\mathbf{B}_1^r)^T \mid (\mathbf{B}_2^r)^T \mid (\mathbf{B}_3^r)^T \mid (\mathbf{B}_4^r)^T\right]^T. \tag{10}$$

Similarly, the assembly of the mass matrix of the full system, $\boldsymbol{\mathcal{M}}$, can be accomplished considering

$$\boldsymbol{\mathcal{M}} = \sum_{i=1}^{p}\sum_{j=1}^{n-1}\left(\mathbf{B}_{ij}^e\right)^T \mathbf{M}_{ij}^e \mathbf{B}_{ij}^e + (\mathbf{B}^r)^T \mathbf{M}^r \mathbf{B}^r, \tag{11}$$

where $\mathbf{M}_{ij}^e$ correspond to the elemental mass matrix of the j^{th} flexible finite element of tether i, and $\mathbf{M}^r$ is the mass matrix of the central rigid body. The exposed rationale, with slight adaptations, is used to carry out the assembly of the Jacobian matrix of the system constraints $\boldsymbol{\mathcal{C}}_{,q}$ and the associated force $\boldsymbol{\mathcal{Q}}_\lambda$, however in the interest of concision the details are omitted here.

DAE integration

This section describes the basic aspects of generalized-α method considered for the numerical integration of the DAE system.

Once the different contributions to the system dynamics are computed and assembled into the matrix form presented in Eq. (3), the integration of the DAE system is carried out based on a generalized-α scheme in which the dynamic equilibrium is enforced at every step [68]. This implicit strategy, based on the Newmark method, offers a good accuracy at low frequencies and the possibility of regulating numerical damping for high frequencies by adjusting the value of the parameters. Although the algorithm's details can be consulted in [68], it is remarked that its implementation is simple but requires the calculation of the Jacobian of the generalized forces. The direct integration of the index-3 DAE system requires that, at each time step, the dynamic equilibrium is enforced by the fulfilment of Eq. (3); consequently, the position constraint equations are directly satisfied and the accelerations are computed with second-order accuracy [68]. The correction of the generalized coordinates $\boldsymbol{\Delta}_q$, and the Lagrange multipliers $\boldsymbol{\Delta}_\lambda$, are given by the solution of the linear system

$$\mathbf{S}_t \begin{bmatrix}\boldsymbol{\Delta}_q \\ \boldsymbol{\Delta}_\lambda\end{bmatrix} = -\begin{bmatrix}\mathbf{r}_q \\ \mathbf{r}_\lambda\end{bmatrix}, \tag{12}$$

where $\mathbf{r}_q$ and $\mathbf{r}_\lambda$ correspond to the residuals associated to the dynamic and constraints equations, respectively, evaluated considering the current estimation of the generalized coordinates and Lagrange multipliers. Considering that all the dynamical and constraint equations are expressed in SI units, a residuals' tolerance equal to 10^{-5} is demanded to conclude the iterative solution. Additionally, the iteration matrix $\mathbf{S}_t$ is written as

$$\mathbf{S}_t = \begin{bmatrix}(\boldsymbol{\mathcal{M}}\nu' + \mathbf{C}_t\mu' + \mathbf{K}_t) & \boldsymbol{\mathcal{C}}_{,\mathbf{q}}^T \\ \boldsymbol{\mathcal{C}}_{,\mathbf{q}} & 0\end{bmatrix}, \tag{13}$$

where are ν' and μ' are the step correction parameters associated to acceleration and velocity. In addition, given the absolute formulation used for the dynamics and the forces considered, the damping tangent matrix $\mathbf{C}_t$ is defined as

$$\mathbf{C}_t = -\frac{\partial \boldsymbol{\mathcal{Q}}_a}{\partial \dot{\mathbf{q}}} = -\frac{\partial \boldsymbol{\mathcal{Q}}_d}{\partial \dot{\mathbf{q}}}, \tag{14}$$

and the stiffness tangent matrix $\mathbf{K}_t$ as

$$\mathbf{K}_t = -\frac{\partial(\boldsymbol{\mathcal{M}}\ddot{\mathbf{q}} - \boldsymbol{\mathcal{Q}}_a + \boldsymbol{\mathcal{C}}_{,q}^T\boldsymbol{\lambda})}{\partial \mathbf{q}} = -\frac{\partial \boldsymbol{\mathcal{Q}}_e}{\partial \mathbf{q}} - \frac{\partial \boldsymbol{\mathcal{Q}}_c}{\partial \mathbf{q}} - \frac{\partial \boldsymbol{\mathcal{Q}}_d}{\partial \mathbf{q}} + \frac{\partial(\boldsymbol{\mathcal{C}}_{,q}^T\boldsymbol{\lambda})}{\partial \mathbf{q}}. \tag{15}$$

In order to enable the implementation, the Jacobians of all the terms involved are provided at Sect. 2.2 for flexible cables, Sect. 2.3 for rigid body and Sect. 2.4 for constraints.

To complete the description of the DAE integration, the definition of the algorithm parameters considered is provided hereafter. In accordance with [68], the step correction parameter are established as $\nu' = \left(1-\alpha_m\right) / \left(h^2\nu\left(1-\alpha_f\right)\right)$

and $\mu' = \mu/(h\nu)$, being h the time step and set equal to 0.1 seconds. The rest of the numerical parameters are selected to ensure accuracy and stability properties as: $\alpha_m = \left(2\rho_\infty - 1\right)/\left(\rho_\infty + 1\right)$, $\alpha_f = \rho_\infty/\left(\rho_\infty + 1\right)$, $\mu = 1/2 + \alpha_f - \alpha_m$ and $\nu = 1/4\,(\mu + 1/2)^2$, where ρ_∞ is the spectral radius controlling the numerical damping and which is defined as $\rho_\infty = 0.25$ for all the simulations.

2.1. Reference frames

This section defines the coordinate systems used in the formulation of the dynamical problem.

The four coordinate systems depicted in Fig. 1(b) are the main frames considered for the formulation of the dynamic problem: the heliocentric ecliptic inertial (H) coordinate system $O_H X_H Y_H Z_H$, the body (B) coordinate system, $O_B X_B Y_B Z_B$, the orbit (O) frame established by $O_O X_O Y_O Z_O$ and the inertial (I) coordinate system defined by $O_I X_I Y_I Z_I$. The unitary vectors associated to the axes X_K, Y_K and Z_K are defined as $\mathbf{i}_K$, $\mathbf{j}_K$ and $\mathbf{k}_K$, respectively, for $K = H, B, O, I$. The origin of the H frame, O_H is located at the center of mass of the Sun, the axis X_H points in the Vernal Equinox direction, axis Z_H follows the normal to the ecliptic plane and Y_H completes the right-hand coordinate system. This frame is considered an inertial frame. The body frame, has its origin O_B, at the geometric center of the main spacecraft, which is assumed to be a cylinder, the axes X_B, Y_B and Z_B follows the orientations defined for the local coordinate system of the rigid body defined in Sect. 2.3. The origin of the orbit coordinate system, O_O, coincides with O_B, the axis Z_O follows the radial direction respect to the Sun, while the orientation of X_O is given by $\mathbf{i}_O = (\mathbf{k}_H \times \mathbf{k}_O)/\parallel \mathbf{k}_H \times \mathbf{k}_O \parallel$ and Y_O completes the right-hand frame. Finally the origin O_I of inertial coordinate system (I), is coincident to the position of O_B for the initial time t_0 and is given by the position vector $\mathbf{R}_0$. Moreover, the I frame is parallel to the H frame, and is the inertial frame used for the formulation of the problem. Consequently, the position of any point of the flexible or rigid bodies $\mathbf{r}$, is referenced to it and is related to the position respect H frame by $\mathbf{R} = \mathbf{R}_0 + \mathbf{r}$. The introduction and use of the I frame is justified due to the significant differences in the order of magnitude of the dimensions involved in the dynamical problem and the finite precision limitation associated to numerical methods. For the short term dynamical analyses carried out in the present work, the definition of the I frame allows to reduce the order of magnitude of the positions by the use of r instead of R, which for 1 AU is of the order of 10^{12} m at the initial instant, notably large in comparison to the dimensions of the central vehicle of the order of 1 m. This disparity on the order of magnitude in addition to the finite precision associated to double precision arithmetic, which provides sixteen significance figures, leads to the abatement of the precision limit during the integration and can be partially avoided for short term simulations by the introduction of the I frame.

Additionally, the E-sail coordinate system E is introduced in Fig.1(c). This auxiliary frame defines the orientation of the plane Π, which is established as the mean plane of the remote units. The frame origin O_E is located at the projection of the center of mass of the remote units on the plane Π, the orientation of the X_E axis is given by the normal vector $\tilde{\mathbf{n}}$, and Y_E is given by the position of the remote mass of the first tether u_1. Z_E completes the right-hand frame.

For the sake of understanding, the superscript is used to indicate the frame in which a variable is expressed, e.g. $\mathbf{r}^O$ indicates position given in orbital frame O. When omitted, the variable is given in I frame. Additionally, the orientation of frame J respect to frame K is defined by the director cosines matrix C_J^K, for $J, K = H, B, O, I, E$, for example $\mathbf{r}^I = C_O^I \mathbf{r}^O$.

2.2. Formulation of cable element based on ANCF

The definition of the cable element selected for the modelling of the E-sail's tethers is presented in the current section. The expressions of generalized forces and Jacobian matrices of the contribution are introduced.

The absolute nodal coordinate formulation considered, is a non-incremental nonlinear finite element procedure proposed in [41, 42], and extensively used for analysing the dynamics of flexible bodies that experience large rotations and deformations. It should be remarked, that, with the aim of simplifying the expressions, the sub-indexes indicating the number of FE and tether have been omitted. Similarly, the super-index e, used in Sect. 2 to identify the flexible character of the contributions on the assembly of the system matrices or vectors, is also excluded, e.g. the denomination of the mass matrix of the j^{th} finite element of tether i, defined as $\mathbf{M}_{ij}^e$ in Sect. 2, is simply referred to as $\mathbf{M}$. Moreover, to facilitate the understanding, part of the expressions are provided in the Appendix A. It should be mentioned that the evaluations of the final expressions containing integral terms, presented in the current Section and in the Appendix A, are carried out by means of Gaussian integration.

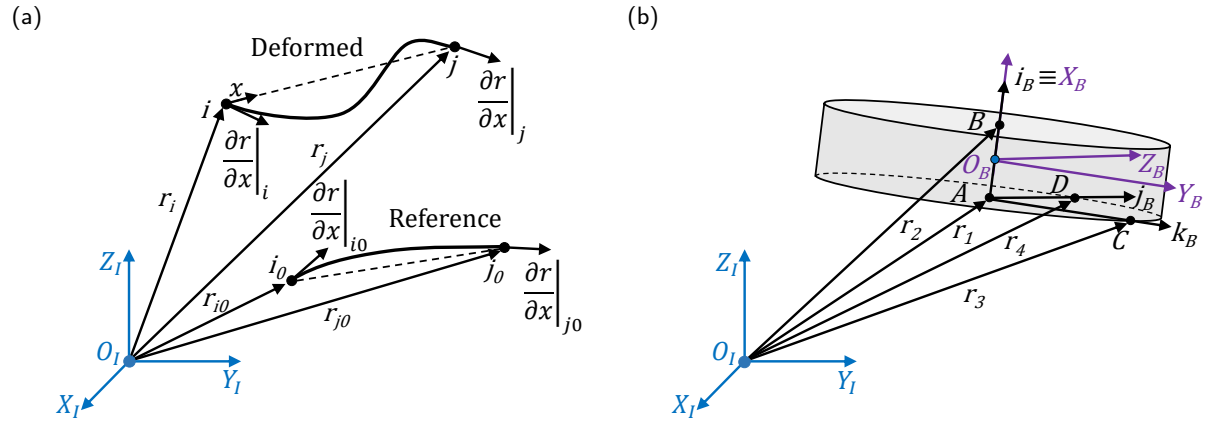

Figure 2: Description of the generalized nodal coordinates for cable element and rigid body: (a) Tether modelling based on a gradient-deficient cable element defined on ANCF, where nodal positions and longitudinal slopes are considered as nodal coordinates. Reference and deformed configurations are displayed; and (b) Base points and body frame considered for the rigid body NC formulation used to model the central spacecraft.

At a given instant, the position of any point of the volume of any finite element of a given tether can be interpolated by

$$\mathbf{r}(x,t) = \mathbf{S}(x)\,\mathbf{e}(t)\,, \tag{16}$$

being $\mathbf{r}(x)$ the coordinate of the point defined in the inertial global coordinate system I, $\mathbf{S}(x)$ is the 3×12 matrix of shape functions defined in Eq. (17) and $\mathbf{e}$ the vector of nodal coordinates of the flexible cable element, whose dimensions are 12×1. According to the formulation for gradient deficient cable elements proposed in [46] and illustrated in Fig. 2(a), one has

$$\mathbf{S}(x) = \begin{bmatrix} s_1\mathbf{I} & s_2\mathbf{I} & s_3\mathbf{I} & s_4\mathbf{I} \end{bmatrix}, \tag{17}$$

where $\mathbf{I}$ is the 3x3 identity matrix and l is the length of the element, which is used to define the normalized position $\xi = x/l$, that allows to write the shape functions

$$s_1 = 1 - 3\xi^2 + 2\xi^3,\ s_2 = l(\xi - 2\xi^2 + \xi^3),\ s_3 = 3\xi^2 - 2\xi^3,\ s_4 = l(-\xi^2 + \xi^3). \tag{18}$$

The set of generalized nodal coordinates for each element, includes the position and the longitudinal slope defined in I frame, at both the initial and end nodes, being

$$\mathbf{e}(t) = \begin{bmatrix} \mathbf{r}_i(t)^T & \mathbf{r}_{i,x}(t)^T & \mathbf{r}_j(t)^T & \mathbf{r}_{j,x}(t)^T \end{bmatrix}^T, \tag{19}$$

where $\mathbf{r}_i(t)$ represents the position and $\mathbf{r}_{i,x}(t) = \left.\frac{\partial \mathbf{r}(t)}{\partial x}\right|_i$ is the longitudinal slope at initial node i. The same definition applies to the final node j. As already mentioned, this formulation of the cable element is gradient deficient, given that only the slope respect to the local x axis is considered. This selection of nodal coordinates and shape functions removes the shear terms, avoiding the related inefficiencies and locking issues, and allows to account for the nonlinear bending effects which have been found to be crucial for the analysis of low tension or rotating beams [74]. An additional consequence is that torsion can't be modelled with the use of this formulation [46].

2.2.1. Kinetic energy and inertial forces

The velocity of any point of the element, calculated as the time derivative of Eq. (16), can be written as

$$\dot{\mathbf{r}}(x,t) = \mathbf{S}\,\dot{\mathbf{e}}, \tag{20}$$

where for simplicity, the spatial and time dependence is omitted from this point onward. Assuming that the cable is straight in the reference configuration, the elemental kinetic energy T is expressed as

$$T = \frac{1}{2}\dot{\mathbf{e}}^T \mathbf{M}\,\dot{\mathbf{e}}, \tag{21}$$

where $\mathbf{M}$ is the constant generalized element mass matrix, calculated as

$$\mathbf{M} = \int_V \rho_t\,\mathbf{S}^T\mathbf{S}\,\mathrm{d}V = \rho_t\,A_t\int_0^l \mathbf{S}^T\mathbf{S}\,\mathrm{d}x, \tag{22}$$

where the elemental length have been defined as $l = L_0/(n-1)$, being L_0 the undeformed length of a tether and n the number of nodes per tether.

2.2.2. Strain energy and elastic forces

The elastic forces associated to the selected ANCF cable element are described in the current section. It should be noted that, in addition to the axial stiffness, the cable element also accounts for the bending stiffness, and it is selected in the current work in order to improve the level of accuracy of the E-sail model. If only the axial contributions are considered, the formulation presented in this section leads to the formulation of a truss element, in line with previous works [28–30, 32], in which truss elements in NPFEM are used.

In opposition to the direct and simple calculation previously presented for the elemental mass matrix, the use of absolute nodal coordinates leads to a more complex formulation of the strain energy and the elastic forces, as it is shown in this Section. The calculation of the energy, the generalized forces and the Jacobian matrices is introduced here, but the final expressions are presented in Appendix A.1, for the sake of brevity. It should be noted that, to ensure the best computing performance, when possible, the generalized forces and Jacobian matrices are expressed in terms of invariant matrices to avoid the computation of integrals for each element in every step. In the practice, the use of invariant terms is feasible only for axial contributions but not for nonlinear bending members.

The elastic energy for a cable element, denoted U_e, can be formulated based on the Euler-Bernoulli beam [46], comprising the axial U_{e_x}, and the bending U_{e_b} contributions

$$U_e = U_{e_x} + U_{e_b} = \frac{1}{2}\int_0^l E_t A_t\,\epsilon_{xx}^2\,\mathrm{d}x + \frac{1}{2}\int_0^l E_t I_t \kappa^2\,\mathrm{d}x, \tag{23}$$

being dependant of the material modulus of elasticity E_t, the cross-section area A_t and the cross section moment of inertia I_t, which are considered constant along the element. Additionally, the longitudinal axial strain ϵ_{xx}, and the curvature κ, are defined as

$$\epsilon_{xx} = \frac{1}{2}(\mathbf{r}_{,x}^T\mathbf{r}_{,x} - 1)\,,\ \kappa = \frac{\parallel \mathbf{r}_{,x}\times\mathbf{r}_{,xx}\parallel}{\parallel \mathbf{r}_{,x}\parallel^3}, \tag{24}$$

where $\mathbf{r}_{,x}$ and $\mathbf{r}_{,xx}$ are the first and second partial derivative of the position respect to x, respectively. The generalized elastic forces $\mathbf{Q}_e$ are defined by the derivation of the elastic energy function established in Eq. (23), respect to the elemental generalized coordinates $\mathbf{e}$, as:

$$\mathbf{Q}_e = -\left(\frac{\partial \mathbf{U}_e}{\partial \mathbf{e}}\right)^T = \mathbf{Q}_{e_x} + \mathbf{Q}_{e_b}, \tag{25}$$

where the axial and bending contributions are established as $\mathbf{Q}_{e_x} = -\left(\partial \mathbf{U}_{e_x}/\partial \mathbf{e}\right)^T$ and $\mathbf{Q}_{e_b} = -\left(\partial \mathbf{U}_{e_b}/\partial \mathbf{e}\right)^T$. And finally, the Jacobian of the elastic forces $\partial\mathbf{Q}_e/\partial\mathbf{e}$ can be written in terms of the axial $\partial\mathbf{Q}_{e_x}/\partial\mathbf{e}$, and bending contributions $\partial\mathbf{Q}_{e_b}/\partial\mathbf{e}$ as:

$$\frac{\partial \mathbf{Q}_e}{\partial \mathbf{e}} = \frac{\partial \mathbf{Q}_{e_x}}{\partial \mathbf{e}} + \frac{\partial \mathbf{Q}_{e_b}}{\partial \mathbf{e}}. \tag{26}$$

2.2.3. Coulomb forces

The formulation of the Coulomb forces, exerted by the solar wind on the tethered under a difference of electric power respect to the solar wind, is described in this section.

The estimation of the thrust generated on a charged wire under the influence of the solar wind, has been investigated considering different approaches and leading to definition of various thrust models for the prediction of the propulsive force [3–7]. Although the predictions of the induced forces, calculated using the previous mentioned models, lead to notable quantitative differences, it has been shown that the impact of the thrust model considered on the E-sail dynamics is negligible [30]. The approximation proposed in [16], valid for a tether exposed to the solar wind at 1U from the Sun, is considered in the current work. Under these conditions, the magnitude of the thrust force per unit of length of a single tether can be estimated as:

$$\sigma \approx 0.18 \max\left(0, V_0 - V_1\right) \sqrt{\epsilon_0 P_{dyn}}, \tag{27}$$

where V_0 is the tether voltage (typically between 15-40 kV), V_1 represents the voltage corresponding to the bulk kinetic energy of a solar wind proton and ϵ_0 stands for the vacuum permittivity, equal to $8.854 \times 10^{-12}\,\mathrm{F\,m^{-1}}$. Additionally, P_{dyn} is the solar wind dynamic pressure defined as

$$P_{dyn} = m_i n_0 u^2, \tag{28}$$

being m_i the solar wind proton mass, n_0 the solar wind plasma density and u the magnitude of the bulk solar wind speed. At 1 AU, the average values for solar wind parameters are $V_1 = 1\,\mathrm{kV}$, $u = 400\,\mathrm{km/s}$, $n_0 = 7.3\,\mathrm{cm^{-3}}$ and $m_i = 1.67 \times 10^{-27}\,\mathrm{kg}$. Keeping in mind that the effective force per unit of length is exclusively due to the component of the solar wind perpendicular to the tether, the resultant force vector per unit of length $\mathbf{f}_c$, expressed in N/m, can be written as [34]

$$\mathbf{f}_c = 0.18 \max(0, V_0 - V_1) \sqrt{\epsilon_0 m_i n_0}\, \mathbf{u}_\perp, \tag{29}$$

where $\mathbf{u}_\perp$ is the aforementioned component of the solar wind perpendicular to the tether, which can be calculated as

$$\mathbf{u}_\perp = \mathbf{u} - (\mathbf{i}_t^T \mathbf{u})\mathbf{i}_t = \left(\mathbf{I} - \mathbf{i}_t \mathbf{i}_t^T\right) \mathbf{u} = \tilde{\mathbf{I}}\mathbf{u}, \tag{30}$$

being $\mathbf{u}$ the solar wind velocity vector, and $\mathbf{i}_i$ the tether tangent vector, defined as $\mathbf{i}_t = \mathbf{r}_{,x} / \parallel \mathbf{r}_{,x} \parallel$. The matrix $\tilde{\mathbf{I}}$ can be written in terms of the component of the slope $\mathbf{r}_{,x}$ as

$$\tilde{\mathbf{I}} = \frac{1}{\mathbf{r}_{,x}^T \mathbf{r}_{,x}} \begin{bmatrix} \mathbf{r}_{2,x}^2 + \mathbf{r}_{3,x}^2 & -\mathbf{r}_{1,x}\mathbf{r}_{2,x} & -\mathbf{r}_{1,x}\mathbf{r}_{3,x} \\ -\mathbf{r}_{1,x}\mathbf{r}_{2,x} & \mathbf{r}_{1,x}^2 + \mathbf{r}_{3,x}^2 & -\mathbf{r}_{2,x}\mathbf{r}_{3,x} \\ -\mathbf{r}_{1,x}\mathbf{r}_{3,x} & -\mathbf{r}_{2,x}\mathbf{r}_{3,x} & \mathbf{r}_{1,x}^2 + \mathbf{r}_{2,x}^2 \end{bmatrix}. \tag{31}$$

Under the assumption of radial evolution of the solar wind, the velocity vector $\mathbf{u}$, expressed in terms of the heliocentric unitary position vector $\mathbf{i}_R$, becomes $\mathbf{u} = u\,\mathbf{i}_R$. Where for every point, the unitary vector $\mathbf{i}_R$ can be expressed as

$$\mathbf{i}_R = \frac{\mathbf{R}}{\parallel \mathbf{R} \parallel} = \frac{\mathbf{R}_0 + \mathbf{S}\mathbf{e}}{\parallel \mathbf{R}_0 + \mathbf{S}\mathbf{e} \parallel}, \tag{32}$$

being $\mathbf{R}$ the position of the point of the tether respect to the origin of frame H and which is equal to the sum of $\mathbf{R}_0$, which represents position of the origin of the inertial frame I respect to the H system, and the absolute coordinates of the tether point, $\mathbf{r}$, respect to the I frame.

The virtual work of the generalized Coulomb force over an element δW_{fc}, can be established as

$$\delta W_{fc} = \int_0^l \delta \mathbf{e}^T \mathbf{S}^T \mathbf{f}_c \, \mathrm{d}x, \tag{33}$$

and the generalized Coulomb forces on an element $\mathbf{Q}_c$, is obtained from the virtual work as

$$\mathbf{Q}_c = \frac{\delta W_{fc}}{\delta \mathbf{e}} = \int_0^l \mathbf{S}^T \mathbf{f}_c \, \mathrm{d}x. \tag{34}$$

To conclude the formulation of the Coulomb forces, the Jacobian matrix of the generalized forces can be calculated by the derivation of $\mathbf{Q}_c$ respect to generalized coordinates $\mathbf{e}$. Considering the dependence of the term $\partial \mathbf{u}_\perp / \partial \mathbf{e}$ respect to $\mathbf{e}$, the following integral expression is obtained

$$\frac{\partial \mathbf{Q}_c}{\partial \mathbf{e}} = 0.18 \max(0, V_0 - V_1)\sqrt{\epsilon_0 m_i n_0} \int_0^l \mathbf{S}^T \frac{\partial \mathbf{u}_\perp}{\partial \mathbf{e}} \, \mathrm{d}x. \tag{35}$$

2.2.4. Damping energy and forces

The dissipation effects associated to the structural damping are included in the formulation of the cable elements as described in the current Section. The consideration of this term is significant with respect to the ANCF cable elements previously proposed for the E-sail dynamics [34, 62].

Based on the Rayleigh dissipation function presented in [75], the power dissipated by the internal damping on an Euler-Bernoulli beam, P_d is established as

$$P_d = P_{d_x} + P_{d_b} = \frac{1}{2}\int_0^l N_{x_v}\dot{\epsilon}_{xx} \, \mathrm{d}x + \frac{1}{2}\int_0^l M_{b_v}\dot{\kappa} \, \mathrm{d}x, \tag{36}$$

where $N_{x_v} = E_t A_t \gamma_x \dot{\epsilon}_{xx}$ and $M_{b_v} = \gamma_b E_t I_t \dot{\kappa}$ are the viscous components of the internal forces, assuming that the viscoelastic effects can be included in the definition of internal axial force as $N_x = E_t A_t \left(\epsilon_{xx} + \gamma_x \dot{\epsilon}_{xx}\right)$ and similarly in the bending moment as $M_b = E_t I_t \left(\kappa + \gamma_b \dot{\kappa}\right)$. Where γ_x and γ_b are the damping coefficients associated to axial and bending components, respectively. Both coefficients are defined equal to 1.00, corresponding to a damping factor of 2.30% for the configuration considered. Subsequently, the damping forces are calculated by derivation of the dissipation function respect to the generalized velocities

$$\mathbf{Q}_d = -\left(\frac{\partial P_d}{\partial \dot{\mathbf{e}}}\right)^T = -\left(\frac{\partial P_{d_x}}{\partial \dot{\mathbf{e}}}\right)^T - \left(\frac{\partial P_{d_b}}{\partial \dot{\mathbf{e}}}\right)^T, \tag{37}$$

and finally, the Jacobian matrix of the generalized damping forces is defined as

$$\frac{\partial \mathbf{Q}_d}{\partial \mathbf{e}} = \frac{\partial \mathbf{Q}_{d_x}}{\partial \mathbf{e}} + \frac{\partial \mathbf{Q}_{d_b}}{\partial \mathbf{e}}. \tag{38}$$

For the sake of comprehension, the extended formulation of the damping terms is provided in Appendix A.2.

2.3. Formulation of rigid element in NC

The dynamics of the central rigid body is established in the present section. The vector of generalized coordinates associated to the rigid body is established, the formulation of the internal constraints is exposed, and the definitions of the inertial generalized forces and Jacobian matrices are provided.

The formulation is carried out considering a set of natural coordinates formed by the positions of four non co-planary base points A, B, C and D depicted in Fig. 2(b). Consequently, a total of 12 generalized coordinates are needed. This selection of the natural coordinates enables a constant mass matrix [76] and enforces the formulation of 6 internal constraint equations. For the sake of readiness, the super-index r, used in the introduction of Sect. 2 to identify the contributions of the rigid body to the system matrices or vectors, is excluded, e.g. the denomination of the mass matrix of the rigid body, defined as $\mathbf{M}^r$ in Eq. (11), is simply referred to as $\mathbf{M}$ in this section.

The position of any point of the solid can be written as

$$\mathbf{r}(\mathbf{x}, t) = \mathbf{G}(\mathbf{x})\,\mathbf{d}(\mathbf{t}), \tag{39}$$

where $\mathbf{d}$ is the generalized coordinates vector formed by the concatenation of the coordinates of the four base points

$$\mathbf{d} = \begin{bmatrix}\mathbf{r}_1^T & \mathbf{r}_2^T & \mathbf{r}_3^T & \mathbf{r}_4^T\end{bmatrix}^T, \tag{40}$$

and $\mathbf{G}$ is a constant matrix that can be computed from the local coordinates of the base points, as described in Appendix B. Given the vector of generalized coordinates of the rigid body, $\mathbf{d}$, the rotation matrix $\mathbf{C}_B^I$, associated with the transformation from the local frame, parallel to B, to the global frame I, can be computed as:

$$C_B^I = \begin{bmatrix}\mathbf{r}_{AB} & \mathbf{r}_{AC} & \mathbf{r}_{AD}\end{bmatrix}\begin{bmatrix}\boldsymbol{\alpha} & \boldsymbol{\beta} & \boldsymbol{\gamma}\end{bmatrix}. \tag{41}$$

where the auxiliary vectors $\mathbf{r}_{AB}$, $\mathbf{r}_{AC}$ and $\mathbf{r}_{AD}$ are calculated based on the positions of the basic points A-D defined in Fig. 2(b) as

$$\mathbf{r}_{AB} = \mathbf{r}_2 - \mathbf{r}_1,\ \mathbf{r}_{AC} = \mathbf{r}_3 - \mathbf{r}_1,\ \mathbf{r}_{AD} = \mathbf{r}_4 - \mathbf{r}_1, \tag{42}$$

and the constant vectors $\boldsymbol{\alpha}$, $\boldsymbol{\beta}$ and $\boldsymbol{\gamma}$ can be computed in base of the local position of the base nodes as described in Appendix B. Additionally, the position of the origin of frames B and O, which are coincident, can be computed from the coordinates of points A and B of the rigid body as

$$\mathbf{r}_{O_B} \equiv \mathbf{r}_{O_O} = 1/2\,(\mathbf{r}_1 + \mathbf{r}_2) = 1/2\,(\mathbf{B}_1^r + \mathbf{B}_2^r)\mathbf{q}, \tag{43}$$

where $\mathbf{B}_1^r$ and $\mathbf{B}_2^r$ are the Boolean matrices that extract the basic points' coordinates of the rigid body defined as per Eq. (10). Once the position of the origin $\mathbf{r}_{O_O}$ is known, the orientation of the Z_O axis is calculated as

$$\mathbf{k}_O = \frac{\mathbf{R}_0 + \mathbf{r}_{O_B}}{\| \mathbf{R}_0 + \mathbf{r}_{O_B} \|}. \tag{44}$$

2.3.1. Rigid body constraints

This section contains the definition of the six internal constraint necessary for the rigid body formulation.

The NC formulation considered for the rigid body contains twelve generalized coordinates, hence six constraint are needed. Two types of constrains are introduced: three equations to impose that the distances between pairs of base points remain constant, and three additional equations to enforce that the angles formed between the auxiliary vectors $\mathbf{r}_{AK}$ are invariable, for $K = B, C, D$. The set of internal constraints $\mathbf{C}_r$, can be written as

$$\mathbf{C}_r = \begin{bmatrix} \mathbf{r}_{AB}^T\mathbf{r}_{AB} - L_{AB}^2 \\ \mathbf{r}_{AC}^T\mathbf{r}_{AC} - L_{AC}^2 \\ \mathbf{r}_{AD}^T\mathbf{r}_{AD} - L_{AD}^2 \\ \mathbf{r}_{AC}^T\mathbf{r}_{AB} - \cos(\widehat{BAC})L_{AB}L_{AC} \\ \mathbf{r}_{AD}^T\mathbf{r}_{AB} - \cos(\widehat{BAD})L_{AB}L_{AD} \\ \mathbf{r}_{AD}^T\mathbf{r}_{AC} - \cos(\widehat{DAC})L_{AD}L_{AC} \end{bmatrix} = \begin{bmatrix} 0 \\ 0 \\ 0 \\ 0 \\ 0 \\ 0 \end{bmatrix}, \tag{45}$$

being L_{AB} the distance between the points A and B, and $\widehat{BAC}$ the angle formed by the vectors $\mathbf{r}_{AB}$ and $\mathbf{r}_{AC}$, which are defined going from point A to point B, and from point A to C respectively. The rest of the parameters involved are comparatively defined, being all of them constant and equal to their initial values.

Based on the strict dependence of $\mathbf{C}_r$ on rigid body natural coordinates $\mathbf{d}$, the Jacobian matrix of the rigid constraint vector $\mathbf{C}_r$ can be expressed as

$$\mathbf{C}_{r,d} = \frac{\partial \mathbf{C}_r}{\partial \mathbf{d}} = \begin{bmatrix} -2\mathbf{r}_{AB}^T & 2\mathbf{r}_{AB}^T & \mathbf{0}_{1x3} & \mathbf{0}_{1x3} \\ -2\mathbf{r}_{AC}^T & \mathbf{0}_{1x3} & 2\mathbf{r}_{AC}^T & \mathbf{0}_{1x3} \\ -2\mathbf{r}_{AD}^T & \mathbf{0}_{1x3} & \mathbf{0}_{1x3} & 2\mathbf{r}_{AD}^T \\ -\mathbf{r}_{AB} - \mathbf{r}_{AC} & \mathbf{r}_{AC} & \mathbf{r}_{AB} & \mathbf{0}_{1x3} \\ -\mathbf{r}_{AB} - \mathbf{r}_{AD} & \mathbf{r}_{AD} & \mathbf{0}_{1x3} & \mathbf{r}_{AB} \\ -\mathbf{r}_{AC} - \mathbf{r}_{AD} & \mathbf{0}_{1x3} & \mathbf{r}_{AD} & \mathbf{r}_{AC} \end{bmatrix}, \tag{46}$$

which can be straightaway expressed in terms of system generalized coordinates $\mathbf{q}$, as $\mathbf{C}_{r,q} = \mathbf{C}_{r,d}\mathbf{B}^r$. Furthermore, the contribution of the internal constraints to the term $\partial\left(\boldsymbol{\mathscr{C}}_{,q}^T\boldsymbol{\lambda}\right)/\partial\mathbf{q}$ of the tangent matrix $\mathbf{S}_t$, established by Eq. (13), is presented next. Keeping into consideration, the definition of the auxiliary vector $\mathbf{D} = \mathbf{C}_{r,q}^T\boldsymbol{\lambda}_r$, where $\boldsymbol{\lambda}_r$ is the Lagrange multipliers vector associated to rigid body constraints, its components can be expressed as

$$\mathbf{D}_i = \sum_{j=1}^{6} \mathbf{C}_{r,d_{ji}}\boldsymbol{\lambda}_{r_j}, \tag{47}$$

and subsequently, the component in row i and column k of the matrix $\partial\left(\mathbf{C}_{r,d}^{T}\boldsymbol{\lambda}_{r}\right)/\partial\mathbf{d}$ can be established as:

$$\frac{\partial\left(\mathbf{C}_{r,d}^{T}\boldsymbol{\lambda}_{r}\right)_{i}}{\partial\mathbf{d}_{k}}=\frac{\partial\sum_{j=1}^{6}\mathbf{C}_{r,d_{ji}}\boldsymbol{\lambda}_{r_{j}}}{\partial\mathbf{d}_{k}}=\sum_{j=1}^{6}\frac{\partial\mathbf{C}_{r,d_{ji}}}{\partial\mathbf{d}_{k}}\boldsymbol{\lambda}_{r_{j}}. \tag{48}$$

Finally and as in the previous case, the Jacobian in terms of $\mathbf{q}$ can be easily calculated by

$$\frac{\partial(\mathbf{C}_{r,q}^{T}\boldsymbol{\lambda}_{r})}{\partial\mathbf{q}}=\frac{\partial(\mathbf{C}_{r,d}^{T}\boldsymbol{\lambda}_{r})}{\partial\mathbf{d}}\mathbf{B}^{r}. \tag{49}$$

2.3.2. Kinetic energy and inertial forces

The inertial terms of the rigid body are described in the current section.

The velocity of any point of the solid can be calculated by differentiation of the position respect to the inertial frame I, given by Eq. (39), respect to the time as

$$\dot{\mathbf{r}}=\mathbf{G}\dot{\mathbf{d}}, \tag{50}$$

that allows to define the kinetic energy of the solid by the integral

$$T=\frac{1}{2}\int_{V}\rho_{r}\,\dot{\mathbf{r}}^{2}\,\mathrm{d}V=\frac{1}{2}\dot{\mathbf{d}}^{T}\mathbf{M}\,\dot{\mathbf{d}}, \tag{51}$$

where $\mathbf{M}$ is the rigid body generalized constant mass matrix defined as

$$M=\rho_{r}\int_{V}\mathbf{G}^{T}\,\mathbf{G}\,\mathrm{d}V. \tag{52}$$

2.4. Formulation of spherical joints

The coupling condition between the rigid body and the flexible cables representing the tethers is described in this section.

The joint between the tethers and the central vehicle is applied by imposing that the positions of the points at the anchor points, in both the rigid and the flexible parts, remain coincident. The joint is referred to as spherical joint given that the coupling is limited to the displacements. This condition can be formulated considering the definition of the position of an arbitrary point established for the cable elements in Eq. (16) and for the rigid body as per Eq. (39). The vector of constraints equations $\mathbf{C}_{a}=\left[\hat{\mathbf{C}}_{a}(1)^{T}\;\hat{\mathbf{C}}_{a}(2)^{T}\;...\hat{\mathbf{C}}_{a}(p)^{T}\right]^{T}$, of dimensions $3p\times1$, is the vertical concatenation of the unitary spherical joint equations $\hat{\mathbf{C}}_{a}(i)$, for the constrains equation matrices associated to the anchor points $i=1,2,...p$. For an arbitrary tether i, the joint equations can be written as

$$\hat{\mathbf{C}}_{a}(i)=\mathbf{G}(\mathbf{x}_{i})\,\mathbf{d}-\mathbf{S}(0)\,\mathbf{e}_{i1}=\mathbf{G}(\mathbf{x}_{i})\mathbf{B}^{r}\mathbf{q}-\mathbf{S}(0)\,\mathbf{B}_{i1}^{e}\mathbf{q}=0 \tag{53}$$

where $\mathbf{e}_{i1}$ are the generalized coordinates of the first element of the tether i, $\mathbf{S}$ is the shape function matrix, evaluated at $x=0$, that corresponds to the local coordinate of the anchor point expressed in the cable frame. Furthermore, $\mathbf{d}$ is the generalized coordinate vector of the rigid body and the matrix $\mathbf{G}$, defined in Eq. (131), is evaluated in $\mathbf{x}_{i}$, that corresponds to the local coordinate vector of the anchor point i, expressed in the local frame of the rigid body, and, according to Fig. 2(b), is equal to:

$$\mathbf{x}_{i}=\left[h_{r}/2\mid R_{r}\cos(2\pi\,i/p)\mid R_{r}\sin(2\pi\,i/p)\right]^{T}, \tag{54}$$

where R_{r} and h_{r} are the central body external radius and height. The Jacobian of the constraint equations with respect to the vector of generalized coordinates $\mathbf{q}$, can be written as

$$\frac{\partial\hat{\mathbf{C}}_{a}(i)}{\partial\mathbf{q}}=\mathbf{G}(\mathbf{x}_{i})\mathbf{B}^{r}-\mathbf{S}(0)\,\mathbf{B}_{i1}^{e}, \tag{55}$$

which is independent of the generalized coordinates of the system $\mathbf{q}$.

3. Definition of auxiliary variables

In order to facilitate the understanding of the E-sail motion and attitude evolution, which may not be direct for the generalized coordinates used in the formulation presented in Sect. 2, a set of auxiliary dynamic and attitude variables are defined in this Section and used subsequently in Sect. 4 to present the analyses results.

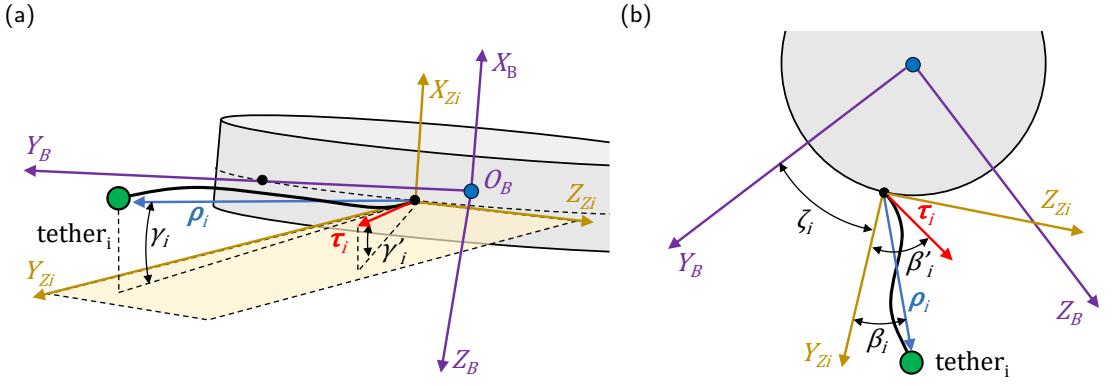

Figure 3: Description of the angular magnitudes establishing the relative position of the remote unit and the tether slope at the root, expressed in the local coordinate system Z_i: (a) Definition of the coning angle γ_i, establishing the vertical position of the remote unit, and the root coning angle γ'_i, describing the vertical component of the longitudinal slope of the tether at the root; and (b) Definition of the lagging angle β_i, establishing the azimuthal position of the remote unit, and the root lagging angle β'_i, describing the horizontal component of the longitudinal slope of the tether at the root.

3.1. Coning and lagging angles

The relative motion of the remote unit with respect to the anchor point, is established by the coning angle, γ_i, and lagging angle, β_i, defined in Figs. 3(a) and (b), respectively.

The relative position of the remote unit i respect to the corresponding anchor point, expressed in the I frame, $\boldsymbol{\rho}_i^I$, is given by

$$\boldsymbol{\rho}_i^I = \hat{\mathbf{B}}^p \left(\hat{\mathbf{B}}_{in}^e - \hat{\mathbf{B}}_{i1}^e \right) \mathbf{q}, \tag{56}$$

where the Boolean matrices $\hat{\mathbf{B}}_{i1}^e$ and $\hat{\mathbf{B}}_{in}^e$ for initial and final node of tether i are defined in Sect. 2 and the definition of $\hat{\mathbf{B}}^p = \left[\mathbf{I}_{3\times3}\, \mathbf{0}_{3\times3}\right]$ allows the extraction of the position coordinates from the nodal generalized coordinates vector. Bearing in mind Fig. 3, a local frame Z is defined for tether i. Its origin O_Z, is located at the corresponding anchor point, and its axes are the result of transforming the body frame B by the matrix

$$\mathbf{C}_B^Z(\zeta_i) = \begin{bmatrix} 1 & 0 & 0 \\ 0 & \cos\zeta_i & \sin\zeta_i \\ 0 & -\sin\zeta_i & \cos\zeta_i] \end{bmatrix}, \tag{57}$$

which corresponds to a rotation of angle ζ_i along the X_B axis. For the tether i, the angular position respect to the Y_B axis is given by $\zeta_i = 2\pi(i-1)/p$, and the vector $\boldsymbol{\rho}_i^I$ can be transformed to the local Z frame by the expression

$$\boldsymbol{\rho}_i^Z = \mathbf{C}_B^Z \left(\mathbf{C}_B^I\right)^T \boldsymbol{\rho}_i^I, \tag{58}$$

where $\mathbf{C}_B^I$ establishes the orientation of the body frame respect to the inertia frame and is calculated as per Eq. (41). Based on the previous definition, the angles γ_i and β_i are defined in terms of the component of the relative position vector $\boldsymbol{\rho}_i^Z$, as

$$\gamma_i = \tan^{-1}\left(\frac{\rho_{i_1}^Z}{\left(\rho_{i_2}^{Z\,2} + \rho_{i_3}^{Z\,2}\right)^{1/2}} \right), \quad \beta_i = \tan^{-1}\left(\frac{\rho_{i_3}^Z}{\rho_{i_2}^Z} \right) \tag{59}$$

where it has been considered that $\boldsymbol{\rho}_i^Z = \left[\rho_{i_1}^Z \; \rho_{i_2}^Z \; \rho_{i_3}^Z\right]^T$.

It can be verified that the same procedure is valid to obtain the expression of the angular variables γ' and β' defining the orientation of the longitudinal slope of the cable at the root and referred to as root coning and root lagging angles, respectively. Both magnitudes are depicted in Figs. 3(a) and (b). Instead of $\boldsymbol{\rho}_i^I$, the generalized coordinates defining the cable tangent at the anchor point ${\boldsymbol{\tau}_i}^I$, should be used

$$ {\boldsymbol{\tau}_i}^I = \hat{\mathbf{B}}^s \hat{\mathbf{B}}_{i1}^e \, \mathbf{q}, \tag{60} $$

where the slope coordinates can be extracted by the use of the matrix $\hat{\mathbf{B}}^s$, defined as $\hat{\mathbf{B}}^s = \left[\mathbf{0}_{3\times3} \, \mathbf{I}_{3\times3}\right]$. The previous definitions allow to write the following expression for γ_i' and β_i':

$$ \gamma_i' = \tan^{-1}\left(\frac{\tau_{i_1}^Z}{\left({\tau_{i_2}^Z}^2 + {\tau_{i_3}^Z}^2\right)^{1/2}}\right), \; \beta_i' = \tan^{-1}\left(\frac{\tau_{i_3}^Z}{\tau_{i_2}^Z}\right), \tag{61} $$

where the definition $\boldsymbol{\tau}_i^Z = \left[\tau_{i_1}^Z \; \tau_{i_2}^Z \; \tau_{i_3}^Z\right]^T$ has been considered.

3.2. Main spacecraft angular rates

The angular motion of the central vehicle is defined in this section by the establishment of the angular velocity vector $\boldsymbol{\omega}^{\boldsymbol{B}} = [\omega_1 \, \omega_2 \, \omega_3]^T$, representing the absolute angular velocity of the B frame with respect to the I coordinate system, and expressed in the B frame.

Consider the position of a point in the rigid body, given by Eq. (128), and whose time derivative can be written as

$$ \dot{\mathbf{r}} = \dot{\mathbf{r}}_1 + \mathbf{C}_B^I \, \widetilde{\boldsymbol{\omega}}^B \, \mathbf{x}, \tag{62} $$

where $\widetilde{\boldsymbol{\omega}}^B$ is the skew matrix defined for $\boldsymbol{\omega}^B$ and $\mathbf{x}$ are the local coordinates of a point on the rigid expressed in the body frame. Given the location selected for the base points used to formulate the rigid body, and presented in Sect. 2.3, their local coordinates are $\mathbf{x}_B = \left[h_r \, 0 \, 0\right]^T$, $\mathbf{x}_C = \left[0 \; R_r \; 0\right]^T$ and $\mathbf{x}_D = \left[0 \, 0 \; R_r\right]^T$, and since Eq. (62) should be satisfied for the three of them, the following expression are fulfilled

$$ \begin{aligned} \dot{\mathbf{r}}_{AB} &= \dot{\mathbf{r}}_2 - \dot{\mathbf{r}}_1 = \mathbf{C}_B^I \, \widetilde{\boldsymbol{\omega}}^B \mathbf{x}_B, \\ \dot{\mathbf{r}}_{AC} &= \dot{\mathbf{r}}_3 - \dot{\mathbf{r}}_1 = \mathbf{C}_B^I \, \widetilde{\boldsymbol{\omega}}^B \mathbf{x}_C, \\ \dot{\mathbf{r}}_{AD} &= \dot{\mathbf{r}}_4 - \dot{\mathbf{r}}_1 = \mathbf{C}_B^I \, \widetilde{\boldsymbol{\omega}}^B \mathbf{x}_D. \end{aligned} \tag{63} $$

Knowning the generalized coordinates of the solid rigid and their velocities, $\widetilde{\boldsymbol{\omega}}^B$ can be calculated by just concatenating the left and right term of the vector equations in Eq. (63) as

$$ \widetilde{\boldsymbol{\omega}}^B = \mathbf{C}_I^B \, \left[\dot{\mathbf{r}}_{AB} \, \dot{\mathbf{r}}_{AC} \, \dot{\mathbf{r}}_{AD}\right] \, \left[\mathbf{x}_B \, \mathbf{x}_C \, \mathbf{x}_D\right]^{-1}, \tag{64} $$

from which, the absolute angular rate components can be obtained.

3.3. Main spacecraft orientation

The orientation of the main spacecraft body frame B respect to the orbital frame O, is established by the Euler angles ψ, θ and ϕ, which are defined according to the classical sequence

$$ O \xrightarrow[Z^O]{\psi} S \xrightarrow[Y^S]{\theta} S' \xrightarrow[Z^{S'}]{\phi} B. \tag{65} $$

Their values are obtained from the Director Cosines Matrix (DCM) $\mathbf{C}_O^B$, which can be expressed as $\mathbf{C}_O^B = \mathbf{C}_I^B \mathbf{C}_O^I$, where the matrix $\mathbf{C}_I^B$ can be computed from the nodal position of rigid body nodes as indicated in Eq. (41), and $\mathbf{C}_O^I$ is defined as

$$ \mathbf{C}_O^I = \left[\mathbf{X}_O \, \mathbf{Y}_O \, \mathbf{Z}_O\right], \tag{66} $$

being $\mathbf{X}_O, \mathbf{Y}_O, \mathbf{Z}_O$ the axes of the orbital O frame described in Sect. 2.1. Consequently, known $\mathbf{C}_O^B$, the angles ψ, θ and ϕ can be computed following the classical definition and considering the angle θ restricted to the range $[-\pi/2, \pi/2]$ [77].

3.4. E-sail orientation

The current paragraph presents the evaluation of the attitude of the E-sail, expressed in terms of the Euler angles Ψ, Θ and Φ, which generally differs from the attitude of the main spacecraft described in previous Sect. 3.3.

The orientation of the E-sail respect to the orbital frame O, is determined considering the orientation of the auxiliary E-sail frame E, depicted in Fig. 1(c) and defined taking into account the normal vector of plane Π and the location of an arbitrary remote unit. In the formulation exposed, the remote unit associated to tether 1 is considered. The plane Π is defined as the mean plane formed by the position of the remote units, and its normal orientation vector $\tilde{\mathbf{n}}$, is computed as the least square solution of the subsequent linear system of dimensions $p \times 3$

$$\begin{pmatrix} \mathbf{r}_{u_1}^T - \mathbf{r}_{\overline{u}}^T \\ \mathbf{r}_{u_2}^T - \mathbf{r}_{\overline{u}}^T \\ \cdots \\ \mathbf{r}_{u_i}^T - \mathbf{r}_{\overline{u}}^T \\ \cdots \\ \mathbf{r}_{u_p}^T - \mathbf{r}_{\overline{u}}^T \end{pmatrix} \tilde{\mathbf{n}} = \begin{pmatrix} 0 \\ 0 \\ \cdots \\ 0 \\ \cdots \\ 0 \end{pmatrix}, \tag{67}$$

where $\mathbf{r}_{\overline{u}}$ represents the position of the center of gravity of the particle system formed by the remote units, and which can be calculated as

$$\mathbf{r}_{\overline{u}} = \frac{1}{p} \sum_{i=1}^{p} \mathbf{r}_{u_i}, \tag{68}$$

and $\mathbf{r}_{u_i}$ is the position vector of the remote unit associated to the tether i which, taking into account the Boolean matrices defined in Sect. 2, can be extracted from $\mathbf{q}$ as

$$\mathbf{r}_{u_i} = \hat{\mathbf{B}}^p \, \hat{\mathbf{B}}_{in}^e \mathbf{q}. \tag{69}$$

Additionally, the origin of the E frame is located at $\mathbf{r}_{\overline{u}}$, and together with the normal vector $\tilde{\mathbf{n}}$ and the relative location of the remote unit 1, the orientations of the frame axes are computed as it follows

$$\mathbf{i}_E = \frac{\tilde{\mathbf{n}}}{\| \tilde{\mathbf{n}} \|}, \; \mathbf{k}_E = \frac{\mathbf{i}_E \times \left(\mathbf{r}_{u_1}^T - \mathbf{r}_{\overline{u}} \right)}{\left\| \mathbf{i}_E \times \left(\mathbf{r}_{u_1}^T - \mathbf{r}_{\overline{u}} \right) \right\|}, \; \mathbf{j}_E = \mathbf{k}_E \times \mathbf{i}_E. \tag{70}$$

In line with Sect. 3.3, the rotation sequence for the E-sail is established as

$$O \xrightarrow[Z^O]{\Psi} P \xrightarrow[Y^P]{\Theta} P' \xrightarrow[Z^{P'}]{\Phi} E, \tag{71}$$

being P and P' the intermediate frames. Similarly, the expression $\mathbf{C}_O^E = \mathbf{C}_I^E \, \mathbf{C}_O^I$ allows to compute $\mathbf{C}_O^E$, given that $\mathbf{C}_I^E$ is the DCM defining the orientation of frame E respect to the inertial frame I, which can be written in term of the axis orientations as $\mathbf{C}_I^E = [\mathbf{i}_E \, \mathbf{j}_E \, \mathbf{k}_E]$, and the matrix $\mathbf{C}_O^I$ is computed as per Eq. (66). Once $\mathbf{C}_O^E$ is known, the angles Ψ, Θ and Φ can be calculated following the procedure indicated in [77].

Moreover, the definition of the sailing and precession angles, depicted in Fig. 1(b), is of interest to expressly define the orientation of X_E. On one hand, the sailing angle α is established by the orientation of the X_B axis respect to the solar wind direction, which is assumed to be radial and then parallel to Z_O axis, and can be computed as $\alpha = \cos^{-1}\left(\mathbf{i}_B^T \mathbf{k}_O \right)$. On the other hand, the precession angle δ, is measured from X_O to the projection of X_E on the plane $X_O Y_O$, and can be calculated as $\delta = \cos^{-1}\left(i_{E_1}^O \right)$, where the expression of the unitary orientation vector $\mathbf{i}_E$, on the O frame is obtained as $\mathbf{i}_E^O = \mathbf{C}_I^O \mathbf{i}_E$.

3.5. Total forces and moments

To conclude the definition of the auxiliary variables, the calculation of several auxiliary forces and moments magnitudes are presented at this point. It should be noted that some magnitudes provide information related to a single tether and others contain global results referred to the E-sail system.

In relation to the propulsive force extracted from the solar wind by the E-sail system, $\mathbf{F}_c$, it can be calculated as the sum of the contributions of each tether as

$$\mathbf{F}_c = \sum_{i=1}^{p} \mathbf{F}_{ci}, \tag{72}$$

where p is the total number of tethers, and $\mathbf{F}_{ci}$ is the resultant of the Coulomb forces over the tether i. Analogously, $\mathbf{F}_{ci}$ can be computed as the sum of the contribution at each node given by

$$\mathbf{F}_{ci} = \left[\hat{\mathbf{B}}^p \,|\, \mathbf{0}_{3\times 6}\right] \mathbf{Q}^e_{c_{i1}} + \sum_{j=1}^{n-1} \left[\mathbf{0}_{3\times 6} \,|\, \hat{\mathbf{B}}^p\right] \mathbf{Q}^e_{c_{ij}}, \tag{73}$$

where $\mathbf{Q}^e_{c_{ij}}$ is the generalized Coulomb force at element j of tether i, computed as per Eq. (34), and n represents the total number of nodes of a tether. This thrust resultant, expressed in the solution system frame I, can be transformed to the orbital frame as

$$\mathbf{F}^O_c = \mathbf{C}^O_I \mathbf{F}_c, \tag{74}$$

allowing the definition of the axial trust component $F_{c_{ax}} = F^O_{c_3}$, parallel to the Sun rays and the specification of the transversal component $F_{c_{tr}} = \sqrt{\left(F^O_{c_1}\right)^2 + \left(F^O_{c_2}\right)^2}$. Both contributions can be combined to define the thrust angle $\Gamma_c = \tan^{-1}\left(F_{c_{ax}}/F_{c_{tr}}\right)$, that represents the angle formed by $\mathbf{F}_c$ and the axis Z_O and is described in Fig. 1(b).

Additionally, the moment $\mathbf{M}_{ci}$, generated by the distribution of the Coulomb forces along the tether i, and considered respect to the anchor point, is written as

$$\mathbf{M}_{ci} = \sum_{j=1}^{n-1} \hat{\mathbf{B}}^p \left(\hat{\mathbf{B}}^e_{i(j+1)} - \hat{\mathbf{B}}^e_{i1}\right) \mathbf{q} \times \left[\mathbf{0}_{3\times 6} \,|\, \hat{\mathbf{B}}^p\right] \mathbf{Q}^e_{c_{ij}}, \tag{75}$$

where the first factor of the cross product represents the position vector of the node $j+1$ respect to the anchor node, and the second is the Coulomb force at the second node of the j^{th} element of tether i. Moreover, and based on the previous expression, the resultant of the Coulomb moment $\mathbf{M}_c$, can be calculated as

$$\mathbf{M}_c = \sum_{i=1}^{p} \mathbf{M}_{ci}, \tag{76}$$

where it should be noted that this torque is not applied to the central vehicle, given that the tethers are pinned at the root, but it contributes to the evolution of the mean plane Π, defined in Fig. 1(c).

Similarly, the constraints at the tethers' root, associated to the Lagrange multipliers vectors, are also characterized by the introduction of the following variables. The total force applied to the central vehicle can be computed from the sum of the contributions of the Lagrange multipliers at every anchor point $\boldsymbol{\lambda}_i$ as

$$\mathbf{F}_\lambda = \sum_{i=1}^{p} \boldsymbol{\lambda}_i, \tag{77}$$

where the Lagrange multipliers vectors $\boldsymbol{\lambda}_i$, are directly obtained from the solution of the DAE system at each time step. Similarly to the thrust force, the applied force can be transformed into the orbital frame by $\mathbf{F}^O_\lambda = \mathbf{C}^O_I \mathbf{F}_\lambda$ and the orientation angle of the multipliers resultant Γ_λ respect to $\mathbf{Z}_O$, can be defined as $\Gamma_\lambda = \tan^{-1}\left(F^O_{\lambda_3}/\sqrt{\left(F^O_{\lambda_1}\right)^2 + \left(F^O_{\lambda_2}\right)^2}\right)$.

To conclude, the resulting torque acting on the main spacecraft $\mathbf{M}_\lambda$, and computed from the constraints reactions, can be established as

$$\mathbf{M}_\lambda = \sum_{i=1}^{p} \left(\hat{\mathbf{B}}^p \hat{\mathbf{B}}^e_{i1} - \frac{1}{2}\left(\mathbf{B}^r_1 + \mathbf{B}^r_2\right)\right) \mathbf{q} \times \boldsymbol{\lambda}_i, \tag{78}$$

where the cross product definition considers that the moment is computed at the origin of the body frame O_B.

4. Analysis cases and results

This section describes the analyses performed and presents the corresponding results. Firstly, the baseline configuration considered in the current work is described. Secondly, the convergence analysis results are presented comparing the use of truss and cable elements. Thirdly the influence of the sailing angle is investigated by considering two operating configurations: one, the Sun facing case, in which $\alpha = 0$ deg, and two, a non-null sailing angle scenario given by $\alpha = 10$ deg. For both cases, the results for a single tether and for the E-sail are provided separately.

It should be noted that all the aforementioned analyses disregard the gravitational forces, and consequently the coupling of orbital and attitude effects are neglected in coherence with the low impact for short term dynamics identified in previous contributions [28].

The simulations are implemented in Matlab R2021b and executed on a Microsoft Windows 10 Pro OS, running on a 11th Gen Intel Core i7-11700 @ 2.5 GHz processor.

4.1. Definition of baseline configuration

The E-sail baseline configuration considered for the numerical simulations, as well as the initial values for position, attitude and angular velocity, are established in this section.

The main dimensions and properties of the central spacecraft, tethers and remote units, are given in Table 1 and correspond to the ones considered in [32]. However, it should be noted that the architecture assessed in the present work does not consider secondary tethers in opposition to [32]. The position of the origin of inertial frame O_I, respect to O_H frame is set to $\mathbf{R}_O = \left[\sqrt{2}/2, \sqrt{2}/2, 0.0\right]^T$ AU. Additionally, the location of O_O (corresponding to O_B) coincides with O_I at the initial instant of the simulations. Regarding the initial orientation of the body frame respect to the orbital frame, it is given by the Euler angles: $\psi_0 = 0$ deg, $\theta_0 = \alpha - 90$ deg, and $\phi_0 = 0$ deg. Analogously, the starting E-sail attitude defined by Ψ_0, Θ_0, and Φ_0 angles, is assumed to be equal to the B frame orientation. The angular rate vector is initiated as $\boldsymbol{\omega}^B(0) = \left[4.0 \cdot 10^{-3}, 0.0, 0.0\right]^T$ rad/s, its initial module, referred to as nominal spin, is computed as $\omega_0 = \| \boldsymbol{\omega}(0) \|$ and leads to the definition of the nominal spin period $T_s = 2\pi/\omega_0$. With reference to the initial nodal positions, on one hand, the nodes of the rigid body are defined accordingly to the dimensions specified in Table 1 and the initial Euler angles previously mentioned, being $\mathbf{d}(0)^B = \left[-h_r/2,\ 0,\ 0,\ h_r/2,\ 0,\ 0,\ 0,\ R_r,\ 0,\ 0,\ 0,\ R_r\right]^T$ and $\mathbf{d}(0) = \mathbf{C}_B^I \mathbf{d}(0)^B$. On the other hand, all the tether nodes are contained in the $\mathbf{Y}_B\mathbf{Z}_B$ plane, following their corresponding radial directions. The cable elongation is considered conforming to the analytical steady solution for a rotating cable with a tip mass. Therefore, the centrifugal acceleration caused by $\boldsymbol{\omega}^B(0)$ leads to the initial generalized coordinates for node j of tether i given by the expression

$$\hat{\mathbf{e}}_{ij}^B(0) = \begin{bmatrix} 0 \\ \left(1 + \frac{\rho_t \omega_0^2}{6E_t}\left(3L_0^2 - \hat{r}_{ij}(0)^2\right) + \frac{m_t \omega_0^2 L_0}{E_t A_t}\right)\hat{r}_{ij}(0)\cos(\zeta_i) \\ \left(1 + \frac{\rho_t \omega_0^2}{6E_t}\left(3L_0^2 - \hat{r}_{ij}(0)^2\right) + \frac{m_t \omega_0^2 L_0}{E_t A_t}\right)\hat{r}_{ij}(0)\sin(\zeta_i) \\ 0 \\ \left(1 + \frac{\rho_t \omega_0^2}{2E_t}\left(L_0^2 - \hat{r}_{ij}(0)^2\right) + \frac{m_t \omega_0^2 L_0}{E_t A_t}\right)\cos(\zeta_i) \\ \left(1 + \frac{\rho_t \omega_0^2}{2E_t}\left(L_0^2 - \hat{r}_{ij}(0)^2\right) + \frac{m_t \omega_0^2 L_0}{E_t A_t}\right)\sin(\zeta_i) \end{bmatrix}, \tag{79}$$

where $\hat{r}_{ij}(0)$ corresponds to the distance of the node to the spin axis ($\mathbf{X}_B$), calculated as

$$\hat{r}_{ij}(0) = \| \hat{\mathbf{r}}_{ij}(0) \| = R + \frac{L_0(j-1)}{n-1}, \tag{80}$$

and which can be transformed to the I frame by $\hat{\mathbf{e}}_{ij}(0) = \mathbf{C}_B^I(0)\,\hat{\mathbf{e}}_{ij}^B(0)$. In regard to the initiation of the velocity of the generalized coordinates, the nodal components can be calculated by the cross product of the initial angular rate and the nodal generalized coordinates. The velocities of the rigid body nodes can be written as

$$\dot{\mathbf{d}}(0) = \mathbf{C}_B^I(0)\,\boldsymbol{\omega}^B(0)\,\mathbf{d}(0), \tag{81}$$

Table 1
Description of the main parameters considered for the definition of the E-sail baseline configuration.

Body	Dimension	Value
Main spacecraft	height, h_r [m]	2
	outer radius, R_r [m]	1
	density, ρ_r [kg/m^3]	884
Tethers	number of tethers, n_t[-]	12
	nominal length, L_0 [km]	10
	section area, A_t [mm^2]	$4.28 \cdot 10^{-3}$
	section inertia, I_t [mm^4]	$1.47 \cdot 10^{-6}$
	density, ρ_t [kg/m^3]	7653
	Young modulus, E_t [GPa]	70
	Voltage, V_0 [kV]	20
Remote unit	mass, m_u [kg]	1.5

and in the case of cable elements, the composition of the angular speed with both the positions and gradients generalized coordinates should be vertically concatenated leading to

$$\dot{\hat{\mathbf{e}}}_{ij}(0) = \begin{bmatrix} \mathbf{C}_B^I(0)\,\boldsymbol{\omega}^B(0) \times \hat{\mathbf{B}}^p\,\hat{\mathbf{e}}_{ij}(0) \\ \mathbf{C}_B^I(0)\,\boldsymbol{\omega}^B(0) \times \hat{\mathbf{B}}^s\,\hat{\mathbf{e}}_{ij}(0) \end{bmatrix}. \tag{82}$$

4.2. Convergence analysis and cable/truss comparison

The impact of the number and type of finite elements considered for the modelling of the tethers is analyzed in this section. Moreover, to validate the effect of considering the bending stiffness with respect to tether's modelling approach considering only axial stiffness [28–30, 32], simulation results are provided for both cable FE and truss FE idealizations. For the former type, non linear axial and bending stiffness and internal damping are considered as per the ANCF introduced in Sect. 2.2. For the latter case, the same formulation is implemented but only the axial contribution is considered.

The E-sail configuration and initial states are established following the baseline configuration described in Sect. 4.1, and the value of sailing angle at the initial time $t = 0$, is set to $\alpha_0 = 10$ deg. The resulting DAE systems, considering different number of FEs per tether, are integrated up to $t_f = 3T_s$, and the evolution of the most relevant magnitudes are depicted in Fig. 4. For a straightforward comparison, normalized variables, defined as $\widetilde{y}_n = y_n/y_1$, are established, being y_n the value of magnitude for a given FE type (cable or truss) considering n finite elements per tether, and y_1 is the case in which one cable finite element per tether is used.

In accordance to Figs. 4(a) and (b), representing the error for thrust magnitude $\| \tilde{\mathbf{F}}_c \|$, thrust angle ($\Gamma_c$), respectively, the tether discretization is demonstrated to have a very low impact on the predicted values of the thrust, and the use of just one element per tether is sufficient to estimate the thrust with an error below 1%. This fact can be justified given the reduced values of the tethers oscillation amplitudes, which do not modify notably the orientation of the tether with respect to the solar rays, which drives the generation of the Coulomb forces. In relation to the maximum strain along the tether, $\tilde{\epsilon}_{max}$, presented in Fig. 4(c), a moderate but non-negligible impact of the idealization is observed. This point is linked to the closer dependence of strains to the tether dynamics. In agreement with the previous discussion, the convergence of cable elements is judged to be achieved for five FEs, whereas for truss elements nine elements per tether seem to be necessary.

According to Fig. 4(d), a notably higher computing time is required to consider cable elements instead of truss elements. Nevertheless, the values of normalized computing times associated to the use of idealizations ensuring the convergence are: 5.64 for five cable elements per tether and 2.15 for nine truss elements per tether, and remain comparable. Furthermore, even if the current work is not oriented on the performance for real-time implementation, it can also be appreciated that, only in the case of considering one finite element per tether the computation time of the current Matlab implementation is close to the real-time computing threshold (RTCT).

Moreover, the comparison of the time histories for angular velocities shown in Figs. 5(a1) to (b3) for cable elements and Figs. 5(c1) to (d3) for truss components, allows to conclude that a higher convergence ratio is observed in the case of considering bending stiffness and its associated vibration modes. In the case of ω_1^B, depicted in detail in Fig. 5(b1),

it is observed that for five elements, the inclusion of additional elements does not affect at all the evolution of the magnitude. It should be noted, that the frequency of the oscillations is captured with just three elements per tether. In the case of ω_2^B and ω_3^B, which are several order of magnitudes lower than ω_1^B, 5(b2) and (b3) allow to appreciate that the convergence is achieved for three FEs, and the inclusion of additional elements and modes affects the evolution very locally. A different conclusion is reached from the observation of results for truss elements, illustrated in Figs. 5(c1) to (d3). According to Figs. 5(c1) and (d1), an extremely large impact of the discretization is observed when truss elements are considered. It is remarkable that for a single element per tether model, the spin oscillations are not even captured. For an increasing number of elements, the frequency of the oscillations notably evolves, and convergence is not reached until increasing the number of elements to nine. With regards to the amplitude of the oscillation, a moderate lack of convergence is observed. The same behaviour is observed for the non-principal axes and its associated angular velocities ω_2^B, presented in Figs. 5(c2) and (d2), and ω_3^B, depicted in Figs. 5(c3) and (d3).

For these reasons, it can be determined that cable elements present a notable higher convergence rate and thus are more adequate than truss elements to capture the dynamics of E-sail tethers with a higher accuracy. For the sake of briefness, additional simulation results comparing the tether idealization considering five cable elements and nine truss elements are provided in Figs. 11 and 12 included in Appendix C.

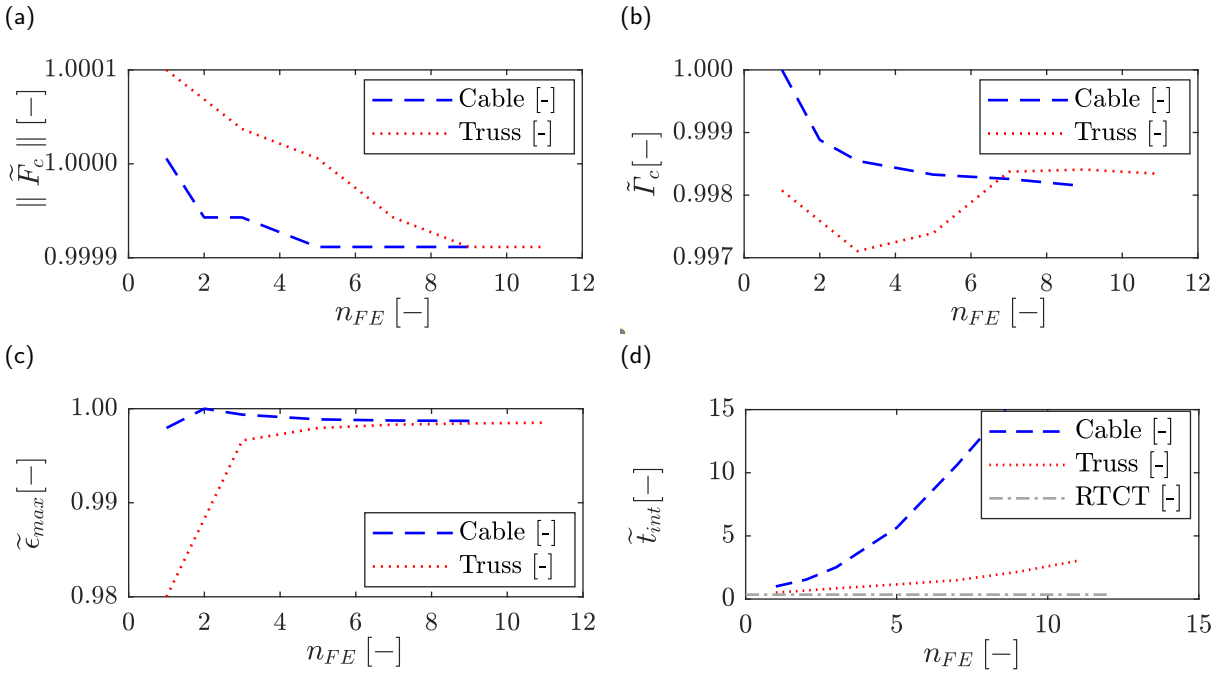

Figure 4: Comparison of the results for the convergence analysis considering the number of elements and the finite element formulation used to idealize the tethers. The E-sail baseline configuration described in Table 1 and a sailing angle $\alpha = 10\,\text{deg}$ are considered. Cable formulation includes axial and bending stiffness while truss approach neglects the bending term. The evolution of the magnitudes, normalized with the results for the case of one cable finite element per tether, are presented: (a) Normalized thrust module, $\| \widetilde{F}_c \|$; (b) Normalized thrust angle, $\widetilde{\Gamma}_c$; (c) Normalized maximum strain at tether 1, $\widetilde{\epsilon}_{max}$; and (d) Normalized integration time, $\widetilde{t}_{int}$. Real-Time Computation Threshold (RTCT) is also displayed for reference.

4.3. Baseline configuration analysis

The current section presents the results for the analyses of an E-sail established following the baseline parameters and initial conditions defined at the Sect. 4.1. The results for the variables of interest in relation to the behaviour of a single tether are presented in Sect. 4.3.1, and the results for the E-sail dynamics are provided in Sect. 4.3.2.

In line with the conclusions achieved in Sect. 4.2, the results correspond to a tethers modelling considering five cable finite elements. Two operating configurations are considered regarding the value of the sailing angle: Sun facing, thus $\alpha = 0$ deg and non-symmetrical operation, given by $\alpha = 10$ deg. Finally, it is remarked that the voltage modulation

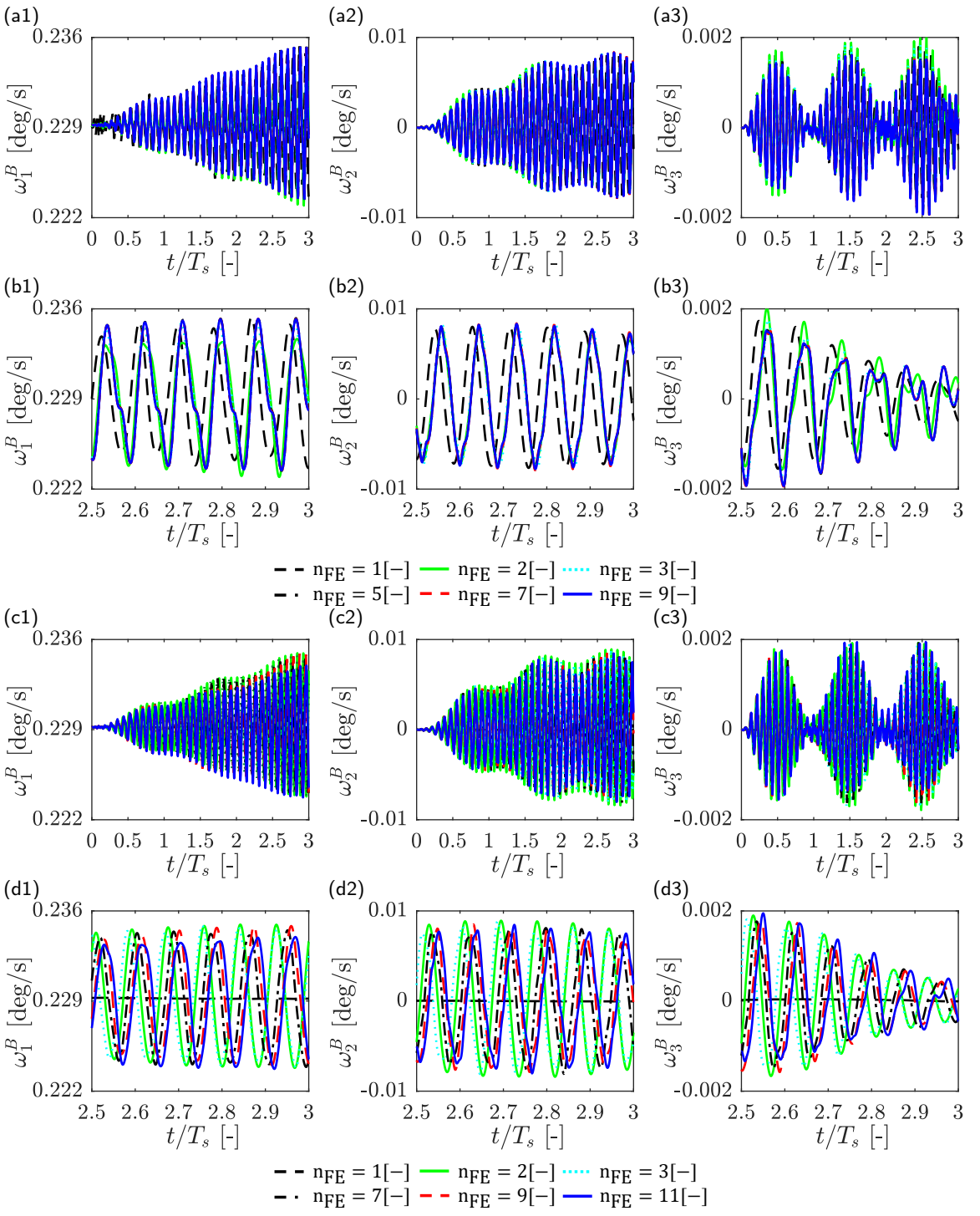

Figure 5: Time histories of absolute angular velocities of the central body obtained for the convergence analysis, which evaluates the effect of the discretization and the element formulation used for tethers modelling. Baseline configuration and $\alpha = 10\,\mathrm{deg}$ are considered. Results for cable element are: (a1) to (a3) expose the evolution along the whole time span $3T_s$; and (b1) to (b3) provide a detailed view for the period $2.5T_s \leq t \leq 3T_s$. The results for truss elements are: (c1) to (c3) display the evolution along the whole time span $3T_s$; and (d1) to (d3) provide a detailed view for the period $2.5T_s \leq t \leq 3T_s$.

Table 2
First natural frequencies for a pinned rotating beam with a tip mass considering the baseline tether's parameters.

Frequencies [Hz]		
Spin	1^{st} Bending	1^{st} Axial
$6.37 \cdot 10^{-4}$	$7.34 \cdot 10^{-3}$	$2.17 \cdot 10^{-2}$

of the tether is constant and equal to 20 kV (Table 1) for all the analyses, with exception to the null voltage case provided in Sect. 4.3.2, which validates that no energy drift is taking place with the selected integration approach.

In order to better understand the active and dominant dynamic modes, not only time histories are systematically presented, but also the Power Spectral Density (PSD) distributions are provided when considered valuable. For PSD charts, the three main analytical frequencies, corresponding to: rigid, bending and longitudinal modes, are also represented by vertical dashed lines. These modal frequencies, are computed for a pinned rotating beam with a tip mass according to [78], and their values, considering the E-sail baseline configuration, are provided in Table 2.

Finally, apart from the figures and graphics provided in next sections, the animation sequence for the baseline configuration operating with a reduced sailing angle ($\alpha = 0.01$ deg) is provided in Appendix D as a supplementary file, allowing to appreciate in a more explicit manner the harmonious dynamics of the system.

4.3.1. Single tether results

This section contains the results associated with the tether 1 of the baseline E-sail. The time histories and PSD of the magnitudes defining the tether motion are provided, namely: the coning and lagging angles establishing the evolution of the remote unit, and the root coning and lagging angles, describing the orientation of the tether's slope at the root. The simulation results are compared and validated against the analytical solution for a rotating rigid cable with a tip mass. In addition, the time evolution of the resultant of the Coulomb force distribution along the tether is presented and compared to the reactions at the tether root defined by the evolution of Lagrange multipliers.

Simulation results are depicted in Fig. 6 for the following magnitudes associated with tether 1: coning angle γ_1 and lagging angle β_1 at the tip, coning angle γ_1', and lagging angles β_1' at the root, and normalized tether's length L/L_0. Both the power spectral density distributions and the time histories are furnished. The time normalized with reference to the spin period T_s is considered for a better identification of periodic behaviours. For the sake of readability, the sub-index indicating that the magnitudes correspond to tether 1 is omitted, but it should be remarked that all the results in this Section correspond to single tether results.

The time evolution of the angle γ, is depicted in Fig. 6(a1), allowing to clearly identify the separation and approach phases, occurring at the first and second half of the spin period T_s, respectively. Moreover it is observed that the overall evolution of γ is ruled by the period T_s associated to the spin rate, as confirmed by Fig. 6(a2). This behaviour is in accordance with the results and the description of the coning motion presented in [25, 30, 34]. It is notable that, even if the E-sail baseline parameters selected, shown in Table 1, correspond to the configuration analyzed in [32], there exists a non-negligible difference in the maximum value of coning angle predicted in [32] and in the current work. This fact is in coherence with the presence of the auxiliary tethers in the configuration studied in [32], which reduce the amplitude of the coning oscillation. For the current configuration, described in Fig. 3, in which only the main tether exist, under the assumption of rigid tether and assuming small angle γ, the dynamic equation describing the coning angle motion [79], can be simplified to:

$$\ddot{\gamma} + \gamma \left(\omega_1^B\right)^2 (1+\varepsilon) = \frac{-M^B_{c1_3}}{(m_u + 1/3m_t)L_0^2}, \tag{83}$$

where m_u is the mass of the remote unit, m_t represents the mass of the tether and L_0 is the nominal tether length. Additionally $M^B_{c1_3}$ is the z component of the moment associated to the Coulomb forces respect to the anchor point, computed for the tether 1 and expressed in the body frame, which is depicted in Fig. 7(b3) and is subsequently described in detail. Moreover, the term ε represents the contribution of the centrifugal restoring moment, and is given by

$$\varepsilon = \frac{3R_r}{2L_0}\frac{2m_u + m_t}{3m_u + m_t}, \tag{84}$$

where R_r is the radius of the main vehicle. The analysis of the order of magnitudes of the terms in Eq. (83), shows that the term associated to γ has an order of magnitude $\mathcal{O}\left(\gamma\left(\omega_1^B\right)^2(1+\varepsilon)\right) = 10^{-8}$, while $\mathcal{O}\left(M^B_{c1_3}/\left(m_u + 1/3m_t\right)L_0^2\right) = 10^{-4}$, being this last dominant. Given the structure of Eq. (83) and the evolution of the Coulomb moment described in Fig. 7(b3), γ oscillates with the spin frequency, being the amplitude modulated by the Coulomb moment applied, which remains notably stable. The reduced impact of sailing angle on $M^B_{c1_3}$ explains the slight alteration observed also for γ. This effects are confirmed by the representation of the solution of Eq. (83) in Fig. 6(a1) for both the Sun facing (label "Rigid $\alpha = 0$") and non-symmetrical operation (label "Rigid $\alpha = 10$").

On the contrary to the coning motion, which is well known and understood thanks to previous contributions on the matter [25, 30], the motion of tether within plane $Y_B Z_B$ has not been studied nor explained for E-sails, even when an extensive literature exists in other rotating applications, namely, helicopter rotors [80]. Consequently, it is necessary to investigate the in-plane dynamics of E-sail's tethers under the effect on non-symmetrical Coulomb forces. This effort is particularly interesting for the current configuration in which the secondary tethers are omitted. The evolution of β is represented in Fig. 6(b1), where it can be observed that, for the case of null sailing angle, the motion is driven by a single high frequency oscillation presenting an increasing amplitude. Moreover, under this operation condition, the mean value of the lagging angle β is initially null, although, a moderate growing tendency is recognized. On the contrary, in the case of non-null sailing angle, the behaviour is notably modified and a superposition of two oscillation of different frequencies is observed. The representation of the corresponding power spectral density depicted in Fig. 6(b2), allows to identify, firstly, a frequency around $6 \cdot 10^{-2}$ Hz associated to the bending mode and acting with a similar amplitude for both Sun facing and non-symmetrical operating conditions. Secondly, and exclusively in the case of non-null sailing angle, it can be observed that the spin frequency $1/T_s = 6.37 \cdot 10^{-3}$ Hz, associated to the rigid body mode, is activated. Both behaviours, can be explained by the Euler dynamic equations for tether lagging in terms of the angle β, under the hypothesis of small angles and rigid cable adapted from [79]

$$\ddot{\beta} + \beta\left(\omega_1^B\right)^2\varepsilon = -\frac{-M^B_{c1_1}}{(m_u + 1/3m_t)L_0^2} + \omega_1^B\gamma\dot{\gamma}, \tag{85}$$

where $M^B_{c1_1}$ is the x component of the moment associated to Coulomb forces respect to the tether root for tether 1 expressed in body frame and represented in Fig. 7(b1). The term $\beta\left(\omega_1^B\right)^2\varepsilon$ represents the restoring force associated to centrifugal forces and $\omega_1^B\gamma\dot{\gamma}$ is the coupling with the out of plane motion. For the current E-sail description and under the baseline analysis configuration, it can be proven that $\mathcal{O}\left(\beta\left(\omega_1^B\right)^2\varepsilon\right) = 10^{-12}$ and $\mathcal{O}\left(\omega_1^B\gamma\dot{\gamma}\right) = 10^{-8}$. In the case of symmetric operation ($\alpha = 0$), the moment associated to Coulomb forces is negligible and the term associated to $\dot{\gamma}$ is dominant and responsible for the moderate increase of the mean value observed. It should be noted that the higher frequency oscillations are associated to the bending flexibility of the tether and are not captured under the rigid pendulum approach, also represented in Fig. 6 (b1). For non-null sailing angle scenario, the order of magnitude of the term affected by $M^B_{c1_1}$ grows, being $\mathcal{O}\left(M^B_{c1_1}/\left(m_r + 1/3m_t\right)L_0^2\right) = 10^{-8}$ for α=10 degrees, and adds an oscillation of the frequency of the main spin. The power spectral density for β in Fig. 6(b2), evidence the participation of the bending modes. This last consideration proves the inadequate performance of the rigid pendulum model for a precise analysis of the in-plane motion in the scenarios where the transversal effects need to be contemplated.

The representation of tether length results, provided in Figs. 6(c1) and (c2), completes the description of the relative motion of the remote unit for tether 1. Both, the time evolution in Fig. 6(c1) and power spectral density distribution in Fig. 6(c2), allows to observe the participation of a more diverse set of frequencies than in the case of the angles γ and β. Moreover, Fig. 6(c2) allows to notice that the dominant frequency is positioned between the frequencies associated to the analytical pure bending and the pure longitudinal modes for a pinned rotating slender beam with a tip mass, presented in Table. 2. The reduced oscillation on the normalized length, allows to conclude that it is driven by the centrifugal forces, which remain remarkably steady according to the angular velocity evolution, in Fig. 10(a1), subsequently described in detail. Consequently, the tensile load in the cable is also expected to remain constant.

Furthermore, given that the direction of the reactions exerted on the central spacecraft at the anchor point depend on the orientation of the longitudinal slope of the tether at the root, the analysis of the root coning angle, γ', and the root lagging angle, β', is of interest to understand the associated perturbation torques. The time evolution of the orientation

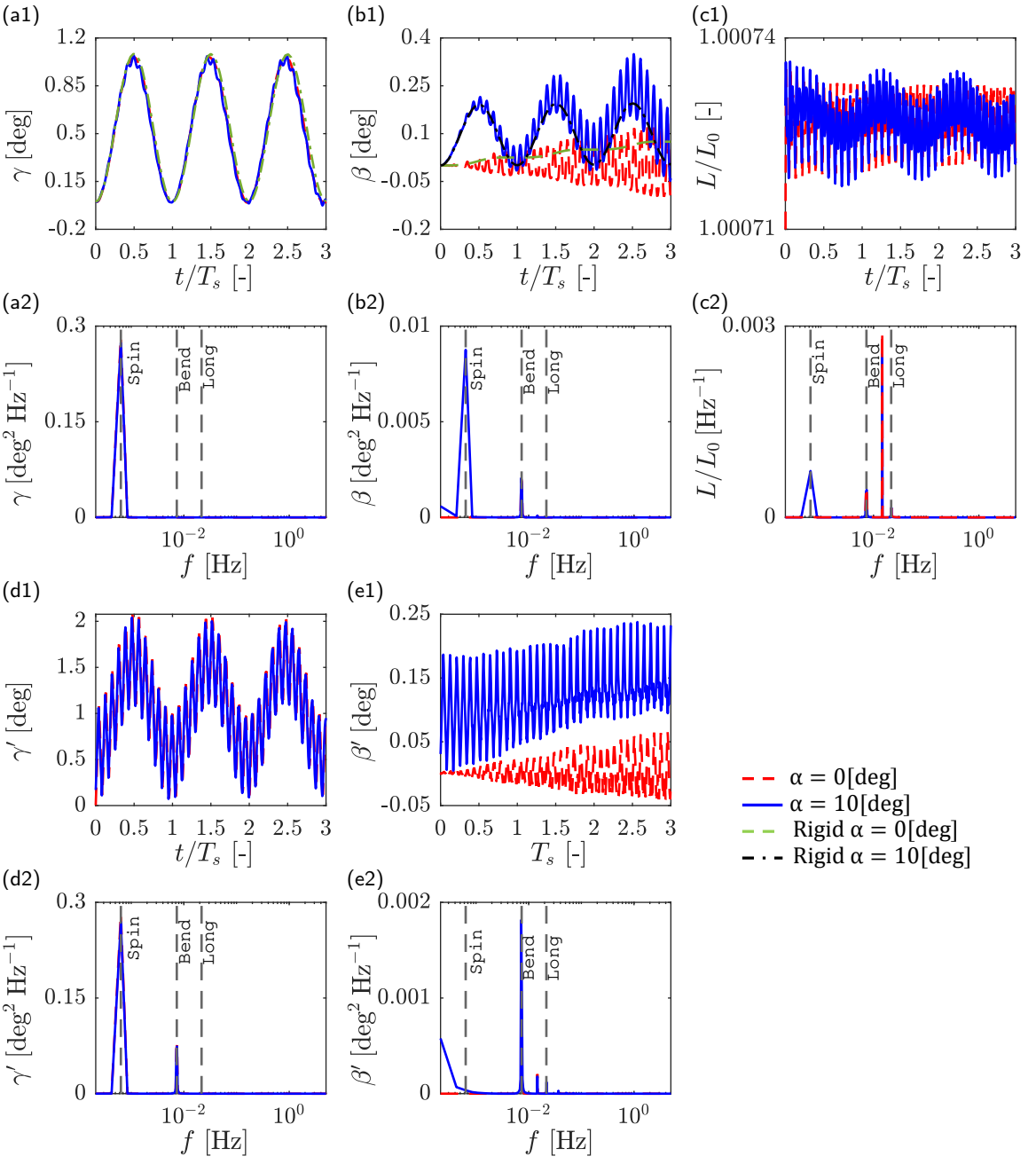

Figure 6: Description of the relative motion of tether 1 under different sailing angles ($\alpha = 0, 10\,\mathrm{deg}$) and comparison to analytical solution under the assumption of rigid rotating pendulum. All the results correspond to the E-sail baseline configuration described in Table 1: (a1) Time evolution of the coning angle, γ, and the solution of Eq.(83), valid for a rigid cable; (a2) PSD of the coning angle γ; (b1) Time evolution of the lagging angle, β, and the solution of Eq.(85), valid for a rigid cable; (b2) PSD of the lagging angle, β; (c1) Time evolution of normalized length, L/L_0; (c2) PSD of normalized length, L/L_0; (d1) Time evolution of the root coning angle, γ'; (d2) PSD of the root coning angle, γ'; (e1) Time evolution of the root lagging angle, β'; and (e2) PSD of the root lagging angle, β'.

of the longitudinal slope of the tether at the root is defined by the root coning angle, γ', and the root lagging angle, β', and presented in Figs. 6 (d1) and (e1), respectively. The PSDs associated to the previous variables are also provided at Figs. 6 (d2) and (e2).

The comparison of the power spectral density representations in Figs. 6(d2) and (e2), allows to identify the active modes for each magnitude and unveils a more complex dynamics of the internal angles γ' and β' in comparison to the evolution of the analogous magnitudes at the tip (Fig. 6(a2) for γ and Fig. 6(b2) for β). In reference to γ', Fig. 6(d1) allows to verify its independence respect to the sailing angle α, previously observed and explained for γ. Furthermore, the activation of the flexural mode in addition to the dominant rigid mode associated to the spin frequency is clearly observed at both Figs. 6(d1) and (d2). Concerning the in-plane orientation of the slope given by β', Fig. 6(e1) reveals a remarkable influence of the sailing angle on its dynamics, similarly to the results for β. However, the effects of the sailing angle on the participating frequencies observed for β', are notably different from those previously described for β, being remarkable: the lack of contribution of the rigid mode, the offset of the active modes to higher frequencies and the appearance of a low frequency oscillation.

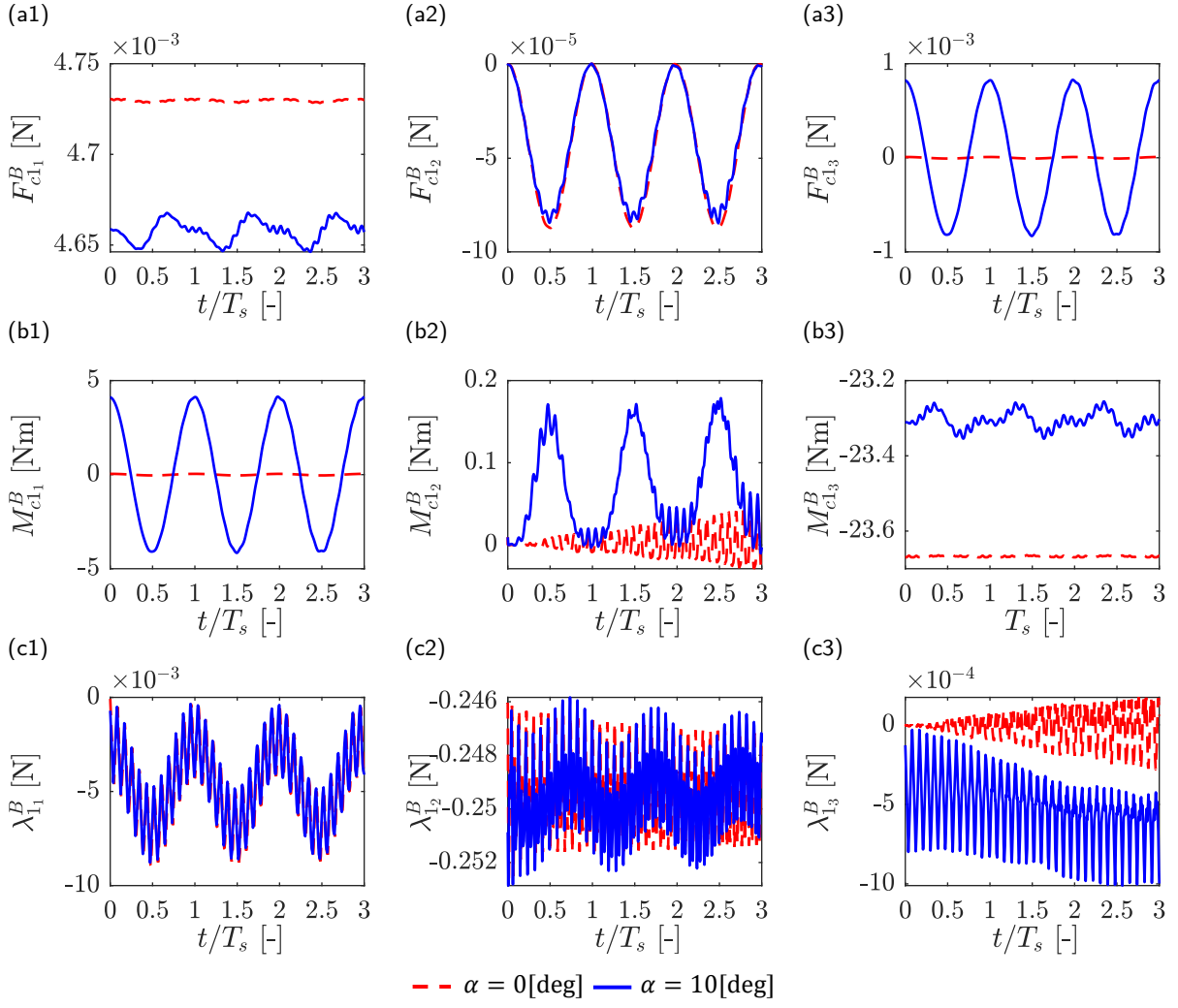

Figure 7: Time histories of simulation results for tether 1 forces and moments, expressed in body frame, considering the baseline configuration and under Sun facing ($\alpha = 0$ deg), and non-symmetrical ($\alpha = 10$ deg) operating conditions: (a1) to (a3) Resultant force components of the Coulomb force distribution along the tether $\mathbf{F}^{B}_{c1}$; (b1) to (b3) Moment components of Coulomb force distribution along the tether, computed at the root $\mathbf{M}^{B}_{c1}$; and (c1) to (c3) Lagrange multipliers at the tether root $\boldsymbol{\lambda}^{B}_{1}$.

To complete the study of the dynamics of an E-sail's tether, the propulsive force resultant $\mathbf{F}^{B}_{c1}$, and its associated torque respect to the anchor point $\mathbf{M}^{B}_{c1}$, are presented and analyzed for tether 1. As it can be observed in Fig. 7(a1),

the resultant of the Coulomb force distribution along X_B, namely $F^B_{c1_1}$, presents an average value clearly affected by the sailing angle α. Negligible oscillations associated to the coning motion can be spotted for $\alpha = 0$ deg, being more accentuated in the case of $\alpha = 10$ deg, due to the additional fluctuations on the angle between the solar wind and the tethers occurring during a spin period. The contribution along Y_B, depicted in Fig. 7(a2), is insignificant, given that for tether 1, the Y_B axis corresponds to the tether radial direction. The propulsive force along it is due exclusively to the bending deformation during the coning motion. Concerning the $F^B_{c1_3}$ component, it presents a clear dependence on sailing angle, as illustrated in Fig. 7(a3), and evolves cyclically following the fluctuation of the tether-Sun wind angle previously mentioned. Similarly, the torque at the anchor point $\mathbf{M}^B_{c1}$, associated to the distribution of the Coulomb force along the tether, is represented in Figs. 7(b1) to (b3). The time histories for each component are coherent to the force evolution previously discussed, besides, their order of magnitude is to be considered to asses the dominant terms on Eq. (83) and (85).

Finally, Figs. 7 (c1) to (c3), present the evolution of the Lagrange multipliers $\boldsymbol{\lambda}^B_1$, corresponding to the reaction at the anchor point of tether 1 expressed on the B frame. The comparison of the results for the Coulomb forces, presented in Figs. 7(a1) to (a3), and for the multipliers, shown in Figs. 7(c1) to (c3), allows to observe how the tether dynamics transforms the smooth propulsive force extracted from the solar wind, into a much more faster and complex load distribution applied to the central vehicle. The existing correlation between $\boldsymbol{\lambda}^B_1$ x and z components, presented in Figs. 7(c1) and (c3), and the tether slope angles γ' and β', represented in Figs. 6(d1) and (e1), respectively, demonstrate the necessity of capturing the motion at the tether root to estimate the dynamics of the forces applied to the main vehicle.

4.3.2. E-sail motion and attitude

This section provides the results for the E-sail dynamics. The evolution and composition of the system energy is presented and assessed. Given that the considered generalized-α algorithm is not a symplectic integrator, in order to demonstrate the nonexistence of energy drift, the evolution of the E-sail energy considering null voltage at the tethers is also provided. In addition, the total thrust force extracted from the solar wind is examined, and its transfer to the central vehicle is investigated. To conclude, the attitude and angular rates of the E-sail and the central vehicle are presented and explained.

The evolution of the system total energy E_T is presented in Fig. 8(a). On the one hand, for the null voltage case (E-sail off) the constant value of the total energy allows to conclude the negligible loss of energy associated with the numerical damping of the generalized-alpha implementation or its non-symplectic condition. On the other hand, the sustained thrusting of the system under the operating conditions $\alpha = 0, 10$ deg, is reflected on the increase of E_T depicted in Fig. 8(a). Additionally, the presence of the spin and the first bending frequencies can be clearly appreciated in the evolution of the magnitude. This behaviour can be explained, considering that according to Fig. 8(b) the kinetic energy is the main contribution to the total energy, and it is determined by the variation of the kinetic energy associated to the remote masses and central vehicle which is driven mainly by both modes. A slight influence of sailing angle can be observed for the approximation phase (second half of the cycle) in which the Sun facing configuration reveals to be more efficient. The energy accumulated by the E-sail under elastic deformations, provided in Fig. 8(c), is observed to remain independent of the sailing angle and to oscillate around an stable value. Moreover, the frequency of the oscillations reveals that the main contribution to the elastic energy fluctuation is associated to the longitudinal deformation. To conclude the discussion of the energy system, the analysis of the dissipated energy associated to internal damping, plotted in Fig. 8(d), reveals a marginal contribution, presenting a decreasing trend with time. It should be remarked that E_d is calculated as the time-averaged dissipated power.

Concerning the evolution of the forces acting on the E-sail, the evolution of the norm of the Coulomb force $\| \mathbf{F}_c \|$, also referred to as thrust force, is represented in Fig. 9(a1), the norm of the moment associated to the thrust $\| \mathbf{M}_c \|$, can be observed in Fig. 9(a2), and the thrust angle Γ_c, formed by the thrust resultant and the Sun rays (coincident with the Z_O axis) is provided in Fig. 9(a3). The effect of the sailing angle can be appreciated in the average value of the thrust module, $\| \mathbf{F}_c \|$, and the thrust angle, Γ_c, which remain almost constant along the period studied. A greater sailing angle implies a reduction of the perpendicular component of the relative velocity of the solar wind, and also the apparition of an in-plane thrust contribution. Consequently, the norm of the thrust decreases with α, whereas the thrust angle grows up to approximately $\alpha/2$, being both effect in line with results provided in [28, 32]. Additionally, a reduced oscillation of the amplitude is observed in the thrust norm, which is explained by the evolution of the coning angle γ presented in Fig. 6(a1), thus the minimum is reached at the half of the spin period where the coning angle is maximum and the overall perpendicular component of the relative velocity of the solar wind is minimum. On the

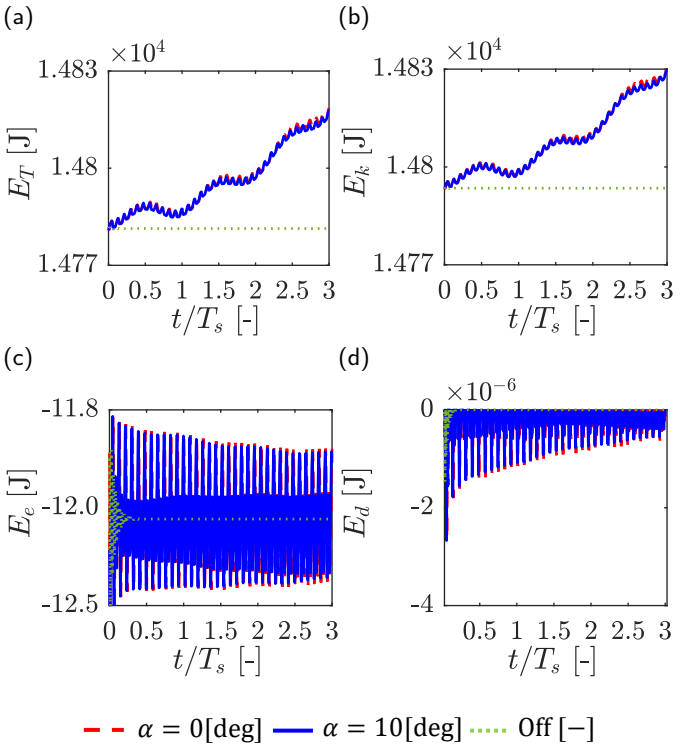

Figure 8: Comparison of E-sail simulation results for energy evolution of baseline configuration under symmetrical ($\alpha = 0$ deg) and non-symmetrical ($\alpha = 10$ deg) operation: (a) Total energy E_T; (b) Kinetic energy E_k; (c) Elastic energy E_e and (d) Damping energy E_d, computed as the time-averaged dissipated power.

contrary, the norm of the thrust moment $\| \mathbf{M}_c \|$ for the $\alpha = 10$ deg case, oscillates following the spin frequency but shows a clear growing tendency.

The equivalent magnitudes for the Lagrange multipliers, are represented in Figs. 9(b1) to (b3) with the aim of outlining the forces and moments applied to the main vehicle. In line with the results presented in Fig. 6 for the slope of the tethers at the root, a faster dynamics is observed. It is remarked that the lower limit of the force module $\| \mathbf{F}_\lambda \|$, depicted in 9(b1), increases with the time for the non-null sailing angle case, which indicates that the mean multipliers force per cycle increases. This effect can be explained based on the detailed component representation for Coulomb and constraint forces provided in Figs. 9(c1) to (d3), expressed in orbit frame for a better understanding. The axial force $\mathbf{F}^O_{\lambda_z}$, Fig. 9(d3), is transmitted along Z_O with a continuous negative sign, which means positive force applied to the central vehicle, according to the coning motion mechanism previously mentioned. The impact of the tether dynamics is clearly revealed by the comparison of the low oscillation of the axial thrust, Fig. 9(c3), and the evolution of axial force applied to the central spacecraft, Fig. 9(d3). At each instant, the difference between the $\mathbf{F}^O_{\lambda_z}$ and $\mathbf{F}^O_{c_z}$ represents the resultant of the Coulomb, inertial, elastic and damping forces acting along the tether and the remote units. It can be observed that the value of the thrust, given by $\mathbf{F}^O_{c_z}$ in the case of sun facing configuration, agrees with the predictions in [32]. In the case of the transversal component $\mathbf{F}^O_{\lambda_x}$, displayed in Fig. 9(d1), a complex and unstable behaviour is observed for non-null sailing angle. It can be verified that its resultant per cycle is negative, hence a positive force along X_O axis is applied to the main spacecraft, in line with the corresponding component of Coulomb force, presented in 9(c1). However, the oscillations of $\mathbf{F}^O_{\lambda_x}$, in contrast to the smooth character of the thrust component $\mathbf{F}^O_{c_x}$, force the existence of a negative torque along Y_O axis acting of the center of gravity of the system and that generates a negative yawing, represented in Fig. 10(b1), that takes the angular momentum out of the orbital plane. To end this discussion, the multipliers component $\mathbf{F}^O_{\lambda_y}$, as observed in Fig.9(d2), for the case of non-null sailing angle, also follows an oscillation of increasing amplitude but resulting on a very low net resultant per cycle, in line with the results for $\mathbf{F}^O_{c_y}$, represented

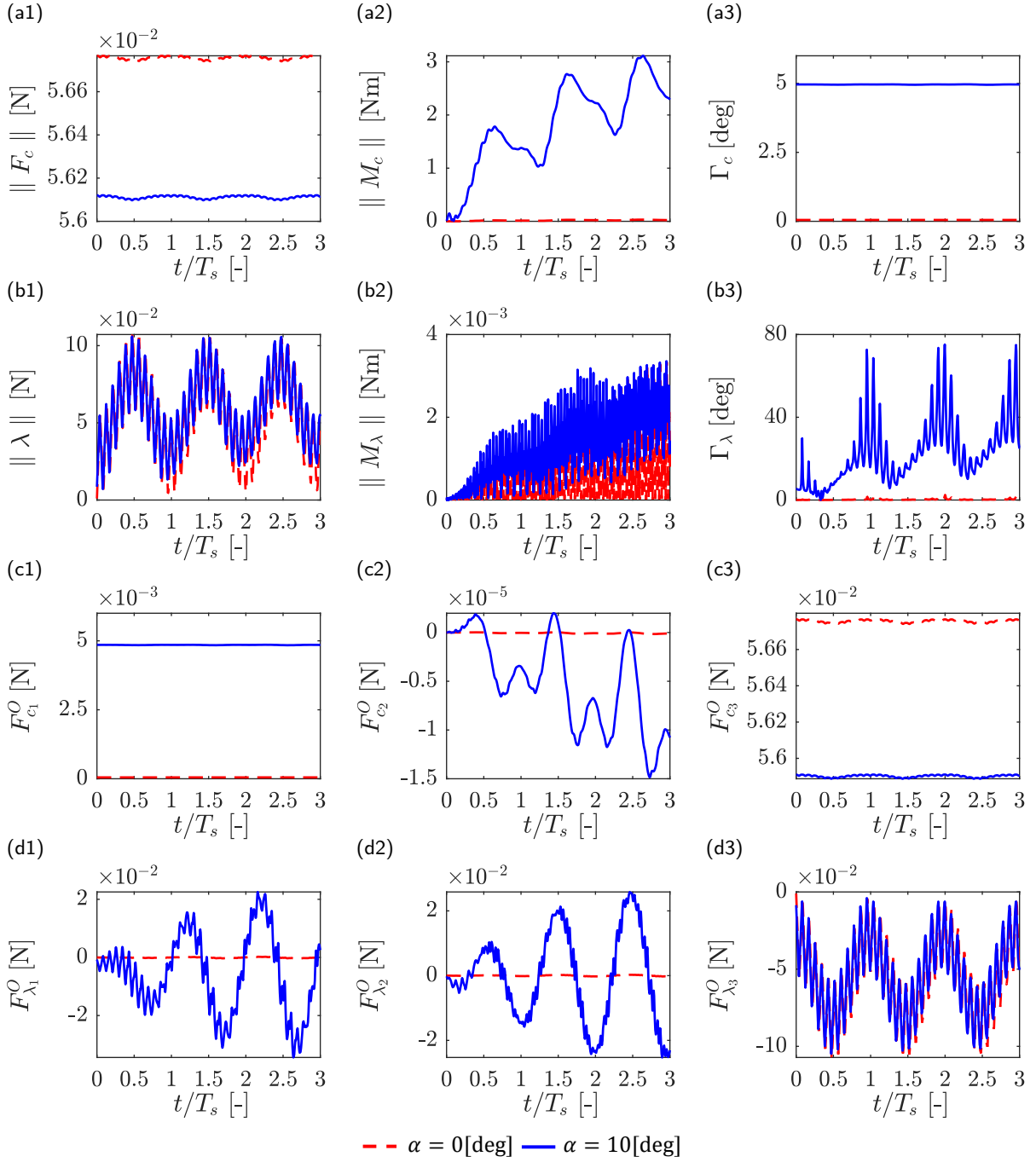

Figure 9: Comparison of simulation results for E-sail's thrust force and Lagrange multipliers, considering the baseline configuration, under symmetrical (α = 0 deg) and non-symmetrical (α = 10 deg) operation: (a1) Thrust force module, $\| \mathbf{F}_c \|$; (a2) Thrust moment module, $\| \mathbf{M}_c \|$; (a3) Thrust angle, Γ_c; (b1) Total Lagrange multiplier force module, $\| \mathbf{F}_\lambda \|$; (b2) Total Lagrange multiplier moment module, $\| \mathbf{M}_\lambda \|$; (b3) Total Lagrange multiplier orientation angle, Γ_λ; (c1) to (c3) Thrust force in orbit frame; and (d1) to (d3) Total Lagrange multiplier in orbit frame.

in 9(c2), and where the effect of the out of plane yaw is reflected on the increase of the magnitude of Coulomb force along Y_O.

In reference to the evolution of the perturbation torque transmitted to the central body and defined by $\| \mathbf{M}_c \|$, Fig. 9(b2) allows to observe a sustained rise. According to the evolution of the angular rates provided in Figs. 10 (a1) to (a3), for null sailing angle, the origin of the norm growth is due exclusively to the spin, while in the case of non-null sailing angle the three component contribute. This behaviour may indicate the instability of the system or the presence of a low frequency mode, and has to be investigated in further works.

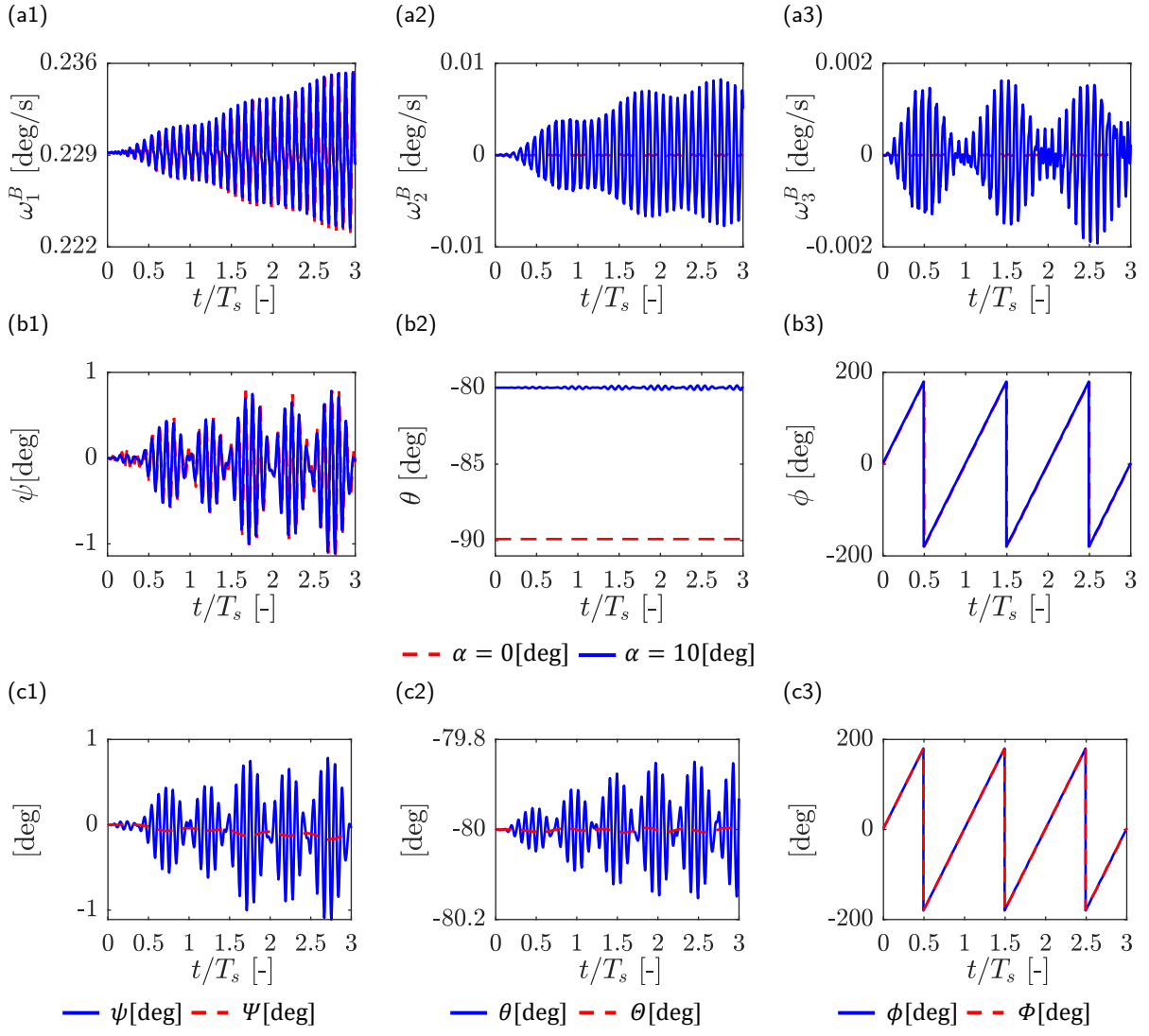

Figure 10: Simulation results for angular rates and orientation for baseline configuration: (a1) to (a3) Comparison of central vehicle absolute angular rates $\boldsymbol{\omega}^B$ considering Sun facing (α=0 deg) and non-symmetrical (α=10 deg) operation; (b1) to (b3) Comparison of central vehicle Euler angles ψ, θ and ϕ considering Sun facing (α=0 deg) and non-symmetrical (α=10 deg) operation; and (c1) to (c3) Comparison of the attitude of the central vehicle given by the B frame (ψ, θ, ϕ), and the attitude of the mean plane of the remote units (Π plane), given by the E frame (Ψ, Θ, Φ), for non-symmetrical (α=10 deg) operation.

To conclude the presentation of results, the absolute body angular rates $\boldsymbol{\omega}^B$, and Euler angles defining the orientation of the main vehicle (ψ, θ, ϕ), and of the E-sail (Ψ, Θ, Φ), are represented for different sailing angles in Fig. 10. In relation to the angular rates, the presence of high frequency oscillations, associated to the bending and the axial modes, can be corroborated accordingly to the behaviours already mentioned for the driving magnitudes, namely, the tether length and the slope at the tether's root. The spin velocity, depicted in Fig.10(a1), describes an oscillation of

increasing amplitude but presents a steady mean value. A very reduced impact of the sailing angle is revealed for the spin oscillation. However, the other two components are notable impacted, as seen in Figs.10(a2) and (a3). For non-null sailing angles, the sustained rise of the oscillations amplitude can be observed for the three components in Figs. 10(a1) to (a3), being more accentuated for ω_1. This evolution is in line with the increase of the perturbation torque associated to the Lagrangian forces depicted in Fig. 9(b2), and may indicate the instability of the system but could also be due to lower frequency modes, not captured for the considered simulation time. This fact needs to be assessed in subsequent work. The sailing angle growth generates the apparition of an increasing oscillation of components ω_2 and ω_3, plotted in Figs. 10(a2) and (a3), respectively. However, Fig. 10(a1) reveals a very reduced effect of sailing angle on the first component ω_1, where only a slight spin acceleration is appreciated and should be further investigated.

Regarding the orientation of the central vehicle, a reduced influence of the sailing angle is confirmed according to the evolution of yaw (ψ), pitch (θ) and roll (ϕ) angles, provided in Figs. 10(b1) to (b3). Apart from the offset of the mean value of θ, a slight increase of the oscillations can be observed for the pitch angle θ for the case of non null sailing angle. To complete the assessment of the system attitude, Figs. 10(c1) to (c3), compares the orientation of the central vehicle and the orientation of the E-sail, being the latest established as per Sect. 3.4. It is noted that the attitude dynamics of Π plane, in contrast to the main vehicle's, is slower, which is in line with the results discussed in previous paragraphs and can be observed at the evolution of ψ and Ψ depicted in Fig. 10(c1) and analogously in Fig. 10(c2) for θ and Θ. It is remarkable the evolution of the yaw angle Ψ, revealing a tendency of the normal vector of the Π planes to move out of the orbital plane when operating with a positive sailing angle. As previously exposed, it is justified by the torque associated to the transference of the X_O component of the Coulomb force to the main vehicle and to the tethers and remote masses.

5. Conclusions

This section contains the conclusions extracted from the results of Sect. 4 and outlines future lines of investigation.

A rigid-flexible multibody model for the E-sail dynamics has been presented and validated. The formulation, considering ACNF for flexible tethers and NC for the center body, is clearly established and described. The expressions of the Jacobian matrices and additional terms, necessary to perform the integration considering the generalized-α algorithm, are provided. In relation to the proposed cable ANCF, the inclusion of internal damping as well as the nonlinear curvature for bending, allows to achieve a better description of the tethers' dynamics and the comparison against formulations considering only axial stiffness. Additionally, a set of auxiliary variables are introduced for a better understanding of the simulation results. The simulation results obtained for the baseline configuration established, allow to settle the following conclusions.

The validity of the proposed model is demonstrated. The evolution of the obtained magnitudes, notably the coning motion mechanism and the thrust force, are in coherence with the results in previous publications. Moreover, the coning and lagging motion of the remote units is validated using analytical formulations.

The accuracy of the generalized-α implementation used to solve the index-3 DAE system is established and the lack of energy drifts associated to numerical damping or other aspect is demonstrated.

The convenience of using cable elements, considering bending stiffness, to accurately capture the dynamic behaviour of the tethers under the effect of the Coulomb forces, is proven. The effectiveness and efficiency of using the existing cable ANCF elements is corroborated. The convergence analysis of truss formulations confirms its high dependency on the discretization and a lower rate of convergence respect to cable elements.

Moreover, thanks to the use of cable elements, the root coning angle γ' and the root lagging angle β' are investigated, and a more complex and faster dynamics is observed in comparison to the magnitudes associated with the remote masses (γ and β). It should be remarked that the time histories of the lagging angles, β and β', manifest a growing tendency, notably dependant of the sailing angle, which needs to be further investigated. Consequently, the interest of analysing the evolution of the in-plane angular magnitudes is demonstrated.

The vibration modes with a more relevant participation on the E-sail dynamics are established; the rigid body mode, associated to the spin frequency and already observed in previous works, and the first bending and axial vibration modes of a rotating cable with a tip mass. This identification is significant for the design of E-sails with appropriate dynamical characteristics.

It is remarkable that for non-null sailing angles, the existence of a torque in the Y_O axis has been found. Results prove that it is associated to the way in which the system dynamics transmits the transverse component of the thrust force to

the main vehicle. As a consequence, an out of plane yawing occurs as well as an increase of the thrust component on the Y_O direction and moves the angular momentum out of the orbital plane.

Further investigations have to be carried out in order to explore the sensitivity of the behaviour exposed to the main parameters of the system, namely, angular velocity, tether length and remote unit mass. Moreover, the effectiveness of auxiliary tethers to prevent tether collision need to be assessed considering cable elements. Additionally, a deeper analysis of the stability and controllability of the system is required to enable the development and application of control strategies. Last but not least, the multi-physics capabilities of the model have to be improved. Namely, the inclusion of thermal aspects is crucial to consider the effect of extreme temperatures or its fluctuations under events such as eclipses and to assess their impact on the dynamics and stability of the system.

A. Cable element formulation

A.1. Elastic contributions

The expressions of the elastic energy, the generalized elastic forces and their Jacobian matrices are derived in detail in this appendix.

In order to achieve an implementation with the best computing performance, the use of invariant matrices is applied when possible to avoid the computation of integrals for each element in every step. In the practice, the use of invariant terms is applicable just for axial contributions but not for nonlinear bending members. In this latter case, the objective is to reach expressions of the integrals in terms of the generalized coordinates (varying with time) and the shape function matrices (just depending on the position and which are evaluated just once for each element) to alleviate the computation effort of the necessary numerical integration for each element at every step. According to the formulation presented in Sect. 2.2.2, the contributions of axial and bending deformation are provided separately.

Axial contribution

Under the assumption of constant properties, the axial contribution of the generalized elastic force defined in Eq. (25) is expressed as

$$\mathbf{Q}_{e_x} = -\frac{E_t A_t}{2}\left(\int_0^l \frac{\partial \epsilon_{xx}^2}{\partial \mathbf{e}}\,\mathrm{d}x\right)^T = -E_t A_t \int_0^l \epsilon_{xx}\left(\frac{\partial \epsilon_{xx}}{\partial \mathbf{e}}\right)^T \mathrm{d}x. \tag{86}$$

Considering the expression of the first partial derivatives of the position with respect to x is given by

$$\mathbf{r}_{,x} = \frac{\partial \mathbf{S}}{\partial x}\,\mathbf{e} = \mathbf{S}_{,x}\,\mathbf{e}, \tag{87}$$

and that the partial derivative of the axial strain ϵ_{xx}, defined in Eq. (24), with respect to the generalized coordinates is given by

$$\frac{\partial \epsilon_{xx}}{\partial \mathbf{e}} = \mathbf{e}^T \mathbf{S}_{,x}^T \mathbf{S}_{,x}, \tag{88}$$

and the expression of the axial elastic force provided in Eq. (86) becomes

$$\begin{aligned}\mathbf{Q}_{e_x} &= -\frac{E_t A_t}{2}\int_0^l \left(\mathbf{e}^T \mathbf{S}_{,x}^T \mathbf{S}_{,x}\mathbf{e} - 1\right)\left(\mathbf{e}^T \mathbf{S}_{,x}^T \mathbf{S}_{,x}\right)^T \mathrm{d}x \\ &= -\frac{E_t A_t}{2}\int_0^l \mathbf{S}_{,x}^T \mathbf{S}_{,x}\mathbf{e}\,\mathbf{e}^T \mathbf{S}_{,x}^T \mathbf{S}_{,x}\mathbf{e}\;\mathrm{d}x + \frac{E_t A_t}{2}\int_0^l \mathbf{S}_{,x}^T \mathbf{S}_{,x}\mathbf{e}\;\mathrm{d}x.\end{aligned} \tag{89}$$

Eq. (89) can be further simplified making use of the invariant matrices proposed in [81] and applied to cable elements in [34] as follows. Define the square matrix $\mathbf{A} = \mathbf{S}_{,x}^T \mathbf{S}_{,x}$, where $\mathbf{A}_{ij}$ represents the element i and j of the matrix

$$\mathbf{Q}_{e_x} = -\mathbf{K}_{1_{ijkn}}\mathbf{e}_j \mathbf{e}_k \mathbf{e}_n + \mathbf{K}_{2_{in}}\mathbf{e}_n, \tag{90}$$

where the following definitions are used:

$$\mathbf{K}_{1_{ijkn}} = \frac{E_t A_T}{2}\int_0^l \mathbf{A}_{ij}\mathbf{A}_{kn}\,\mathrm{d}x, \tag{91}$$

and

$$\mathbf{K}_{2_{ij}} = \frac{E_t A_t}{2} \int_0^l \mathbf{A}_{ij}\, \mathrm{d}x. \tag{92}$$

Similarly, the Jacobian of generalized forces associated to axial strains con be simplified by the consideration of the invariant terms $\mathbf{K}_1$ and $\mathbf{K}_2$, allowing to express

$$\begin{aligned}\frac{\partial \mathbf{Q}_{e_x}}{\partial \mathbf{e}} &= -\frac{\partial \frac{E_t A_t}{2} \int_0^l \mathbf{S}_x^T \mathbf{S}_x \mathbf{e}\, \mathbf{e}^T \mathbf{S}_x^T \mathbf{S}_x \mathbf{e}\, \mathrm{d}x}{\partial \mathbf{e}} + \frac{\partial \frac{E_t A_t}{2} \int_0^l \mathbf{S}_x^T \mathbf{S}_x \mathbf{e}\, \mathrm{d}x}{\partial \mathbf{e}} \\ &= -\frac{E_t A_t}{2} \int_0^l 2\mathbf{S}_x^T \mathbf{S}_x \mathbf{e}\, \mathbf{e}^T \mathbf{S}_x^T \mathbf{S}_x\, \mathrm{d}x - \frac{E_t A_t}{2} \int_0^l (\mathbf{e}^T \mathbf{S}_x^T \mathbf{S}_x \mathbf{e})\, \mathbf{S}_x^T \mathbf{S}_x\, \mathrm{d}x + \frac{E_t A_t}{2} \int_0^l \mathbf{S}_x^T \mathbf{S}_x\, \mathrm{d}x \\ &= -2\mathbf{K}_{1_{ijkn}} \mathbf{e}_j \mathbf{e}_k - \mathbf{K}_{1_{ijkn}} \mathbf{e}_k \mathbf{e}_n + \mathbf{K}_2.\end{aligned} \tag{93}$$

To conclude the formulation of the elastic cable element, the axial contribution of the elastic energy, established as per Eq. (23), can also be expressed considering the invariant matrices $\mathbf{K}_1$ and $\mathbf{K}_2$ as

$$U_{e_x} = \frac{E_t A_t l}{8} + \frac{1}{4}\mathbf{K}_{1_{ijkn}} \mathbf{e}_i \mathbf{e}_j \mathbf{e}_k \mathbf{e}_n - \frac{1}{2}\mathbf{K}_{2_{in}} \mathbf{e}_i \mathbf{e}_n. \tag{94}$$

Nonlinear bending contribution

Regarding the bending contribution, due to the nonlinear character of the curvature κ defined in Eq. (24), it cannot be expressed in terms of the previous invariant matrices, and its integral expression

$$\mathbf{Q}_{e_b} = -E_t I_t \int_0^l \kappa \left(\frac{\partial \kappa}{\partial \mathbf{e}}\right)^T \mathrm{d}x, \tag{95}$$

is evaluated numerically. On one hand, given expression of the second partial derivative of the position with respect to x

$$\mathbf{r}_{,xx} = \frac{\partial^2 \mathbf{S}}{\partial x^2}\, \mathbf{e} = \mathbf{S}_{,xx}\, \mathbf{e}, \tag{96}$$

the curvature κ formulated in Eq. (24) can be expressed as

$$\kappa = \left(\mathbf{r}_{,xx}^T \overline{\mathbf{R}}_{,x}^T \overline{\mathbf{R}}_{,x} \mathbf{r}_{,xx}\right)^{\frac{1}{2}} \left(\mathbf{r}_{,x}^T \mathbf{r}_{,x}\right)^{-\frac{3}{2}} = \mathbf{\Phi}_1^{\frac{1}{2}}\, \mathbf{\Phi}_2^{-\frac{3}{2}}, \tag{97}$$

where the definitions of the functions $\mathbf{\Phi}_1(\mathbf{e}, x) = \mathbf{r}_{,xx}^T \overline{\mathbf{R}}_{,x}^T \overline{\mathbf{R}}_{,x} \mathbf{r}_{,xx}$ and $\mathbf{\Phi}_2(\mathbf{e}, x) = \mathbf{r}_{,x}^T \mathbf{r}_{,x}$ are considered to simplify the expressions. The skew matrix $\overline{\mathbf{R}}_{,x}$, based on the components of slope vector $\mathbf{r}_{,x}$, is defined as

$$\overline{\mathbf{R}}_{,x} = \begin{bmatrix} 0 & -\mathbf{r}_{3,x} & \mathbf{r}_{2,x} \\ \mathbf{r}_{3,x} & 0 & -\mathbf{r}_{1,x} \\ -\mathbf{r}_{2,x} & \mathbf{r}_{1,x} & 0 \end{bmatrix}. \tag{98}$$

On the other hand, the derivative of κ with respect to $\mathbf{e}$ can be expressed as

$$\frac{\partial \kappa}{\partial \mathbf{e}} = \frac{\partial \left(\mathbf{\Phi}_1^{\frac{1}{2}}\, \mathbf{\Phi}_2^{-\frac{3}{2}}\right)}{\partial \mathbf{e}} = \frac{1}{2}\mathbf{\Phi}_1^{-\frac{1}{2}}\, \mathbf{\Phi}_2^{-\frac{3}{2}} \frac{\partial \mathbf{\Phi}_1}{\partial \mathbf{e}} - \frac{3}{2}\mathbf{\Phi}_1^{\frac{1}{2}}\, \mathbf{\Phi}_2^{-\frac{5}{2}} \frac{\partial \mathbf{\Phi}_2}{\partial \mathbf{e}}. \tag{99}$$

All terms in both equations (97) and (99) can be written as a function of the first and second derivatives of the form functions matrix, $\mathbf{S}_{,x}$, and $\mathbf{S}_{,xx}$, and the generalized coordinate vector $\mathbf{e}$, considering the expressions presented in Eq. (100) to Eq. (103)

$$\overline{\mathbf{R}}_{,x}^T \overline{\mathbf{R}}_{,x} = \begin{bmatrix} \mathbf{r}_{2,x}^2 + \mathbf{r}_{3,x}^2 & -\mathbf{r}_{1,x}\mathbf{r}_{2,x} & -\mathbf{r}_{1,x}\mathbf{r}_{3,x} \\ -\mathbf{r}_{1,x}\mathbf{r}_{2,x} & \mathbf{r}_{1,x}^2 + \mathbf{r}_{3,x}^2 & -\mathbf{r}_{2,x}\mathbf{r}_{3,x} \\ -\mathbf{r}_{1,x}\mathbf{r}_{3,x} & -\mathbf{r}_{2,x}\mathbf{r}_{3,x} & \mathbf{r}_{1,x}^2 + \mathbf{r}_{2,x}^2 \end{bmatrix} = \mathbf{r}_{,x}^T \mathbf{r}_{,x} \mathbf{I}_{3x3} - \mathbf{r}_{,x} \mathbf{r}_{,x}^T = \mathbf{e}^T \mathbf{S}_{,x}^T \mathbf{S}_{,x} \mathbf{e}\, \mathbf{I}_{3x3} - \mathbf{S}_{,x} \mathbf{e}\, \mathbf{e}^T \mathbf{S}_{,x}^T, \tag{100}$$

$$\begin{aligned}\boldsymbol{\Phi}_1 = \mathbf{r}_{,xx}^T \overline{\mathbf{R}}_{,x}^T \overline{\mathbf{R}}_{,x} \mathbf{r}_{,xx} &= (\mathbf{r}_{,x}^T \mathbf{r}_{,x})(\mathbf{r}_{,xx}^T \mathbf{r}_{,xx}) - (\mathbf{r}_{,xx}^T \mathbf{r}_{,x})(\mathbf{r}_{,x}^T \mathbf{r}_{,xx}) \\ &= (\mathbf{e}^T \mathbf{S}_{,x}^T \mathbf{S}_{,x} \mathbf{e})(\mathbf{e}^T \mathbf{S}_{,xx}^T \mathbf{S}_{,xx} \mathbf{e}) - (\mathbf{e}^T \mathbf{S}_{,xx}^T \mathbf{S}_{,x} \mathbf{e})(\mathbf{e}^T \mathbf{S}_{,x}^T \mathbf{S}_{,xx} \mathbf{e}),\end{aligned} \tag{101}$$

$$\begin{aligned}\frac{\partial \boldsymbol{\Phi}_1}{\partial \mathbf{e}} = \frac{\partial \left(\mathbf{r}_{,xx}^T \overline{\mathbf{R}}_{,x}^T \overline{\mathbf{R}}_{,x} \mathbf{r}_{,xx} \right)}{\partial \mathbf{e}} =& 2\mathbf{e}^T \mathbf{S}_{,x}^T \mathbf{S}_{,x} (\mathbf{e}^T \mathbf{S}_{,xx}^T \mathbf{S}_{,xx} \mathbf{e}) + 2(\mathbf{e}^T \mathbf{S}_{,x}^T \mathbf{S}_{,x} \mathbf{e}) \mathbf{e}^T \mathbf{S}_{,xx}^T \mathbf{S}_{,xx} \\ &- 2(\mathbf{e}^T \mathbf{S}_{,xx}^T \mathbf{S}_{,x} + \mathbf{e}^T \mathbf{S}_{,x}^T \mathbf{S}_{,xx})(\mathbf{e}^T \mathbf{S}_{,xx}^T \mathbf{S}_{,xx} \mathbf{e}),\end{aligned} \tag{102}$$

$$\frac{\boldsymbol{\Phi}_2}{\partial \mathbf{e}} = \frac{\partial \left(\mathbf{r}_{,x}^T \mathbf{r}_{,x} \right)}{\partial \mathbf{e}} = 2\mathbf{e}^T \mathbf{S}_{,x}^T \mathbf{S}_{,x}. \tag{103}$$

A similar procedure is followed for the formulation of the Jacobian of the bending forces

$$\frac{\partial \mathbf{Q}_{e_b}}{\partial \mathbf{e}} = -E_t I_t \int_0^l \frac{\partial \kappa}{\partial \mathbf{e}} \left(\frac{\partial \kappa}{\partial \mathbf{e}} \right)^T \mathrm{d}x - E_t I_t \int_0^l \kappa \frac{\partial \left(\frac{\partial \kappa}{\partial \mathbf{e}} \right)^T}{\partial \mathbf{e}} \mathrm{d}x. \tag{104}$$

For the first summand, it is sufficient to consider Eq. (99), whereas for the second summand, the second derivative of κ respect to $\mathbf{e}$, can be written as:

$$\begin{aligned}\frac{\partial \left(\frac{\partial \kappa}{\partial \mathbf{e}} \right)^T}{\partial \mathbf{e}} = \frac{\partial}{\partial \mathbf{e}} \left(\frac{1}{2} \frac{\frac{\partial \boldsymbol{\Phi}_1}{\partial \mathbf{e}}}{\boldsymbol{\Phi}_1^{\frac{1}{2}} \boldsymbol{\Phi}_2^{\frac{3}{2}}} - \frac{3}{2} \frac{\boldsymbol{\Phi}_1^{\frac{1}{2}} \frac{\partial \boldsymbol{\Phi}_2}{\partial \mathbf{e}}}{\boldsymbol{\Phi}_2^{\frac{5}{2}}} \right) =& -\frac{1}{4} \frac{\frac{\partial \boldsymbol{\Phi}_1}{\partial \mathbf{e}} \left(\frac{\partial \boldsymbol{\Phi}_1}{\partial \mathbf{e}} \right)^T}{\boldsymbol{\Phi}_1^{\frac{3}{2}} \boldsymbol{\Phi}_2^{\frac{3}{2}}} - \frac{3}{4} \frac{\frac{\partial \boldsymbol{\Phi}_2}{\partial \mathbf{e}} \left(\frac{\partial \boldsymbol{\Phi}_1}{\partial \mathbf{e}} \right)^T}{\boldsymbol{\Phi}_1^{\frac{1}{2}} \boldsymbol{\Phi}_2^{\frac{5}{2}}} + \frac{1}{2} \frac{\frac{\partial}{\partial \mathbf{e}} \left(\frac{\partial \boldsymbol{\Phi}_1}{\partial \mathbf{e}} \right)^T}{\boldsymbol{\Phi}_1^{\frac{1}{2}} \boldsymbol{\Phi}_2^{\frac{3}{2}}} \\ &- \frac{3}{4} \frac{\frac{\partial \boldsymbol{\Phi}_1}{\partial \mathbf{e}} \left(\frac{\partial \boldsymbol{\Phi}_2}{\partial \mathbf{e}} \right)^T}{\boldsymbol{\Phi}_1^{\frac{1}{2}} \boldsymbol{\Phi}_2^{\frac{5}{2}}} + \frac{15}{4} \frac{\frac{\partial \boldsymbol{\Phi}_2}{\partial \mathbf{e}} \left(\frac{\partial \boldsymbol{\Phi}_2}{\partial \mathbf{e}} \right)^T}{\boldsymbol{\Phi}_1^{\frac{1}{2}} \boldsymbol{\Phi}_2^{\frac{7}{2}}} - \frac{3}{2} \frac{\frac{\partial}{\partial \mathbf{e}} \left(\frac{\partial \boldsymbol{\Phi}_2}{\partial \mathbf{e}} \right)^T}{\boldsymbol{\Phi}_1^{\frac{1}{2}} \boldsymbol{\Phi}_2^{\frac{5}{2}}},\end{aligned} \tag{105}$$

where all the terms can be expressed as a function of $\mathbf{S}_{,x}, \mathbf{S}_{,xx}$ and $\mathbf{e}$ considering the expressions obtained in Eq. (101) to Eq. (103), with exception to the second derivative terms, which are specified in Eq. (106)

$$\frac{\partial}{\partial \mathbf{e}} \left(\frac{\partial \boldsymbol{\Phi}_2}{\partial \mathbf{e}} \right)^T = 2\, \mathbf{S}_{,x}^T \mathbf{S}_{,x}, \tag{106}$$

and Eq. (107)

$$\begin{aligned}\frac{\partial}{\partial \mathbf{e}} \left(\frac{\partial \boldsymbol{\Phi}_2}{\partial \mathbf{e}} \right)^T =& 2\, \mathbf{S}_{,x}^T \mathbf{S}_{,x} \left(\mathbf{e}^T \mathbf{S}_{,xx}^T \mathbf{S}_{,xx} \mathbf{e} \right) + 4\, \mathbf{S}_{,x}^T \mathbf{S}_{,x} \mathbf{e}\, \mathbf{e}^T \mathbf{S}_{,xx}^T \mathbf{S}_{,xx} + 2\, \mathbf{S}_{,xx}^T \mathbf{S}_{,xx} \left(\mathbf{e}^T \mathbf{S}_{,x}^T \mathbf{S}_{,x} \mathbf{e} \right) + 4 \mathbf{S}_{,xx}^T \mathbf{S}_{,xx} \mathbf{e}\, \mathbf{e}^T \mathbf{S}_{,x}^T \mathbf{S}_{,x} \\ &- 2 \left(\mathbf{S}_{,x}^T \mathbf{S}_{,xx} + \mathbf{S}_{,xx}^T \mathbf{S}_{,x} \right) \left(\mathbf{e}^T \mathbf{S}_{,xx}^T \mathbf{S}_{,x} \mathbf{e} \right) - 2 \left(\mathbf{S}_{,x}^T \mathbf{S}_{,xx} \mathbf{e} + \mathbf{S}_{,xx}^T \mathbf{S}_{,x} \mathbf{e} \right) \left(\mathbf{e}^T \mathbf{S}_{,xx}^T \mathbf{S}_{,x} + \mathbf{e}^T \mathbf{S}_{,x}^T \mathbf{S}_{,xx} \right).\end{aligned} \tag{107}$$

Finally, the elastic energy due to nonlinear bending U_{e_b}, is calculated by integration of the corresponding term in Eq. (23), by substituting Eq. (101) and Eq. (87) into curvature definition in κ definition presented in Eq. (97).

A.2. Damping contributions

The expressions of the damping energy, the generalized dissipation forces and their Jacobian matrices are derived in detail in this appendix.

Axial contribution

The time derivative of the axial strain $\dot{\epsilon}_{xx}$, can be computed from Eq. (24), and written in term of generalized coordinates position $\mathbf{e}$ and velocity $\dot{\mathbf{e}}$, and shape function matrix derivative $\mathbf{S}_{,x}$, as

$$\dot{\epsilon}_{xx} = \mathbf{e}^T \mathbf{S}_{,x}^T \mathbf{S}_{,x} \dot{\mathbf{e}}, \tag{108}$$

which substituted into the definition of N_{X_v} allows to write the power dissipated due to axial strains P_{d_x}, as

$$P_{d_x} = \frac{\gamma_x E_t A_t}{2} \int_0^l \dot{\epsilon}_{xx}^2 \, \mathrm{d}x = \frac{\gamma_x E_t A_t}{2} \int_0^l \dot{\mathbf{e}}^T \mathbf{S}_x^T \mathbf{S}_x \mathbf{e} \, \mathbf{e}^T \mathbf{S}_x^T \mathbf{S}_x \dot{\mathbf{e}} \, \mathrm{d}x, \tag{109}$$

which can be expressed in terms of the invariant defined in Eq. (91) as

$$P_{d_x} = \frac{\gamma_x E_t A_t}{2} \int_0^l \dot{\epsilon}_{xx}^2 \, \mathrm{d}x = \gamma_x \mathbf{K}_{1_{ijkn}} \dot{\mathbf{e}}_i \mathbf{e}_j \mathbf{e}_k \dot{\mathbf{e}}_n. \tag{110}$$

The generalized force associated to axial damping $\mathbf{Q}_{d_x}$, is obtained by derivation respect to generalized coordinates velocity ($\dot{\mathbf{e}}$) of Eq. 109

$$\begin{aligned} \mathbf{Q}_{d_x} &= -\left(\frac{\partial P_{d_x}}{\partial \dot{\mathbf{e}}} \right)^T = -\frac{E_t A_t \gamma_x}{2} \int_0^l \left(\frac{\partial (\dot{\mathbf{e}}^T \mathbf{S}_x^T \mathbf{S}_x \mathbf{e} \, \mathbf{e}^T \mathbf{S}_x^T \mathbf{S}_x \dot{\mathbf{e}})}{\partial \dot{\mathbf{e}}} \right)^T \mathrm{d}x \\ &= -E_t A_t \gamma_x \int_0^l \mathbf{S}_x^T \mathbf{S}_x \mathbf{e} \mathbf{e}^T \mathbf{S}_x^T \mathbf{S}_x \dot{\mathbf{e}} \, \mathrm{d}x = -2\gamma_x \mathbf{K}_{1_{ijkn}} \mathbf{e}_j \mathbf{e}_k \dot{\mathbf{e}}_n, \end{aligned} \tag{111}$$

also expressed considering the invariant $\mathbf{K}_{1_{ijkn}}$ to avoid the computational overload associated to quadrature calculation at each step. To conclude, the Jacobian matrix of the axial damping forces is derived and written

$$\begin{aligned} \frac{\partial \mathbf{Q}_{d_x}}{\partial \mathbf{e}} &= -E_t A_t \gamma_x \frac{\partial \left(\int_0^l \mathbf{S}_x^T \mathbf{S}_x \mathbf{e} \, \mathbf{e}^T \mathbf{S}_x^T \mathbf{S}_x \dot{\mathbf{e}} \, \mathrm{d}x \right)}{\partial \mathbf{e}} \\ &= -\gamma_x E_t A_t \int_0^l \left(\mathbf{S}_x^T \mathbf{S}_x \mathbf{e} \frac{\partial (\mathbf{e}^T \mathbf{S}_x^T \mathbf{S}_x \dot{\mathbf{e}})}{\partial \mathbf{e}} \right) \mathrm{d}x - \gamma_x E_t A_t \int_0^l \left(\mathbf{e}^T \mathbf{S}_x^T \mathbf{S}_x \dot{\mathbf{e}} \frac{\partial (\mathbf{e}^T \mathbf{S}_x^T \mathbf{S}_x)}{\partial \mathbf{e}} \right) \mathrm{d}x \\ &= -\gamma_x E_t A_t \int_0^l \left(\mathbf{S}_x^T \mathbf{S}_x \mathbf{e} \dot{\mathbf{e}}^T \mathbf{S}_x^T \mathbf{S}_x \right) \mathrm{d}x - \gamma_x E_t A_t \int_0^l \left((\dot{\mathbf{e}}^T \mathbf{S}_x^T \mathbf{S}_x \mathbf{e}) \mathbf{S}_x^T \mathbf{S}_x \right) \mathrm{d}x \\ &= -2\gamma_x \mathbf{K}_{1_{ijkn}} \mathbf{e}_j \mathbf{e}_k - \gamma_x E_t A_t \int_0^l (\dot{\mathbf{e}}^T \mathbf{S}_x^T \mathbf{S}_x \mathbf{e}) \, \mathbf{S}_x^T \mathbf{S}_x \, \mathrm{d}x, \end{aligned} \tag{112}$$

where it is not possible to elude the existence of an integral term that needs to be computed at every time step and element.

Nonlinear bending contribution

In the case of bending damping, the use of invariant matrices to simplify the calculation and reduce computation time is not possible and all the expressions need to be calculated by numerical integration, for which six integration points are used. However, a compact formulation in terms of the shape functions matrix $\mathbf{S}$ and it first $\mathbf{S}_{,x}$ and second derivative $\mathbf{S}_{,xx}$ is presented. Given that the form matrices are function of x and all the elements are created owning the same length, a single evaluation of the shape functions matrices can be used for the quadrature of all the elements at all the steps, and the use of computing resources is partially alleviated.

Keeping previous comments in mind, the time derivative of the curvature $\dot{\kappa}$, needed for the dissipation power associated to bending P_{d_b}, can be written considering the definition of $\mathbf{\Phi}_1$ and $\mathbf{\Phi}_2$ presented in Sect. A.1 as

$$\dot{\kappa} = \frac{\partial \kappa}{\partial t} = \frac{1}{2} \mathbf{\Phi}_1^{-\frac{1}{2}} \mathbf{\Phi}_2^{-\frac{3}{2}} \frac{\partial \mathbf{\Phi}_1}{\partial t} - \frac{3}{2} \mathbf{\Phi}_1^{\frac{1}{2}} \mathbf{\Phi}_2^{-\frac{5}{2}} \frac{\partial \mathbf{\Phi}_2}{\partial t}, \tag{113}$$

where all the terms can be written as a function of the first and second derivatives of the form functions matrix ($\mathbf{S}_{,x}, \mathbf{S}_{,xx}$), and the generalized coordinate vector ($\mathbf{e}$), considering Eq. (87), Eq. (101) and its time derivative

$$\frac{\partial \mathbf{\Phi}_1}{\partial t} = 2\ \mathbf{e}^T\mathbf{S}_{,x}^T\mathbf{S}_{,x}\dot{\mathbf{e}}\ \mathbf{e}^T\mathbf{S}_{,xx}^T\mathbf{S}_{,xx}\mathbf{e} + 2\ \mathbf{e}^T\mathbf{S}_{,x}^T\mathbf{S}_{,x}\mathbf{e}\ \mathbf{e}^T\mathbf{S}_{,xx}^T\mathbf{S}_{,xx}\dot{\mathbf{e}} - 2\left(\mathbf{e}^T\mathbf{S}_{,xx}^T\mathbf{S}_{,x}\dot{\mathbf{e}} + \mathbf{e}^T\mathbf{S}_{,x}^T\mathbf{S}_{,xx}\dot{\mathbf{e}}\right)\left(\mathbf{e}^T\mathbf{S}_{,x}^T\mathbf{S}_{,xx}\mathbf{e}\right). \tag{114}$$

and the time derivative of Eq. (103), which can be written as

$$\frac{\partial \mathbf{\Phi}_2}{\partial t} = 2\mathbf{e}^T\mathbf{S}_{,x}^T\mathbf{S}_{,x}\dot{\mathbf{e}}. \tag{115}$$

The generalized damping force associated to bending deformation is obtained by derivation with respect to generalized coordinates time derivative ($\dot{\mathbf{e}}$) of corresponding power P_{d_b}

$$\mathbf{Q}_{d_b} = -\left(\frac{\partial P_{d_b}}{\partial \dot{\mathbf{e}}}\right)^T = -\gamma_b E_t I_t \int_0^l \dot{\kappa}\left(\frac{\partial \dot{\kappa}}{\partial \dot{\mathbf{e}}}\right)^T \mathrm{d}x, \tag{116}$$

where the term $\partial\dot{\kappa}/\partial\dot{\mathbf{e}}$ is defined as

$$\frac{\partial \dot{\kappa}}{\partial \dot{\mathbf{e}}} = \frac{1}{2}\mathbf{\Phi}_1^{-\frac{1}{2}}\mathbf{\Phi}_2^{-\frac{3}{2}}\frac{\partial}{\partial \dot{\mathbf{e}}}\left(\frac{\partial \mathbf{\Phi}_1}{\partial t}\right) - \frac{3}{2}\mathbf{\Phi}_1^{\frac{1}{2}}\mathbf{\Phi}_2^{-\frac{5}{2}}\frac{\partial}{\partial \dot{\mathbf{e}}}\left(\frac{\partial \mathbf{\Phi}_2}{\partial t}\right), \tag{117}$$

and the derivation respect to $\dot{\mathbf{e}}$ of Eq. (115) and Eq. (119) results in

$$\frac{\partial}{\partial \dot{\mathbf{e}}}\left(\frac{\partial \mathbf{\Phi}_2}{\partial t}\right) = 2\mathbf{e}^T\mathbf{S}_{,x}^T\mathbf{S}_{,x}, \tag{118}$$

and

$$\frac{\partial}{\partial \dot{\mathbf{e}}}\left(\frac{\partial \mathbf{\Phi}_2}{\partial t}\right) = 2\mathbf{e}^T\mathbf{S}_{,xx}^T\mathbf{S}_{,xx}\mathbf{e}\ \mathbf{e}^T\mathbf{S}_{,x}^T\mathbf{S}_{,x}\ + 2\ \mathbf{e}^T\mathbf{S}_{,x}^T\mathbf{S}_{,x}\mathbf{e}\ \mathbf{e}^T\mathbf{S}_{,xx}^T\mathbf{S}_{,xx} - 2\left(\mathbf{e}^T\mathbf{S}_{,xx}^T\mathbf{S}_{,x} + \mathbf{e}^T\mathbf{S}_{,x}^T\mathbf{S}_{,xx}\right)\left(\mathbf{e}^T\mathbf{S}_{,x}^T\mathbf{S}_{,xx}\mathbf{e}\right), \tag{119}$$

which allow to complete the force formulation. The Jacobian of the bending damping force respect to the generalized coordinates $\mathbf{e}$ is expressed as

$$\begin{aligned}\frac{\partial \mathbf{Q}_{d_b}}{\partial \mathbf{e}} &= -\frac{\partial}{\partial \mathbf{e}}\left(\left(\frac{\partial P_{d_{bd}}}{\partial \dot{\mathbf{e}}}\right)^T\right) = -\gamma_b E_t I_t \int_0^l \frac{\partial}{\partial \mathbf{e}}\left(\dot{\kappa}\left(\frac{\partial \dot{\kappa}}{\partial \dot{\mathbf{e}}}\right)^T\right)\mathrm{d}x \\ &= -\gamma_b E_t I_t \int_0^l \left(\frac{\partial \dot{\kappa}}{\partial \dot{\mathbf{e}}}\right)^T \frac{\partial \dot{\kappa}}{\partial \mathbf{e}}\,\mathrm{d}x - \gamma_b E_t I_t \int_0^l \dot{\kappa}\frac{\partial}{\partial \mathbf{e}}\left(\left(\frac{\partial \dot{\kappa}}{\partial \dot{\mathbf{e}}}\right)^T\right)\mathrm{d}x.\end{aligned} \tag{120}$$

Where the term $\partial\dot{\kappa}/\partial\dot{\mathbf{e}}$ is defined by Eq. (117) to Eq. (119), the expression $\partial\dot{\kappa}/\partial\mathbf{e}$ can be written as

$$\begin{aligned}\frac{\partial \dot{\kappa}}{\partial \mathbf{e}} =& \frac{1}{2}\frac{\partial \mathbf{\Phi}_1}{\partial t}\left(-\frac{1}{2}\mathbf{\Phi}_1^{-\frac{3}{2}}\mathbf{\Phi}_2^{-\frac{3}{2}}\frac{\partial \mathbf{\Phi}_1}{\partial \mathbf{e}} - \frac{3}{2}\mathbf{\Phi}_1^{-\frac{1}{2}}\mathbf{\Phi}_2^{-\frac{5}{2}}\frac{\partial \mathbf{\Phi}_2}{\partial \mathbf{e}}\right) + \frac{1}{2}\mathbf{\Phi}_1^{-\frac{1}{2}}\mathbf{\Phi}_2^{-\frac{3}{2}}\frac{\partial}{\partial \mathbf{e}}\left(\frac{\partial \mathbf{\Phi}_1}{\partial t}\right) \\ &- \frac{3}{2}\frac{\partial \mathbf{\Phi}_2}{\partial t}\left(\frac{1}{2}\mathbf{\Phi}_1^{-\frac{1}{2}}\mathbf{\Phi}_2^{-\frac{5}{2}}\frac{\partial \mathbf{\Phi}_1}{\partial \mathbf{e}} - \frac{5}{2}\mathbf{\Phi}_1^{\frac{1}{2}}\mathbf{\Phi}_2^{-\frac{7}{2}}\frac{\partial \mathbf{\Phi}_2}{\partial \mathbf{e}}\right) - \frac{3}{2}\mathbf{\Phi}_1^{\frac{1}{2}}\mathbf{\Phi}_2^{-\frac{5}{2}}\frac{\partial}{\partial \mathbf{e}}\left(\frac{\partial \mathbf{\Phi}_2}{\partial t}\right),\end{aligned} \tag{121}$$

being possible to calculate the terms $\partial\left(\partial\mathbf{\Phi}_1/\partial t\right)/\partial\mathbf{e}$ and $\partial\left(\partial\mathbf{\Phi}_2/\partial t\right)/\partial\mathbf{e}$, by derivation of Eq. (114) and Eq. (115) respectively

$$\begin{aligned}\frac{\partial}{\partial \mathbf{e}}\left(\frac{\partial \mathbf{\Phi}_1}{\partial t}\right) =& 2\left(\mathbf{e}^T\mathbf{S}_{,xx}^T\mathbf{S}_{,xx}\mathbf{e}\right)\dot{\mathbf{e}}^T\mathbf{S}_{,x}^T\mathbf{S}_{,x} + 4\left(\mathbf{e}^T\mathbf{S}_{,x}^T\mathbf{S}_{,x}\dot{\mathbf{e}}\right)\mathbf{e}^T\mathbf{S}_{,xx}^T\mathbf{S}_{,xx} + 4\left(\mathbf{e}^T\mathbf{S}_{,xx}^T\mathbf{S}_{,xx}\dot{\mathbf{e}}\right)\mathbf{e}^T\mathbf{S}_{,x}^T\mathbf{S}_{,x} \\ &+ 2\left(\mathbf{e}^T\mathbf{S}_{,x}^T\mathbf{S}_{,x}\mathbf{e}\right)\dot{\mathbf{e}}^T\mathbf{S}_{,xx}^T\mathbf{S}_{,xx} - 2\left(\mathbf{e}^T\mathbf{S}_{,x}^T\mathbf{S}_{,xx}\mathbf{e}\right)\left(\dot{\mathbf{e}}^T\mathbf{S}_{,x}^T\mathbf{S}_{,xx} + \dot{\mathbf{e}}^T\mathbf{S}_{,xx}^T\mathbf{S}_{,x}\right) \\ &- 2\left(\mathbf{e}^T\mathbf{S}_{,xx}^T\mathbf{S}_{,x}\dot{\mathbf{e}} + \mathbf{e}^T\mathbf{S}_{,x}^T\mathbf{S}_{,xx}\dot{\mathbf{e}}\right)\left(\mathbf{e}^T\mathbf{S}_{,x}^T\mathbf{S}_{,xx} + \mathbf{e}^T\mathbf{S}_{,xx}^T\mathbf{S}_{,x}\right),\end{aligned} \tag{122}$$

and

$$\frac{\partial}{\partial \mathbf{e}}\left(\frac{\partial \mathbf{\Phi}_2}{\partial t}\right) = 2\dot{\mathbf{e}}^T \mathbf{S}_{,x}^T \mathbf{S}_{,x}. \tag{123}$$

Finally, the term $\partial\left((\partial\dot{\kappa}/\partial\dot{\mathbf{e}})^T\right)/\partial\mathbf{e}$, can be expressed as

$$\begin{aligned}\frac{\partial}{\partial \mathbf{e}}\left(\left(\frac{\partial \dot{\kappa}}{\partial \dot{\mathbf{e}}}\right)^T\right) =& \frac{1}{2}\left(\frac{\partial}{\partial \dot{\mathbf{e}}}\left(\frac{\partial \mathbf{\Phi}_1}{\partial t}\right)\right)^T\left(-\frac{1}{2}\mathbf{\Phi}_1^{-\frac{3}{2}}\mathbf{\Phi}_2^{-\frac{3}{2}}\frac{\partial \mathbf{\Phi}_1}{\partial \mathbf{e}} - \frac{3}{2}\mathbf{\Phi}_1^{-\frac{1}{2}}\mathbf{\Phi}_2^{-\frac{5}{2}}\frac{\partial \mathbf{\Phi}_2}{\partial \mathbf{e}}\right)\\ &+\left(-\frac{3}{4}\mathbf{\Phi}_1^{-\frac{1}{2}}\mathbf{\Phi}_2^{-\frac{5}{2}}\frac{\partial \mathbf{\Phi}_1}{\partial \mathbf{e}} + \frac{15}{4}\mathbf{\Phi}_1^{\frac{1}{2}}\mathbf{\Phi}_2^{-\frac{7}{2}}\frac{\partial \mathbf{\Phi}_2}{\partial \mathbf{e}}\right)\left(\frac{\partial}{\partial \dot{\mathbf{e}}}\left(\frac{\partial \mathbf{\Phi}_2}{\partial t}\right)\right)^T\\ &-\frac{3}{2}\mathbf{\Phi}_1^{\frac{1}{2}}\mathbf{\Phi}_2^{-\frac{5}{2}}\frac{\partial}{\partial \mathbf{e}}\left(\left(\frac{\partial}{\partial \dot{\mathbf{e}}}\left(\frac{\partial \mathbf{\Phi}_2}{\partial t}\right)\right)^T\right) + \frac{1}{2}\mathbf{\Phi}_1^{-\frac{1}{2}}\mathbf{\Phi}_2^{-\frac{3}{2}}\frac{\partial}{\partial \mathbf{e}}\left(\left(\frac{\partial}{\partial \dot{\mathbf{e}}}\left(\frac{\partial \mathbf{\Phi}_1}{\partial t}\right)\right)^T\right),\end{aligned} \tag{124}$$

being

$$\begin{aligned}\frac{\partial}{\partial \mathbf{e}}\left(\left(\frac{\partial}{\partial \dot{\mathbf{e}}}\left(\frac{\partial \mathbf{\Phi}_1}{\partial t}\right)\right)^T\right) =& 4\mathbf{S}_{,x}^T\mathbf{S}_{,x}\mathbf{e}\,\mathbf{e}^T\mathbf{S}_{,xx}^T\mathbf{S}_{,xx} + 2\left(\mathbf{e}^T\mathbf{S}_{,xx}^T\mathbf{S}_{,xx}\mathbf{e}\right)\mathbf{S}_{,x}^T\mathbf{S}_{,x} + 4\mathbf{S}_{,xx}^T\mathbf{S}_{,xx}\mathbf{e}\,\mathbf{e}^T\mathbf{S}_{,x}^T\mathbf{S}_{,x}\\ &+2\left(\mathbf{e}^T\mathbf{S}_{,x}^T\mathbf{S}_{,x}\mathbf{e}\right)\mathbf{S}_{,xx}^T\mathbf{S}_{,xx} - 2\left(\mathbf{S}_{,x}^T\mathbf{S}_{,xx} + \mathbf{S}_{,xx}^T\mathbf{S}_{,x}\right)\left(\mathbf{e}^T\mathbf{S}_{,x}^T\mathbf{S}_{,xx}\mathbf{e}\right)\\ &-2\left(\mathbf{S}_{,x}^T\mathbf{S}_{,xx}\mathbf{e} + \mathbf{S}_{,xx}^T\mathbf{S}_{,x}\mathbf{e}\right)\left(\mathbf{e}^T\mathbf{S}_{,x}^T\mathbf{S}_{,xx} + \mathbf{e}^T\mathbf{S}_{,xx}^T\mathbf{S}_{,x}\right),\end{aligned} \tag{125}$$

and

$$\frac{\partial}{\partial \mathbf{e}}\left(\left(\frac{\partial}{\partial \dot{\mathbf{e}}}\left(\frac{\partial \mathbf{\Phi}_2}{\partial t}\right)\right)^T\right) = 2\mathbf{S}_{,x}^T\mathbf{S}_{,x}. \tag{126}$$

Last but not least, the Jacobian respect to the generalized velocity $\dot{\mathbf{e}}$, also used for the integration using generalized-α algorithm is written as

$$\frac{\partial \mathbf{Q}_{d_b}}{\partial \dot{\mathbf{e}}} = -\frac{\partial}{\partial \dot{\mathbf{e}}}\left(\left(\frac{\partial P_{d_{bd}}}{\partial \dot{\mathbf{e}}}\right)^T\right) = -\gamma_b E_t I_t \int_0^l \frac{\partial}{\partial \dot{\mathbf{e}}}\left(\dot{\kappa}\left(\frac{\partial \dot{\kappa}}{\partial \dot{\mathbf{e}}}\right)^T\right)\mathrm{d}x = -\gamma_b E_t I_t \int_0^l \left(\frac{\partial \dot{\kappa}}{\partial \dot{\mathbf{e}}}\right)^T\left(\frac{\partial \dot{\kappa}}{\partial \dot{\mathbf{e}}}\right)\mathrm{d}x, \tag{127}$$

where the expression for all the intervening terms are known.

B. Rigid body formulation

This appendix contains the detailed description of the NC formulation of the rigid body.

The position of any point of the solid can be expressed as the position of the origin of the local coordinate system $\mathbf{r}_1$, plus the rotation matrix $\mathbf{C}_B^I$, associated to the transformation from the local frame, which is parallel to B, to the global frame I, multiplied by the point coordinates respect to the local frame $\mathbf{x} = \begin{bmatrix} x & y & z \end{bmatrix}^T$, resulting

$$\mathbf{r} = \mathbf{r}_1 + \mathbf{C}_B^I\,\mathbf{x}. \tag{128}$$

The matrix $\mathbf{C}_B^I$ is formed by three orthonormal vectors $\mathbf{i}_B$, $\mathbf{j}_B$ and $\mathbf{z}_B$, thus $\mathbf{C}_B^I = \begin{bmatrix}\mathbf{i}_B & \mathbf{j}_B & \mathbf{k}_B\end{bmatrix}$, conforming a base of the $\mathbb{R}^3$ space. Given the non co-planar condition imposed to the selection of the four points of the solid used for the solid formulation, the origin of the local frame is set at $\mathbf{r}_1$ and the frame unitary vector are calculated as

$$\mathbf{i}_B = \frac{\mathbf{r}_{AB}}{\|\,\mathbf{r}_{AB}\,\|},\ \mathbf{k}_B = \frac{\mathbf{u}\times\mathbf{r}_{AC}}{\|\,\mathbf{u}\times\mathbf{r}_{AC}\,\|},\ \mathbf{j}_B = \mathbf{k}_B\times\mathbf{i}_B. \tag{129}$$

Given the restriction previously exposed for the selection of the base points, the vectors conforming the local base can be expressed as a linear combination of the form:

$$\begin{aligned}\mathbf{i}_B &= \alpha_1\,\mathbf{r}_{AB} + \alpha_2\,\mathbf{r}_{AC} + \alpha_3\,\mathbf{r}_{AD},\\ \mathbf{j}_B &= \beta_1\,\mathbf{r}_{AB} + \beta_2\,\mathbf{r}_{AC} + \beta_3\,\mathbf{r}_{AD},\\ \mathbf{k}_B &= \gamma_1\,\mathbf{r}_{AB} + \gamma_2\,\mathbf{r}_{AC} + \gamma_3\,\mathbf{r}_{AD}.\end{aligned} \tag{130}$$

It can be verified that substituting Eq.(130) into Eq.(129) and operating, the position of any point of the solid can be written as expressed by Eq. (39). Being the definition of the matrix $\mathbf{G}$

$$\mathbf{G} = \begin{bmatrix} g_1\mathbf{I} & g_2\mathbf{I} & g_3\mathbf{I} & g_4\mathbf{I}\end{bmatrix}, \tag{131}$$

where the coefficients g_1 to g_4 depends of the local point coordinates $\mathbf{x}$ and have the following expressions

$$\begin{gathered} g_1 = 1 - x\sum_{j=1}^{3}\boldsymbol{\alpha}(j) - y\sum_{j=1}^{3}\boldsymbol{\beta}(j) - z\sum_{j=1}^{3}\boldsymbol{\gamma}(j),\;\; g_2 = x\cdot\alpha_1 + y\cdot\beta_1 + z\cdot\gamma_1,\\ g_3 = x\cdot\alpha_2 + y\cdot\beta_2 + z\cdot\gamma_2,\;\; g_4 = x\cdot\alpha_3 + y\cdot\beta_3 + z\cdot\gamma_3.\end{gathered} \tag{132}$$

It should be noted that vectors $\boldsymbol{\alpha}$, $\boldsymbol{\beta}$ and $\boldsymbol{\gamma}$ are constant, given the rigid body assumption. Considering Eq. (130) and (134) the mentioned vector variables, $\boldsymbol{\alpha}$, $\boldsymbol{\beta}$ and $\boldsymbol{\gamma}$, can be calculated by solving, just once, the linear systems

$$\mathbf{B}\boldsymbol{\alpha} = \mathbf{i}_B,\; \mathbf{B}\boldsymbol{\beta} = \mathbf{j}_B,\; \mathbf{B}\boldsymbol{\gamma} = \mathbf{k}_B, \tag{133}$$

where the matrix $\mathbf{B}$ is defined as:

$$\mathbf{B} = \begin{bmatrix}\mathbf{r}_{AB} & \mathbf{r}_{AC} & \mathbf{r}_{AD}\end{bmatrix}. \tag{134}$$

C. Comparison of cable and truss

This appendix presents additional information allowing the comparison of simulation results under the use of cable elements, considering axial and bending stiffness, and truss elements, accounting exclusively for axial contribution. The results correspond to the baseline configuration, presented in Table 1, and a $\alpha = 10$deg.

The times histories for simulation results considering five cable elements and nine truss elements for tethers idealization are provided. The coning angle, γ, root coning angle, γ', lagging angle, β, and root lagging angle, β', for tether 1 are described in Figs. 11 (a1) to (b3), respectively. The Figs. 11 (c1) to (c3), contains the evolution of the central vehicle absolute angular rates, $\boldsymbol{\omega}^B$. Finally, the central vehicle Euler angles, ψ, θ and ϕ, are provided in Figs. 11 (d1) to (d3).

The total thrust is described in Figs. 12 (a1) to (a3), while the total Lagrange multiplier are represented in Figs. 12 (b1) to (b3). In addition, the total thrust moments is presented in Figs. 12 (c1) to (c3) and the total Lagrange multiplier moment is presented in Figs. 12 (d1) to (d3).

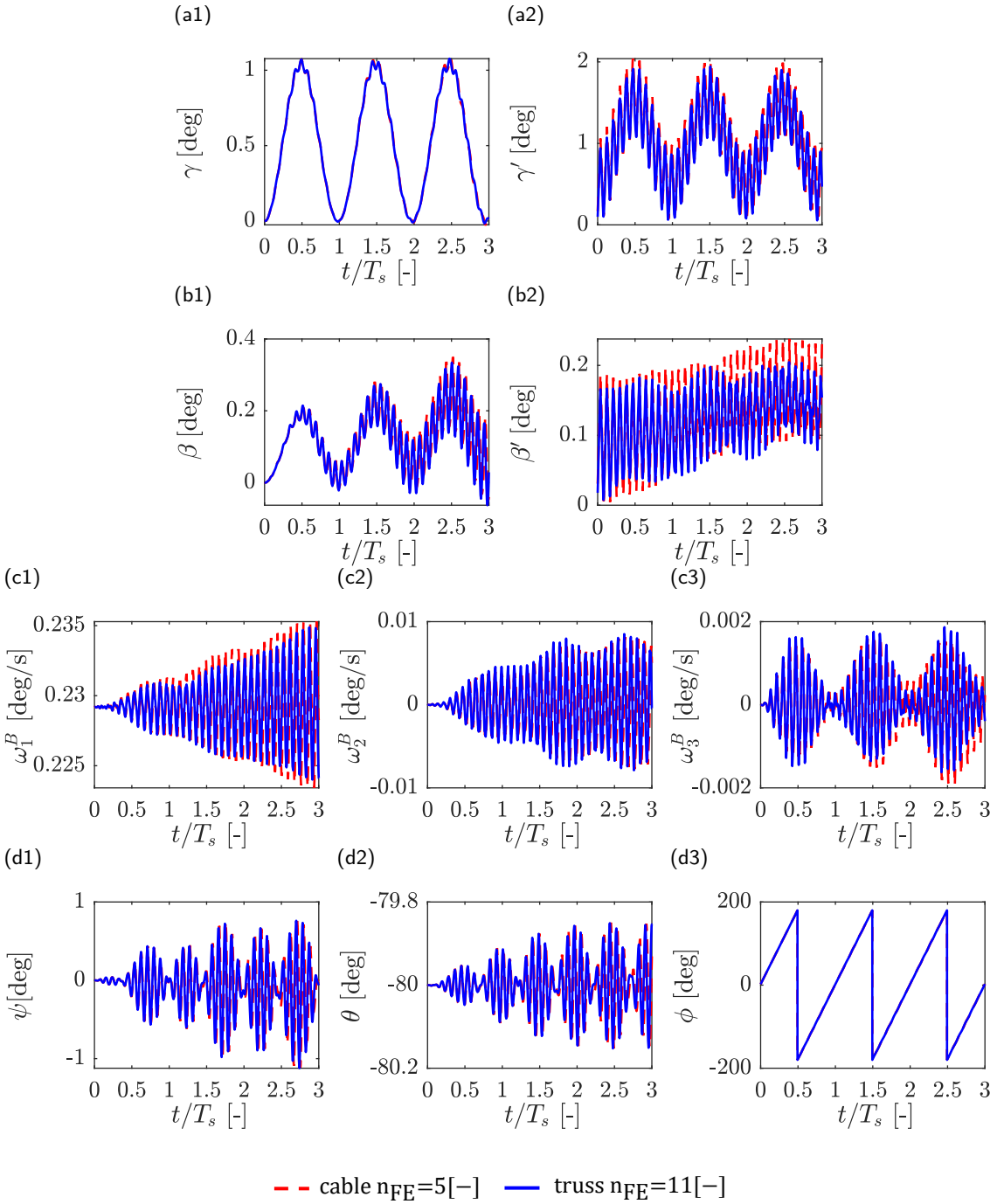

Figure 11: Comparison of simulation results obtained for the E-sail baseline configuration under non-symmetrical (α=10 deg) operation, considering different idealizations for the flexible tethers: (a1) Coning angle γ for tether 1; (a2) Root coning angle γ' for tether 1; (b1) Lagging angle β for tether 1; (b2) Root lagging angle β' for tether 1; (c1) to (c3) Central vehicle absolute angular rates $\boldsymbol{\omega}^B$; and (d1) to (d3) Central vehicle Euler angles ψ, θ and ϕ.

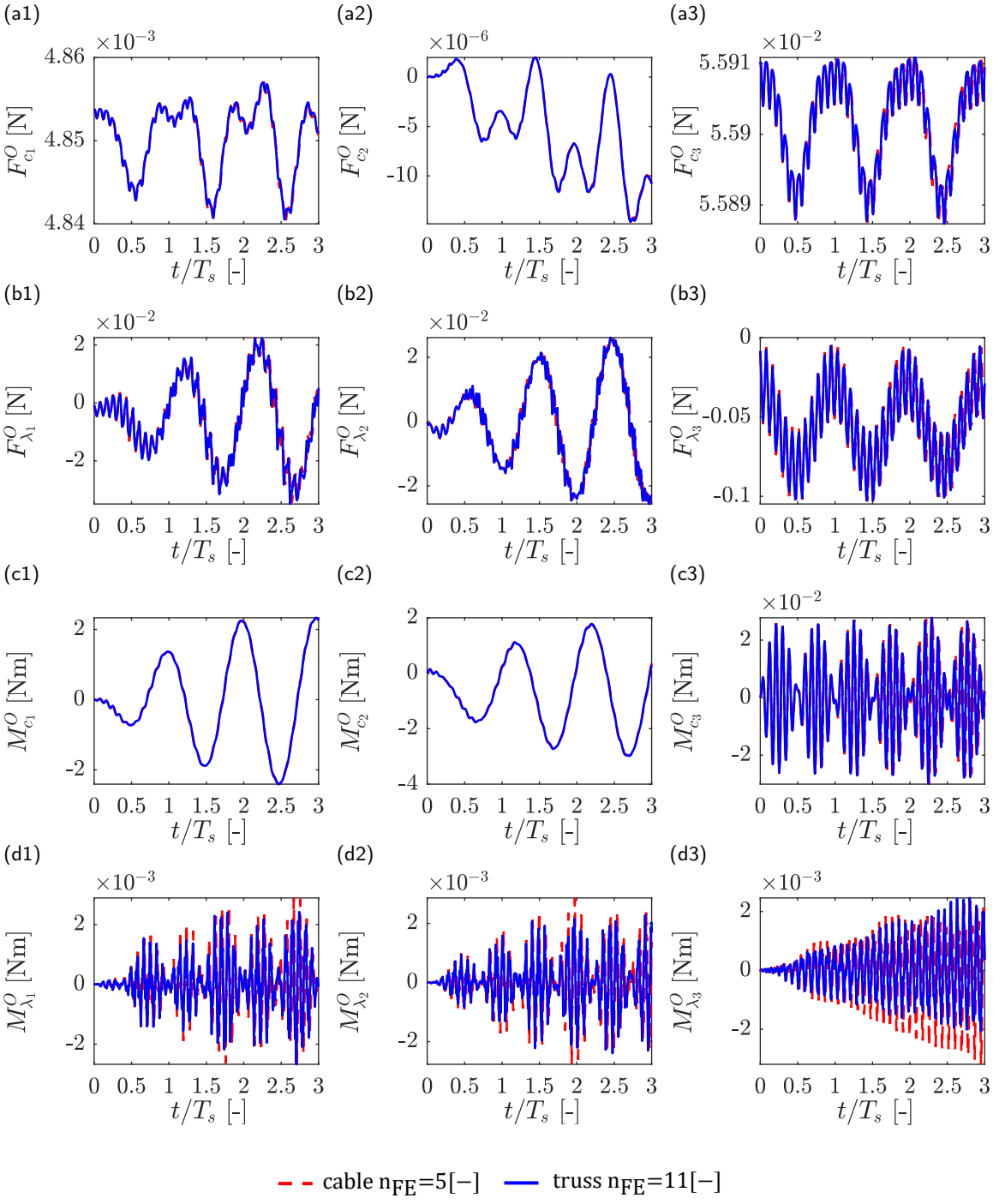

Figure 12: Comparison of simulation results obtained for the E-sail baseline configuration under non-symmetrical (α=10 deg) operation, considering different idealizations for the flexible tethers: (a1) to (a3) Thrust force components in orbit frame; (b1) to (b3) Total Lagrange multiplier components in orbit frame; (c1) to (c3) Thrust Moment components in orbit frame; and (d1) to (d3) Total Lagrange multiplier Moment components in orbit frame.

D. Supplementary data

The following is the Supplementary material related to this article.

CRediT authorship contribution statement

Guillermo Pacheco-Ramos: Conceptualization of this study, Methodology, Software. **Daniel Garcia-Vallejo:** Conceptualization of this study, Methodology, Software. **Rafael Vazquez:** Conceptualization of this study, Methodology, Software.

References

[1] P. Janhunen, Electric sail for spacecraft propulsion, Journal of Propulsion and Power 20 (2004) 763–764. doi:10.2514/1.8580.

[2] M. Bassetto, L. Niccolai, A. A. Quarta, G. Mengali, A comprehensive review of Electric Solar Wind Sail concept and its applications, Progress in Aerospace Sciences 128 (September 2021) (2022) 100768. doi:10.1016/j.paerosci.2021.100768.

[3] P. Janhunen, A. Sandroos, Simulation study of solar wind push on a charged wire: Basis of solar wind electric sail propulsion, Annales Geophysicae 25 (2007) 755–767. doi:10.5194/angeo-25-755-2007.

[4] P. Janhunen, PIC simulation of electric sail with explicit trapped electron modeling, ASP Conference Series 459 (2012) 271–276.

[5] A. Sanchez-Torres, Propulsive force in an electric solar sail, Contributions to Plasma Physics 54 (2014) 314–319. doi:10.1002/ctpp.201410077.

[6] P. Janhunen, Boltzmann electron PIC simulation of the E-sail effect, Ann. Geophys 33 (2015) 1507–1512. doi:10.5194/angeo-33-1507-2015.

[7] W. B. M., Summary of nasa's electric sail propulsion investigations 2014-2017, AIAA Aerospace Sciences Meeting (2018). doi:10.2514/6.2018-1536.

[8] P. K. Toivanen, P. Janhunen, Spin plane control and thrust vectoring of electric solar wind sail, Journal of Propulsion and Power 29 (2013) 178–185. doi:10.2514/1.B34330.

[9] G. Mengali, A. A. Quarta, P. Janhunen, Electric sail performance analysis, Journal of Spacecraft and Rockets 45 (2008) 122–129. doi:10.2514/1.31769.

[10] P. Janhunen, Status report of the electric sail in 2009, Vol. 68, 2011, pp. 567–570. doi:10.1016/j.actaastro.2010.02.007.

[11] B. M. Wiegmann, T. Scheider, A. Heaton, J. Vaughn, N. Stone, K. Wright, The heliopause electrostatic rapid transit system (herts) - design, trades, and analyses performed in a two year nasa investigation of electric sail propulsion systems, American Institute of Aeronautics and Astronautics Inc, AIAA, 2017. doi:10.2514/6.2017-4712.

[12] M. Huo, G. Mengali, A. A. Quarta, Optimal planetary rendezvous with an electric sail, Aircraft Engineering and Aerospace Technology 88 (2016) 515–522. doi:10.1108/AEAT-01-2015-0012.

[13] M. Huo, J. Zhao, S. Xie, N. Qi, Coupled attitude-orbit dynamics and control for an electric sail in a heliocentric transfer mission, PLoS ONE 10 (2015) 1–14. doi:10.1371/journal.pone.0125901.

[14] M. Bassetto, A. A. Quarta, G. Mengali, Locally-optimal electric sail transfer, Proceedings of the Institution of Mechanical Engineers, Part G: Journal of Aerospace Engineering 233 (2019) 166–179. doi:10.1177/0954410017728975.

[15] M. Huo, H. Liao, Y. Liu, N. Qi, The coupled orbit-attitude dynamics and control of electric sail in displaced solar orbits, International Journal of Aerospace Engineering 2017 (2017). doi:10.1155/2017/3812397.

[16] P. Janhunen, P. K. Toivanen, J. Polkko, S. Merikallio, P. Salminen, E. Haeggström, H. Seppänen, R. Kurppa, J. Ukkonen, S. Kiprich, G. Thornell, H. Kratz, L. Richter, O. Krömer, R. Rosta, M. Noorma, J. Envall, S. Lätt, G. Mengali, A. A. Quarta, H. Koivisto, O. Tarvainen, T. Kalvas, J. Kauppinen, A. Nuottajärvi, A. Obraztsov, Invited article: Electric solar wind sail: Toward test missions, Review of Scientific Instruments 81 (2010). doi:10.1063/1.3514548.

[17] P. Janhunen, Photonic spin control for solar wind electric sail, Acta Astronautica 83 (2013) 85–90. doi:10.1016/j.actaastro.2012.10.017.

[18] P. Janhunen, P. Toivanen, An intrinsic way to control e-sail spin (2014). doi:10.48550/ARXIV.1406.6847.

[19] P. Toivanen, P. Janhunen, J. Envall, Electric sail control mode for amplified transverse thrust, Acta Astronautica 106 (2015) 111–119. doi:10.1016/j.actaastro.2014.10.031.

[20] P. Toivanen, P. Janhunen, Thrust vectoring of an electric solar wind sail with a realistic sail shape, Acta Astronautica 131 (2017) 145–151. doi:10.1016/j.actaastro.2016.11.027.

[21] M. Bassetto, G. Mengali, A. A. Quarta, Thrust and torque vector characteristics of axially-symmetric E-sail, Acta Astronautica 146 (2018) 134–143. doi:10.1016/j.actaastro.2018.02.035.

[22] M. Bassetto, G. Mengali, A. A. Quarta, Attitude dynamics of an electric sail model with a realistic shape, Acta Astronautica 159 (2019) 250–257. doi:10.1016/j.actaastro.2019.03.064.

[23] M. Bassetto, G. Mengali, A. A. Quarta, E-sail attitude control with tether voltage modulation, Acta Astronautica 166 (2020) 350–357. doi:10.1016/j.actaastro.2019.10.023.

[24] P. Janhunen, P. Toivanen, TI tether rig for solving secular spinrate change problem of electric sail (2016). doi:10.48550/arXiv.1603.05563.

[25] F. Liu, Q. Hu, J. Zhang, K. Yang, Y. Li, Dynamics of single charged wire for solar wind electric sail dynamics of single charged wire for solar wind electric sail, 31st International Symposiumon Space Technology and Sciences, Japan Soc. for Aeronautical and Space Sciences Paper 2017-o-1-05, Tokyo, Japan, 2017.

[26] G. Q. Li, Z. H. Zhu, Long-term dynamic modeling of tethered spacecraft using nodal position finite element method and symplectic integration, Celestial Mechanics and Dynamical Astronomy 123 (2015) 363–386. doi:10.1007/s10569-015-9640-5.

[27] G. Li, Z. H. Zhu, J. Cain, F. Newland, A. Czekanski, Libration control of bare electrodynamic tethers considering elastic-thermal-electrical coupling, Journal of Guidance, Control, and Dynamics 39 (2016) 642–654. doi:10.2514/1.G001338.

[28] G. Li, Z. H. Zhu, C. Du, S. A. Meguid, Characteristics of coupled orbital-attitude dynamics of flexible electric solar wind sail, Acta Astronautica 159 (2019) 593–608. doi:10.1016/j.actaastro.2019.02.009.

[29] G. Li, Z. H. Zhu, C. Du, Flight dynamics and control strategy of electric solar wind sails, Journal of Guidance, Control, and Dynamics 43 (2020) 462–474. doi:10.2514/1.G004608.

[30] C. Du, Z. H. Zhu, G. Li, Analysis of thrust-induced sail plane coning and attitude motion of electric sail, Acta Astronautica 178 (2021) 129–142. doi:10.1016/j.actaastro.2020.09.001.

[31] F. Liu, Q. Hu, Y. Liu, Attitude dynamics of electric sail from multibody perspective, Journal of Guidance, Control, and Dynamics 41 (2018) 2633–2646. doi:10.2514/1.G003625.

[32] C. Du, Z. H. Zhu, G. Li, Rigid-flexible coupling effect on attitude dynamics of electric solar wind sail, Communications in Nonlinear Science and Numerical Simulation 95 (2021) 105663. doi:10.1016/j.cnsns.2020.105663.

[33] H. Ren, T. Yuan, M. Huo, C. Zhao, S. Zeng, Dynamics and control of a full-scale flexible electric solar wind sail spacecraft, Aerospace Science and Technology 119 (2021) 107087. doi:10.1016/j.ast.2021.107087.

[34] C. Zhao, M. Huo, J. Qi, S. Cao, D. Zhu, L. Sun, H. Sun, N. Qi, Coupled attitude-vibration analysis of an E-sail using absolute nodal coordinate formulation, Astrodynamics 4 (2020) 249–263. doi:10.1007/s42064-020-0081-x.

[35] R. Wang, C. Wei, Y. Wu, Y. Zhao, The study of spin control of flexible electric sail using the absolute nodal coordinate formulation, in: 2017 IEEE International Conference on Cybernetics and Intelligent Systems (CIS) and IEEE Conference on Robotics, Automation and Mechatronics (RAM), 2017, pp. 785–790. doi:10.1109/ICCIS.2017.8274879.

[36] K. U. Kristiansen, P. L. Palmer, R. M. Roberts, Numerical modelling of elastic space tethers, Celestial Mechanics and Dynamical Astronomy 113 (2) (2012) 235–254. doi:10.1007/s10569-012-9411-5.

[37] B. He, K. Li, R. Nie, B. Gao, Deployment modeling for soft cable networks from slack to tension, International Journal of Mechanical Sciences 221 (5 2022). doi:10.1016/j.ijmecsci.2022.107225.

[38] E. Xing, C. Zhou, Analysis of the bending behavior of a cable structure under microgravity, International Journal of Mechanical Sciences 114 (2016) 132–140. doi:10.1016/j.ijmecsci.2016.05.013.

[39] B. Buckham, F. R. Driscoll, M. Nahon, Development of a Finite Element Cable Model for Use in Low-Tension Dynamics Simulation , Journal of Applied Mechanics 71 (4) (2004) 476–485. arXiv:https://asmedigitalcollection.asme.org/appliedmechanics/article-pdf/71/4/476/5471132/476_1.pdf, doi:10.1115/1.1755691.

[40] Z. Zhu, S. Meguid, Elastodynamic analysis of low tension cables using a new curved beam element, International Journal of Solids and Structures 43 (6) (2006) 1490–1504. doi:https://doi.org/10.1016/j.ijsolstr.2005.03.053.

[41] A. A. Shabana, Definition of the Slopes and the Finite Element Absolute Nodal Coordinate Formulation, Multibody System Dynamics 1 (1997) 339–348. doi:10.1023/A:1009740800463.

[42] A. A. Shabana, Computer Implementation of the Absolute Nodal Coordinate Formulation for Flexible Multibody Dynamics, Nonlinear Dynamics 16 (1998) 293–306. doi:10.1023/A:1008072517368.

[43] A. A. Shabana, R. Y. Yakoub, Three Dimensional Absolute Nodal Coordinate Formulation for Beam Elements: Theory , Journal of Mechanical Design 123 (4) (2000) 606–613. arXiv:https://asmedigitalcollection.asme.org/mechanicaldesign/article-pdf/123/4/606/5758672/606_1.pdf, doi:10.1115/1.1410100.

[44] M. Omar, A. Shabana, A TWO-DIMENSIONAL SHEAR DEFORMABLE BEAM FOR LARGE ROTATION AND DEFORMATION PROBLEMS, Journal of Sound and Vibration 243 (3) (2001) 565–576. doi:https://doi.org/10.1006/jsvi.2000.3416.

[45] M. Berzeri, A. Shabana, DEVELOPMENT OF SIMPLE MODELS FOR THE ELASTIC FORCES IN THE ABSOLUTE NODAL CO-ORDINATE FORMULATION, Journal of Sound and Vibration 235 (4) (2000) 539–565. doi:https://doi.org/10.1006/jsvi.1999.2935.

[46] J. Gerstmayr, A. A. Shabana, Analysis of thin beams and cables using the absolute nodal co-ordinate formulation, Nonlinear Dynamics 45 (2006) 109–130. doi:10.1007/s11071-006-1856-1.

[47] P. G. Gruber, K. Nachbagauer, Y. Vetyukov, J. Gerstmayr, A novel director-based Bernoulli–Euler beam finite element in absolute nodal coordinate formulation free of geometric singularities, Mechanical Sciences 4 (2) (2013) 279–289. doi:10.5194/ms-4-279-2013.

[48] F. Sheng, Z. Zhong, K. H. Wang, Theory and model implementation for analyzing line structures subject to dynamic motions of large deformation and elongation using the absolute nodal coordinate formulation (ANCF) approach, Nonlinear Dynamics 101 (2020) 333–359. doi:10.1007/s11071-020-05783-4.

[49] J. Gerstmayr, H. Sugiyama, A. Mikkola, Review on the absolute nodal coordinate formulation for large deformation analysis of multibody systems, Journal of Computational and Nonlinear Dynamics 8 (3) (2013). doi:10.1115/1.4023487.

[50] K. Otsuka, K. Makihara, H. Sugiyama, Recent Advances in the Absolute Nodal Coordinate Formulation: Literature Review From 2012 to 2020, Journal of Computational and Nonlinear Dynamics 17 (8) (2022). doi:10.1115/1.4054113.

[51] J. Liu, J. Hong, Nonlinear formulation for flexible multibody system with large deformation, Acta Mechanica Sinica/Lixue Xuebao 23 (2007) 111–119. doi:10.1007/s10409-006-0046-1.

[52] H. Sugiyama, J. L. Escalona, A. A. Shabana, Formulation of three-dimensional joint constraints using the absolute nodal coordinates, Nonlinear Dynamics 31 (2003) 167–195. doi:10.1023/A:1022082826627.

[53] D. García-Vallejo, J. L. Escalona, J. Mayo, J. Domínguez, Describing Rigid-Flexible Multibody Systems Using Absolute Coordinates (2003).

[54] D. García-Vallejo, J. Mayo, J. L. Escalona, J. Domínguez, Three-dimensional formulation of rigid-flexible multibody systems with flexible beam elements, Multibody System Dynamics 20 (2008) 1–28. doi:10.1007/s11044-008-9103-9.

[55] T. Z. Htun, H. Suzuki, D. García-Vallejo, On the theory and application of absolute coordinates-based multibody modelling of the rigid–flexible coupled dynamics of a deep-sea ROV-TMS (tether management system) integrated model, Ocean Engineering 258 (February) (2022) 111748. doi:10.1016/j.oceaneng.2022.111748.

[56] J. R. Yuan, H. Ding, Dynamic model of curved pipe conveying fluid based on the absolute nodal coordinate formulation, International Journal of Mechanical Sciences 232 (10 2022). doi:10.1016/j.ijmecsci.2022.107625.

[57] A. A. Shabana, Flexible Multibody Dynamics: Review of Past and Recent Developments, Multibody System Dynamics 1 (2) (1997) 189–222. doi:10.1023/A:1009773505418.

[58] P. Eberhard, W. Schiehlen, Computational dynamics of multibody systems: History, formalisms, and applications, Journal of Computational and Nonlinear Dynamics 1 (1) (2006) 3–12. doi:10.1115/1.1961875.

[59] J. L. Tang, G. X. Ren, W. D. Zhu, H. Ren, Dynamics of variable-length tethers with application to tethered satellite deployment, Communications in Nonlinear Science and Numerical Simulation 16 (8) (2011) 3411–3424. doi:10.1016/j.cnsns.2010.11.026.

[60] C. Q. Luo, J. L. Sun, H. Wen, D. P. Jin, Dynamics of a tethered satellite formation for space exploration modeled via ANCF, Acta Astronautica 177 (2020) 882–890. doi:10.1016/j.actaastro.2019.11.028.

[61] Z. Bai, X. Jiang, Effects of Orbital Perturbations on Deployment Dynamics of Tethered Satellite System Using Variable-Length Element, IEEE Access 9 (2021) 22399–22407. doi:10.1109/ACCESS.2021.3056458.

[62] J. Sun, E. Chen, T. Chen, D. Jin, Spin dynamics of a long tethered sub-satellite system in geostationary orbit, Acta Astronautica 195 (2022) 12–26. doi:10.1016/j.actaastro.2022.02.026.

[63] M. Shan, J. Guo, E. Gill, Deployment dynamics of tethered-net for space debris removal, Acta Astronautica 132 (2017) 293–302. doi:10.1016/j.actaastro.2017.01.001.

[64] M. Shan, J. Guo, E. Gill, An analysis of the flexibility modeling of a net for space debris removal, Advances in Space Research 65 (3) (2020) 1083–1094. doi:10.1016/j.asr.2019.10.041.

[65] D. Negrut, E. J. Haug, H. C. German, An implicit Runge-Kutta method for integration of differential algebraic equations of multibody dynamics, Multibody System Dynamics 9 (2003) 121–142. doi:10.1023/A:1022506312444.

[66] L. Zhang, D. Zhang, A two-loop procedure based on implicit Runge–Kutta method for index-3 DAE of constrained dynamic problems, Nonlinear Dynamics 85 (2016) 263–280. doi:10.1007/s11071-016-2682-8.

[67] J. Chung, G. M. Hulbert, A Time Integration Algorithm for Structural Dynamics With Improved Numerical Dissipation: The Generalized-α Method, Journal of Applied Mechanics 60 (2) (1993) 371–375. arXiv:https://asmedigitalcollection.asme.org/appliedmechanics/article-pdf/60/2/371/5463014/371_1.pdf, doi:10.1115/1.2900803.

[68] M. Arnold, O. Brüls, Convergence of the generalized-α scheme for constrained mechanical systems, Multibody System Dynamics, Springer Verlag 85 (2007) 187–202. doi:10.1007/s11044-007-9084-0.

[69] W. Hu, Y. Huai, M. Xu, Z. Deng, Coupling dynamic characteristics of simplified model for tethered satellite system, Acta Mechanica Sinica/Lixue Xuebao 37 (2021) 1245–1254. doi:10.1007/s10409-021-01108-9.

[70] W. Hu, M. Xu, F. Zhang, C. Xiao, Z. Deng, Dynamic analysis on flexible hub-beam with step-variable cross-section, Mechanical Systems and Signal Processing 180 (11 2022). doi:10.1016/j.ymssp.2022.109423.

[71] P. Janhunen, Increased electric sail thrust through removal of trapped shielding electrons by orbit chaotisation due to spacecraft body, Annales Geophysicae 27 (2009) 3089–3100. doi:10.5194/angeo-27-3089-2009.

[72] G. Li, Z. H. Zhu, C. Du, Stability and control of radial deployment of electric solar wind sail, Nonlinear Dynamics 103 (2021) 481–501. doi:10.1007/s11071-020-06067-7.

[73] J. A. Fulton, H. Schaub, Fixed-axis electric sail deployment dynamics analysis using hub-mounted momentum control, Acta Astronautica 144 (2018) 160–170. doi:10.1016/j.actaastro.2017.11.048.

[74] J. Valverde, D. García-Vallejo, Stability analysis of a substructured model of the rotating beam, Nonlinear Dynamics 55 (2009) 355–372. doi:10.1007/s11071-008-9369-8.

[75] D. García-Vallejo, J. Valverde, J. Domínguez, An internal damping model for the absolute nodal coordinate formulation, Nonlinear Dynamics 42 (2005) 347–369. doi:10.1007/s11071-005-6445-1.

[76] J. G. de Jalon, E. Bayo, Kinematic and dynamic simulation of multibody systems: The real-time challenge, SpringerLink (1993).

[77] M. Shuster, A Survey of Attitude Representations, Astronautical Sciences 41 (4) (1993) 439–517.

[78] A. D. Wright, C. E. Smith, R. W. Thresher, J. L. C. Wang, Vibration Modes of Centrifugally Stiffened Beams, Journal of Applied Mechanics 49 (1982) 197–202.

[79] J. K. Zbrozek, The simple harmonic motion of a helicopter rotor with hinged blades, Aeronautical Research Council R&M (2813) (1955).

[80] S. Mikhailov, E. Nikolaev, N. Shilova, Dynamics of Coupled Flap-Lag Motion by the Helicopter Rotor Blades, IFAC Proceedings Volumes 37 (6) (2004) 565–570. doi:https://doi.org/10.1016/S1474-6670(17)32235-8.

[81] D. García-Vallejo, J. Mayo, J. L. Escalona, J. Domínguez, Efficient evaluation of the elastic forces and the jacobian in the absolute nodal coordinate formulation, Nonlinear Dynamics 35 (2004) 313–329. doi:10.1023/B:NODY.0000027747.41604.20.